MICROFLUIDIC DEVICES FOR STIFFNESS DEPENDENT ENRICHMENT OF RED BLOOD CELL SUBPOPULATIONS

A Dissertation
Presented to
The Academic Faculty

By

Faisal Ahmed

In Partial Fulfillment
of the Requirements for the Degree
Doctor of Philosophy in the
School of BioEngineering

Georgia Institute of Technology

December 2017

MICROFLUIDIC DEVICES FOR STIFFNESS DEPENDENT ENRICHMENT OF RED BLOOD CELL SUBPOPULATIONS

Approved by:

Dr. Cyrus K Aidun, Advisor
School of Mechanical Engineering
Georgia Institute of Technology

Dr. Gilda A Barabino, Advisor
School of Biomedical Engineering
The City College of New York

Dr. Edward Botchwey
School of Biomedical Engineering
Georgia Institute of Technology

Dr. J Brandon Dixon
School of Mechanical Engineering
Georgia Institute of Technology

Dr. Wilbur A Lam
School of Biomedical Engineering
Georgia Institute of Technology

Date Approved: August 29, 2017

Be thankful for what you have, work hard for what you want to achieve, be kind and respectful to others.

Self

Dedicated to my family.

ACKNOWLEDGEMENTS

I would like to express my deepest gratitude to my advisors, Dr. Cyrus K. Aidun and Dr. Gilda A. Barabino. I was very fortunate to be co-advised by them and to have the opportunity to learn a great deal about scientific research from them. I will always be grateful to them for their wisdom, guidance, enormous support and the freedom they provided me to explore on my own.

My deepest gratitude goes to all my committee members. Their support for my PhD research went above and beyond the norm. I thank them from the bottom of my heart for providing me lab space, samples and invaluable suggestions throughout this whole time.

I am grateful to all my lab mates, especially Dr. Yueh Hsung Yang, Dr. Shereka Banton and Mykel Green for their support, valuable suggestions and reviews. Special thanks goes to Dr. David Myers, Yumiko Sakurai and others at Dr. Wilbur Lam's lab for their suggestion on experiments and for always being there to provide me samples when I needed. I am deeply gratified to Dr. Dixon and all his lab members for letting me use their lab space and equipments. My gratitude also goes to core lab and administrative staffs at IBB, administrative staffs at Department of Biomedical Engineering and RBI for their support with logistics and administrative issues.

I am grateful to all my friends at Georgia Tech and the ones in Bangladeshi community who have supported me in many ways throughout this challenging journey.

I will never be able to show enough gratitude to my family members, especially my parents, my brother, my in-laws and my beloved wife, who were always there for me to take the lion share of my agony and pain at difficult times during this whole journey. I am deeply gratified and thankful to my wife Safina, who has been there for me all the time and has been my greatest source of support.

Last but not the least, I am thankful to the almighty for the blessings and always taking care of me and my family.

TABLE OF CONTENTS

LIST OF TABLES

LIST OF FIGURES

SUMMARY

Red blood cell is the most dominant cell type of blood and these cells are often the target of many hematologic diseases such as sickle cell disease, malaria, spherocytosis and some types of cancers. In addition to affecting biological properties, these diseases also alter biomechanical properties such as morphology, size and stiffness of red blood cells. Separating or enriching the cellular components of blood into subpopulations based on their biomechanical properties and analyzing them have the potential to lead to enhanced strategies for assessment of disease progression and treatment of these diseases. Current techniques and equipment for diseased cell sample enrichment are time consuming, expensive and need well trained professionals to be conducted. Microfluidic platform based red blood cell enrichment device is one of the most promising technologies that are currently the subject of considerable interest among researchers because of its low cost, high throughput, easy operation and the potential to do enrichment within the physiological flow condition. In this research work, microfluidic devices were designed, fabricated and tested for enriching red blood cell subpopulations based on their stiffness from a mixture of stiff and normal red blood cells. In the first portion of the work, lab developed numerical simulation tools were deployed to study stiffness dependent margination pattern of red blood cells in high aspect ratio straight microchannels with rectangular cross-section. Stiff red blood cells were observed to marginate near the channel walls whereas normal (and hence more deformable) red blood cells were observed to marginate to the central core of the channel regardless whether cell-cell interactions were present or not. Cells of different stiffness reached to their equilibrium locations faster in channels with smaller cross sections. Increasing flow Reynolds number and hence the flow rate resulted in stronger segregation between normal and stiff red blood cells for the whole range of Reynolds numbers for which simulations were run. Increasing cell volume fraction in solution also boosted separation between cells of different stiffness. Based on the findings of the simulations, two types of

cell enrichment devices were designed and fabricated, simple straight channel device and multistep device. The simple straight channel device was tested for a wide range of flow Reynolds number and cell volume fractions. Simple straight channels were observed to perform better with increasing flow Reynolds number and cell volume fraction up to certain threshold for each of them, and after that threshold no significant improvement of performance was observed. Numerical simulations were conducted with parameters matching with some of the experiments and the results obtained were remarkably close to those from the experiments. Statistical analysis on experimental data found the effect of individual parameters, flow Reynolds number and cell volume fraction, to be significant. It also revealed that there was significant interaction between the factors flow Reynolds number and volume fraction. This implies that the extent of the effect of one factor (e.g. flow Reynolds number) changes when the value of the other factor (e.g. volume fraction) varies and for best performance of the devices the combination of flow Reynolds number and volume fraction needs to be optimized. The multistep device was also tested for different combinations of flow Reynolds number and cell volume fraction and, was observed to perform 1.6 times to 3.15 times better than single step device in enriching stiff cells from a mixture of stiff and normally deformable red blood cells. To our knowledge this is the first study that incorporated such rigorous multiphysics simulations to support experimental study on stiffness dependent margination of red blood cells in straight micro-channels. This research work improved the performance and throughput of simple straight channel enrichment device, revealed previously unreported information about stiffness dependent cell enrichment with simple straight channel microfluidic device and proposed a new device that performed significantly better than the simple straight channel device.

CHAPTER 1
INTRODUCTION AND BACKGROUND

Blood, which has its origin at the bone marrow and is spread throughout the whole body, is arguably the most important biological fluid in human body [1]. Two main constituents of blood are plasma (approximately 60% volume fraction) and cells (approximately 40% volume fraction). Out of nearly five billion cells per milliliter of blood, red blood cells (RBCs) make up more than 99% of all cellular components and the rest are composed of different types, of which leukocytes/white blood cells (WBCs), platelets and monocytes are significant. For quite a number of hematologic diseases such as, sickle cell disease (SCD), malaria, spherocytosis and some types of cancer, RBC is the primarily affected cell type. In addition to changing biological properties, all of these diseases alter the bio-mechanical properties e.g. stiffness, morphology and size of RBCs. Separating the cellular components of blood into subpopulation based on their bio-mechanical properties and analyzing them are likely to lead to enhanced strategies for assessment of disease progression and treatment of these diseases. Current technologies for diseased cell sample enrichment include density gradient/ centrifugation method, flow cytometer, dieelectrophoresis activated cell sorting (DACS) and acoustic sorting. All of these are time consuming, expensive and need well trained professionals to be conducted. Also, the most common of the above mentioned methods, the density gradient method, puts the cells under non-physiological stress. This causes expression of additional proteins of RBCs, thereby making any further study on them biased and erroneous [2]. Microfluidic platform based RBC enrichment device is one of the most promising technologies that are currently the subject of considerable interest among researchers because of its low cost, high throughput, easy operation and the potential to do enrichment within the physiological flow condition.

The main motivation for this research work is to enrich SCD affected RBC from patients

blood sample. SCD is a highly complex and inherited blood disorder affecting people from African descent, South or Central America, Caribbean Islands, Mediterranean countries (Turkey, Greece and Italy) and India. According to a 2016 report of Red Cross [3], one in approximately 1500-2000 newborn in the US is diagnosed with SCD and currently there are around 100000 SCD patients only in the US. Globally about 400000 new babies are born with SCD per year [4]. With per person inpatient care cost of about $ 16000 per year, annual health care cost of SCD only in the US about 1.6 billion. Regular episodes of intense bone pain is the most common manifestation of SCD. Sickle cell patients very often are affected by other diseases like bone growth disorder, bone necrosis, heart disease, stroke, etc. Life expectancies of SCD patients is $<$50 years in the US [5] with about 11% suffering clinically apparent stroke before the age of 20 years[6]. In Africa mortality among SCD affected children ($<$5 years old) 50% -90% [7].

In the next subsections the genetic basis of SCD and change of RBC stiffness and morphology in SCD will be discussed.

1.1 Genetic Basis of Sickle Cell Disease

The genetic basis for SCD is a DNA point mutation at the sixth codon of gene (thymine for adenine, GAG $\rightarrow$ GTG) [2, 8] responsible for β -hemoglobin (β -Hb) production in red blood cells (RBC). This mutation causes the substitution of polar hydrophilic glutamic acid with non-polar hydrophobic valine at the sixth position of each β -globin chain in hemoglobin, converting β -Hb to β S-Hb or HbS. Under the deoxygenated conditions occurring in microcirculation, HbS molecules polymerize to form rigid fibers distorting the RBC cytoskeleton. This eventually changes the shape of RBCs from discoid to sickle and makes the RBCs stiffer. Under oxygenated conditions the fibers melt away and RBCs return to their normal shape. Figure 1.1 shows the genetic basis of SCD and morphology change of SCD affected RBC. Details about the genetic basis of SCD and the associated complications can be found in many literatures [2, 8–12].

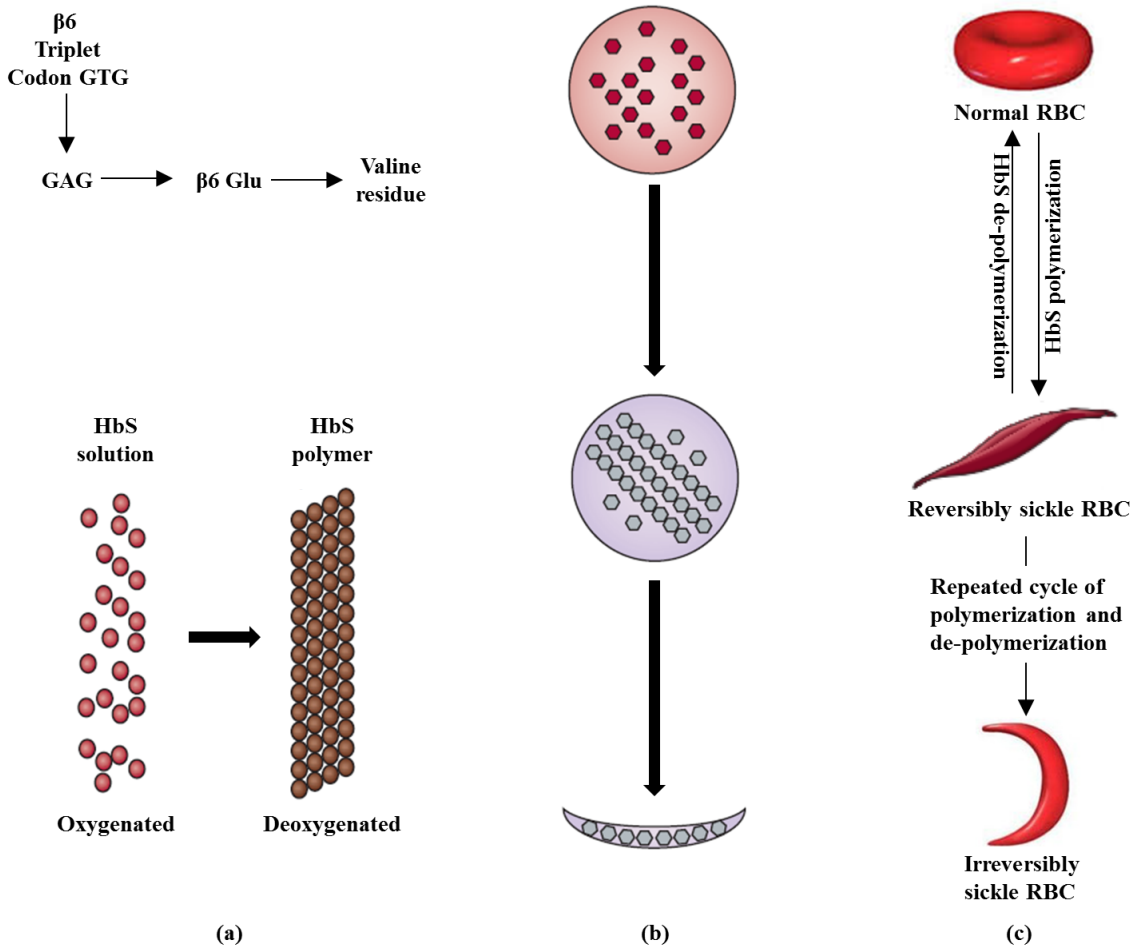

Figure 1.1: Genetic basis of SCD. (a) DNA point mutation at the sixth codon of gene and HbS polymerization under deoxygenation (figure adapted from [8]). (b) HbS polymerization inside RBC and RBC shape distortion (figure adapted from [13]). (c) Conversion of normal RBC to ISC.

1.2 Red Blood Cell Stiffness Change in Sickle Cell Disease

As RBC is the major cell type in blood, its deformability is the primary determinant of blood behavior in microcirculation, because RBCs must deform for them to pass through narrow capillaries that have diameters half the size of their own [10]. Two classes of factors contribute to deformability of RBCs, intrinsic and extrinsic [2]. The intrinsic factors, factors inherent to the membrane and internal contents, include elasticity, viscosity and fragility of membrane, cytoplasmic viscosity, increased permeability to cations, RBC dehydration and stiffened cytoskeleton [2, 11, 12, 14]. The extrinsic factors include oxygen

tension, osmolality, pH, temperature and concentration of plasma protein which are related to surface area, volume and environment [2].

There are mainly two mechanisms by which SCD affected RBCs become stiffer than the normal ones. One of them is the HbS polymerization inside RBC. As shown in figure 1.1, under deoxygenated condition the mutated HbSs in RBC start polymerizing. These single polymer fibers aggregate in groups and push the RBC membrane decreasing its deformability.The decrease in deformability occurs even before the morphological sickling takes place [2]. The second mechanism of RBC deformability reduction is through dehydration from RBC [11, 15–22]. Brugnara *et al.* [20, 21] and Mohandas *et al.* [22] shed light on the intricate relationship between sickling and dehydration by showing that deoxygenation and sickling increases permeability of cell membrane to cations (K^+, Na^+ and Ca^{2+}) resulting in water efflux. As RBC dehydrates, the mean cellular hemoglobin concentration (MCHC) increases, which results in increase of cytosolic viscosity leading to decrease in RBC deformability. Alternatively, due to higher membrane permeability, sickle RBCs may sometimes be over hydrated [2]. This will cause RBC volume to increase, resulting in decrease in surface area to volume ratio and hence its deformability. Nash *et al.* [23] and Evans *et al.* [11] showed, even under normally oxygenated condition, sickle RBCs demonstrated a higher stiffness compared to the healthy ones.

1.3 Red Blood Cell Shape Change in Sickle Cell Disease

As mentioned in section 1.1, under deoxygenated condition occurring in micro-circulation of the body, SCD affected RBCs undergo shape change due to polymerization of HbS and return to their usual discoidal shape under oxygenated condition. However, after repeated cycles of sickling and unsickling, the RBCs get permanently sickle, and these subpopulations of RBCs are known as Irreversibly Sickle Cells (ISCs) [2, 8, 24]. An overview of the process can be seen in 1.1.

1.4 Subpopulation of Red Blood Cells in Sickle Cell Disease

As mentioned in previous sub-sections, in SCD, RBCs lose their deformability and undergo morphological changes due to repeated HbS polymerization and de-polymerization cycles under deoxygenated (venous circulation) and reoxygenated (arterial circulation) condition. So at any particular time, no matter if the condition is oxygenated or deoxygenated, a sickle patients blood sample contains RBCs of variable morphology and deformability along with healthy RBCs. Using density gradient method to fractionate and Scanning Electron Microscopy (SEM) to study the morphology, Kaul *et al.* [24] identified four different fractions of RBCs (based on their hemoglobin concentration or deformability and shape) from blood samples of each patients they studied. These fractions can be listed as:

1. Fraction I: having large percentage of reticulocytes and a small percentage of ISCs, many of the reticulocytes appear lobulated, while the others appear as flat or ovalocytic under oxygenated condition.

2. Fraction II: having large percentage of cells of discocytes morphology at oxygenated state or RSCs and small portion of reticulocytes and ISCs.

3. Fraction III: mainly dense discocytes at oxygenated states with some ISCs.

4. Fraction IV: mainly ISCs.

Figure 1.2 shows the SEM images to reveal morphology of the subpopulations both under oxygenated and deoxygenated conditions. Fraction I, rich in multi-lobulated reticulocytes, assume multi-spiculated form upon deoxygenation. RBCs of fraction II mostly take the typical sickle shape under deoxygenated condition. Minimal transformation is seen in fraction III, displaying only tiny spicules projected from a more or less circular morphology, while faction IV being rich in ISCs shows no significant morphological change.

It is clear from above discussion that, in case of SCD, RBCs hold important information related to disease pathology. However, analysis of disease mechanism has been

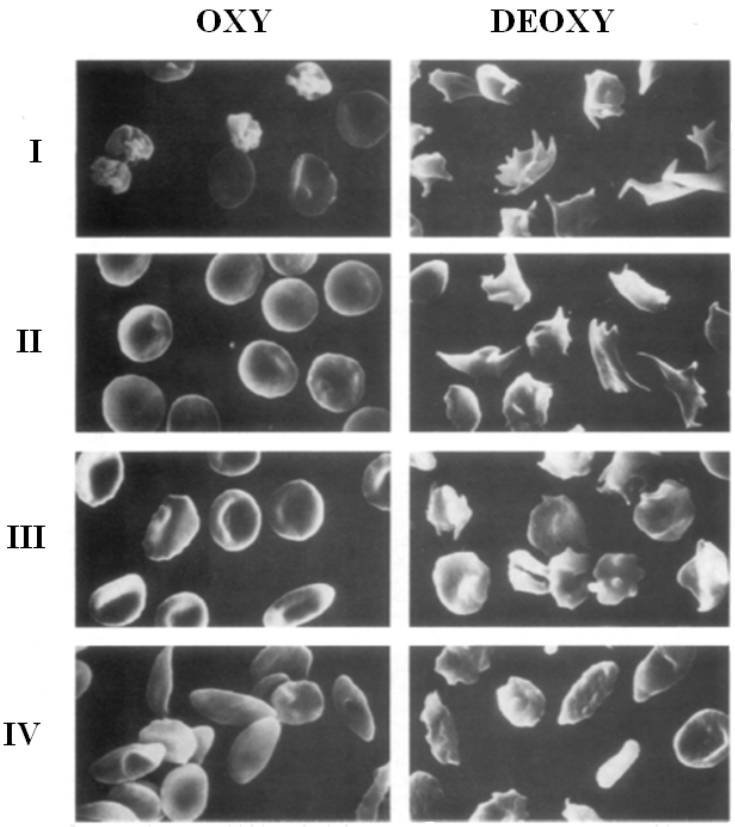

Figure 1.2: Subpopulation of SCD affected RBCs (figure adapted from Kaul *et al.*[24])

complicated greatly by the heterogeneity of the RBCs themselves, as subpopulations of different characteristics coexist in sickle blood [24, 25]. To analyze different aspects of SCD in general and its severity and progression for an individual patient, it is imperative to be able to isolate different subpopulations of sickle RBCs from patient whole blood samples in a reasonably short time and at low expense. The main objetive of this research is to design and fabricate a microfuidic device that will isolate / enrich RBC subpopulations based on their stiffness, while there is no morphological difference between the subgroups. This research will eventually lead to the development of a separation device, that will be able to isolate SCD affected stiff RBCs with similar shape as normal ones from patient's blood sample. The objectives and steps followed for this research are summarized in the following list:

- At first stiffness dependent margination of RBCs in a rectangular cross secion chan-

nel will be explored by performing direct numerical simulation (DNS) with the help of a lattice Boltzmann method based simulation tool. In chapter 2 effects of RBC's internal viscosity, channel dimension, shear rate and RBC volume fraction on margination of RBCs in transverse direction to flow had been studied for flow in a straight channel with rectangular cross section.

- Microfluidic channels with different features will be designed and fabricated based on the insights obtained from the simulations. Experiments will be conducted to enrich RBC samples based on their stiffness. Sample enrichment performance of the devices will be characterized for variation in parameters like flow rate and cell volume fraction. Experimental results are presented in chapter 3.

CHAPTER 2
INTERNAL VISCOSITY DEPENDENT LATERAL MARGINATION OF RED BLOOD CELLS IN STRAIGHT RECTANGULAR CROSS-SECTION MICRO-FLUIDIC CHANNEL

2.1 Introduction

Lateral margination mechanism of solid particles [26–31], deformable droplets [29, 32–38], elastic particles [39], capsules [40, 41] and lipid vesicles [42] have been studied extensively by several authors. In their study on rigid particles and deformable droplets, Goldsmith *et al.* [29] found out that, at low channel Reynolds number(Re_c) range, when inertial effect is negligible, only the deformable droplets migrate in cross flow direction and no such phenomenon was observed for rigid particles. This was later supported by the study of Asmolov *et al.* [31] and Schonberg *et al.* [28]. They derived an expression for net force that caused the transverse migration and showed that the value of the force is linearly dependent on particle deformation, thereby explaining why the deformable particles show lateral migration and the solid ones do not. One of the earliest studies was done during 1960s by Segré & Silberberg [43, 44], who studied lateral migration of rigid particles under flow condition where the effect of inertia is not negligible. They discovered that rigid particles in inertial tube flow marginate to equilibrium positions at a radial distance of approximately 0.6 tube radii from the axis and this phenomenon is irrespective of the radial position at which the particles enter the tube. A particle in a Poiseuille flow, as shown in figure 2.1(a), experiences two opposing forces. One is F_S (figure 2.1(b)), a force acting away from the centerline and towards the wall, created due to non-linear velocity (hence, shear gradient) and negative slip velocity (as particle velocity at its centroid always lags behind the undisturbed flow velocity) [32, 39, 45, 46]. The other force experienced by the

particle is F_W (shown in figure 2.1), which acts in the opposing direction to F_S. This is due to the presence of enclosure or wall, and hence also known as wall force, whose mechanism is well described [31–33, 42, 47–50]. This equilibrium lateral position, as observed by Segré & Silberberg, is a result of the balance between the two opposing forces F_S and F_W.

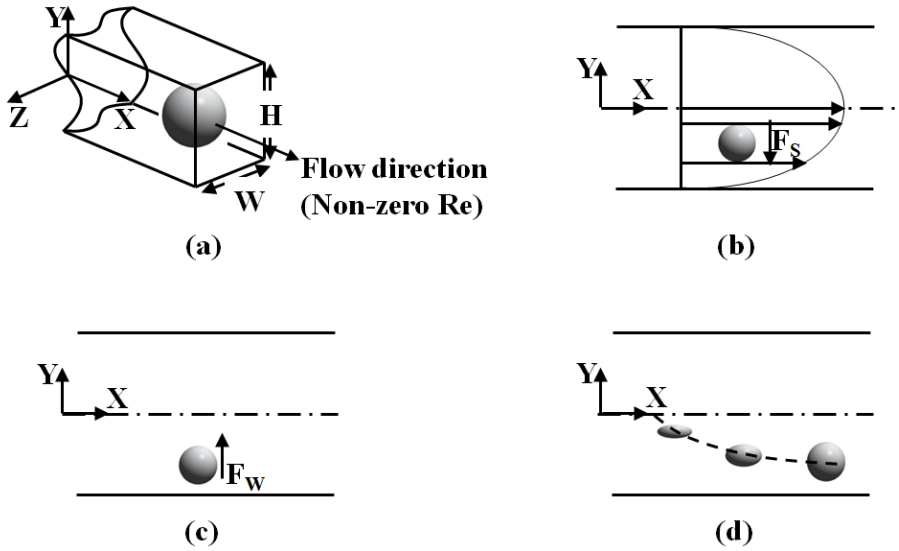

Figure 2.1: Particle migration mechanism in plain Poiseuille flow. (a) A single particle in Poiseuille flow, (b) Non-linear shear force, (c) Wall force, (d) Migration of deformable particle.

Non-inertial lateral migration of deformable particles has been studied by numerous authors in the past couple of years [32, 35–38, 40, 51, 52]. The migration pattern of deformable particles is similar to as observed for solid particles under the effect of inertia, they migrate to equilibrium positions located somewhere between the centerline and wall. Mortazavi *et al.* [32] conducted numerical simulations with single droplet in a channel and found that in the range of small to moderate channel Reynolds number ($Re_c \leq 1$), drop migration strongly depends on the ratio of internal viscosity of the drop to the viscosity of the suspending fluid (λ). For $\lambda = 0.125$ drop moves towards the center of the channel, whereas for $\lambda \geq 0.125$ it moves away from the centerline and somewhat stabilizes at an equilibrium location between the wall and the centerline. These findings are quite in

agreement with the findings of experimental study of Hiller *et al.* [37] and, numerical studies of Zhou *et al.* [38] and Doddi *et al.* [40]. Mortazavi *et al.* [32] explained the migration mechanism using slip velocity and non-uniform velocity in Poiseuille flow. Slip velocity is defined as the axial velocity of the particle minus the undisturbed fluid velocity at the position of particle centroid. As the particle velocity always lags behind the undisturbed flow for creeping flow [32, 35], the slip velocity is a negative quantity. Due to negative slip velocity and non-uniform shear, a particle experiences a force towards the wall. As a particle with higher deformability will be thinner than the one with lower deformability, the more deformable one will have less velocity gradient around it and hence the particle with higher deformability will experience lesser force due to non-linear shear and stay closer to the centerline. It was also shown in [32, 33, 35, 40, 46] that the drift or migration velocity of particles towards the equilibrium position is higher for more deformable particles compared to the lesser ones.

For flow with higher Reynolds number, effect of inertia starts playing a significant role and there is a competition between the inertial effect and the deformability effect (also represents shear effect) [32]. The final transverse equilibrium position of a deformable particle in an inertial flow will be determined by the dominant factor of this competition. For flows with dominant inertial effect the equilibrium position is determined by Segré-Silberberg effect [43]. Mortazavi *et al.* [32] using front-tracking algorithm, Lan *et. al.* [34] using volume of fluid (VOF) approach and Hur *et. al.* [46] using experiments have shown that when the effect of inertia becomes dominant, the deformable particles settle down at equilibrium positions somewhere between the centerline and the wall after an initial period of transient or oscillatory movement. Studies done by Kilimnik *et al.* [53], Nourbakhsh *et al.* [54] and Krüger *et al.* [41] have shown that, the more deformable droplets take position near to the centerline while the less deformable ones stay closer to the wall as shown qualitatively in Figure 2.1 (d). The role of interplay of both deformability and inertia on deformable particle margination has only recently been explored. Di Carlo [55] first ex-

amined the effect of inertial force on particle margination and later in association with Hur *et al.* [46] experimentally showed deformability based particle enrichment under the effect of inertial force. More recently, Krüger *et al.* [41] studied the combined effect of inertia and deformability on margination of deformable capsules in semi-dilute (volume fraction $\phi = 10\%$) suspension by simulation combining finite element, immersed boundary and lattice-Boltzmann methods for Re_c ranging between 3 to 417. They found that deformable particles tend to concentrate more around the center line of channel with increasing Re_c whereas the less deformable ones get dispersed in span wise direction with higher Re_c.

With the exception of the one done by Hur *et al.* [46], all the experimental and theoretical studies mentioned so far were done with dilute suspensions and hence without considering the effect of inter particle interaction. Also all of them were conducted with synthetic deformable particles, capsules or spherical droplets working as models for cells. RBCs, the cell type of interest of this study, are of discoidal shape, have more membrane than required to enclose the volume and appear in concentrated regime. Because of these special geometrical and rheological properties, flow behavior of RBCs is quite complex and require in-depth analysis. Goldsmith *et al.* [56] conducted one of the first experiments to study the flow properties of individual RBC in the Re_c range of 10^{-5} to 0.1. Rigid body rotation of normal RBCs at very low shear stress $\left(\ll 0.1\frac{N}{m^2}\right)$, tank-treading motion and travelling of normal RBCs at a constant orientation to the flow at shear stress above $0.4\frac{N}{m^2}$, rigid body rotation of artificially stiffened RBCs, margination of normal (more deformable) RBCs around location near centerline compared to the stiffened ones and faster migration speed of deformable RBCs compared to stiffened ones in media of higher viscosity were their significant observations. In a follow up work [57], studying flow of dense suspension of ghost (artificial) RBCs in a circular channel in the Re_c range between 10^{-3} and 0.3. Goldsmith *et al.* found out that, at steady state a blunt velocity profile arises with a region of plug at the core of tube whose spread increases with increasing cell concentration and decreases with increasing flow rate and channel radius. They also observed that nor-

mal RBC ghosts went through remarkable deformation and tank treading motion at higher cell concentration whereas the stiffened ghost RBCs showed no deformation and continued to rotate at varying angular velocities. Dupin *et al.* [58] did a lattice-Boltzmann method (LBM) based simulation for dense suspension (30%) of deformable RBCs at physiological Reynolds number range $\mathcal{O}(10^{-2} - 10^{-3})$ and observed deformed tumbling at moderate shear rate of $10sec^{-1}$ (particle Reynolds, $Re_{RBC} = 0.016$) undeformed tumbling at shear rate lower than $10sec^{-1}$ and tank treading at higher shear, confirming the observations of Goldsmith *et al.* [56, 57]. They also found significant variation of pressure along the channel wall with time. One limitation to their study was that, they did not include the lubrication forces in their model that is supposed to give a more accurate representation of inter-cellular interaction. McWhirter *et al.* [59], through their 3-D simulations, studied the shape and clustering phenomena of individual RBCs in thin and dense suspension of RBCs in narrow capillary. At very low hematocrit they observed flow-induced cluster formation above a threshold flow velocity. However at higher hematocrit they observed three distinct phases. One phase consisted of disordered biconcave-disk-shape RBCs. The second phase was with parachute-shaped RBCs aligned in a single file. The third phase had, slipper-shaped RBCs arranged as two parallel interdigitated rows. For their study, they modeled RBCs to have same internal viscosity as the media they were suspended in, i.e. $\lambda = 1$. Using LBM-FEA method MacMeccan *et al.* [60] accurately predicted suspension viscosity and the shear thinning behavior of blood with 40% volume fraction of RBCs for shear rate ranging from $15sec^{-1}$ to $64sec^{-1}$ and $Re_{RBC} = 0.1$. Wu *et al.* [61] have shown the usefulness of using external boundary force (EBF) to impose no-slip boundary condition in LBM in conjunction with lattice-spring model (LSM) by simulating RBCs at physiological volume fraction of 47% in the shear rate range of $16sec^{-1}$ to $144sec^{-1}$ and accurately predicting the parachute-like shape of RBCs in capillary flow condition and the shear-thinning phenomenon. Reasor *et al.* [62, 63] from the same research group used LBM and spectrin-link (SL) method to do direct numerical simulation of cellular blood

flow, and demonstrated the efficacy of this method in reproducing the previous findings of Wu *et al.* [61] and provided new detailed analysis of rheology of blood flow including the development of normal stresses in shear flow. More recently Mehrabadi *et al.* [64] studied the effect of channel size, shear rate and particle properties on the lateral margination of platelets in a moderately dense suspension ($\phi = 20\%$) of RBCs and platelets. In this study, platelet margination was shown to be mainly driven by RBC-enhanced diffusion of platelets and entrapment in RBC-free layer near the wall. A scaling relation was developed showing margination length (L_D) to vary cubically with channel height and being independent of shear rate up to $20000sec^{-1}$ and $Re_{RBC} = 0.09$. They also found stiffness to have a stronger impact on margination than the size of the particle. However, to study the effect of stiffness on margination, Mehrabadi *et al.* [64] compared the margination behavior of normal deformable RBCs with that of platelets that were modeled as rigid oblate spheroids. All these studies [60–64] used plasma viscosity to be $\mu = 1.2 \times 10^{-3} {}^{N.sec}/_{m^2}$ and $\lambda = 5$, which are physiological values.

The current study focuses on studying the margination behavior of deformable RBCs based on their cytoplasmic viscosity, which is a major factor for defining RBC deformability. Results are reported for two broad classes of simulations, (1) studies on individual RBCs of different internal viscosities where there is no inter-cellular interaction, and (2) studies on semi-dense ($\phi = 10\%$) to dense ($\phi = 30\%$) suspensions of RBCs where inter-cellular interaction is significant. The second category, which is the major focus of our study, studies the impact of parameters like channel cross section size, shear rate ($\dot{\gamma}$) and volume fraction (ϕ) on the margination behavior of RBCs having different cytoplasmic viscosity. Preliminary experiments were conducted to validate the results obtained from simulation. To our knowledge, this is the first time a combined theoretical and experimental study probing lateral margination behavior of RBCs based on the RBC cytoplasmic viscosity for such a wide range of suspension density has been conducted. The findings of this study will contribute immensely not only to the understanding of the physics, but

also to the design of microfluidic devices for blood cell sample enrichment for different diseases.

2.2 Methodology

Direct Numerical Simulation (DNS) simulation of RBCs of different cytoplasmic viscosity is done with a coupled lattice-Boltzmann and spectrin-link (LB-SL) method [62, 63, 65]. In the LB-SL method, a lattice-Boltzmann (LB) solver for the fluid phase (i.e., RBC surrounding fluid and RBC cytoplasm) is coupled to a coarse-grained spectrin-link (SL) model for the RBC membranes. LB-SL method was developed by Reasor *et al.* [62, 63] based on the initial hybrid lattice-Boltzmann and finite element (FE) implementation of MacMeccan *et al.* [60]. SL method for modeling RBC membrane dynamics enables simulation of larger deformation of RBCs membrane at higher capillary number (Ca_G) number and captures full range of dynamics at no additional computational cost compared to the linear FE model of [60]. Message Passing Interface (MPI) protocol is used to run the LB-SL solver on multiple processors on super computers to simulate complex fluids with particles. LB-SL method has been validated to produce results that are in good agreement with past experimental and numerical studies such as deformation of isolated RBC stretched by optical tweezers and high shear, parachuting of RBCs in Hagen-Poiseuille flow and, experimental study of RBC rheological properties by viscometers [62, 63]. In the following subsection a brief outline of LB and SL method formulations used for this work is given. A more extensive derivation and validations are provided elsewhere in literatures [62, 63, 65–72].

2.2.1 Lattice Boltzmann Method

The lattice-Boltzmann method is a mesoscopic approach based on the discretization of the continuous Boltzmann equation in velocity space. It was developed as an alternative to lattice gas methods. The solution to the LB equations converge to the solution of the

incompressible Navier-Stokes equation at low wave numbers through Chapman-Enskog expansion [66] using advective scaling. This scaling is valid for low Mach (Ma) and low Reynolds number (Re) fluid flow cases and physiological blood flow problems fall well within that range of Ma and Re. Higher Re flows can be investigated using the entropic [73] and multi-relaxation time LB methods [74]. A comprehensive review of these methods can be found in review by Aidun *et al.* [67]. LBM is an attractive approach for simulating multiphase particulate flows, mainly because of two following advantages: (i) the computational expense of this method scales linearly with the number of particles since particle interactions are propagated on time scales that is smaller than that of particle motions [75, 76] and, (ii) time evolution of the fluid particle distribution at each node requires only the knowledge of particle distribution functions at neighboring nodes, making all calculations localized in space and therefore making LBM optimal for parallel computing [77]. Particulate flows with significant inertial flows can be handled with LBM because of its capability to resolve inertia through the Navier-Stokes equations [78]. Some of the first simulations of rigid suspensions using the LBM coupled with the standard bounce-back boundary condition were performed by Ladd *et al.* [75, 76, 79] and Aidun *et al.* [80, 81]. Ding *et al.* [82] developed methods for studying suspension of thin shells, which took into account the influence of forces caused by the fluid inside the particle. Development of these two, paved the way for development of method for simulating deformable particles combining LBM for fluid phase and finite element method (FEM) for the particles [60, 83].

In LBM, Boltzmann equation is discretized in velocity space in terms of a chosen set of velocity vectors $\vec{e_i}$, where $i = 1 \cdots Q$ represents velocity vector directions. This chosen velocity vector set results in a discrete lattice space denoted by $\vec{x}$. Particle distribution function f_i existing at each node can be thought of as the density of mesoscopic particles restricted to flow with velocities of $\vec{e_i}$. At each time step, the evolution of f_i is governed by the streaming and collision operators. Using the single-relaxation-time collision operator of Bhatnagar-Gross-Krook [84], the time evolution of f_i can be written as

$$f_i(\vec{x} + (\Delta x)\vec{e_i}, t + \Delta t) = f_i(\vec{x}, t) - \frac{1}{\tau}[f_i(\vec{x}, t) - f_i^{eq}(\vec{x}, t)] \tag{2.1}$$

where τ is the Bhatnagar-Gross-Krook relaxation time parameter determining the rate of relaxation to a local equilibrium distribution function $f_i^{eq}(\vec{x}, t)$, Δx is the lattice length (equivalent to grid size) in lattice unit and Δt is the time step size in lattice unit. The macroscopic flow kinematic viscosity ν is related to the relaxation time by $\nu = c_s^2 \left(\tau - \frac{1}{2}\right) \Delta t$, where c_s is the LB pseudo sound speed with value $c_s = \frac{\Delta x}{\sqrt{3}\Delta t}$. For LBM formulation both Δx and Δt are set to unity. Hence the relation between ν and τ becomes $\nu = c_s^2 \left(\tau - \frac{1}{2}\right)$ and the LB pseudo sound speed becomes $c_s = \sqrt{\frac{1}{3}}$. At low Mach numbers, i.e., at small $\frac{u}{c_s}$, the local equilibrium distribution can be approximated in terms of local macroscopic variables as

$$f_i^{eq}(\vec{x}, t) = \omega_i \rho \left[1 + \frac{1}{c_s^2}(\vec{e_i} \cdot \vec{u}) + \frac{1}{2c_s^4}(\vec{e_i} \cdot \vec{u})^2 - \frac{1}{2c_s^2}(\vec{u}.\vec{u})\right] \tag{2.2}$$

where, ρ is macroscopic density, $\vec{u}$ macroscopic velocity and ω_i are lattice constants dependent of LB stencil used for solving the fluid phase. For this work a D3Q19 stencil with single-relaxation-time LBM implementation of [60, 61] has been used for solving the fluid phase, where D represents the space dimension and Q represents the velocity vector directions. For D3Q19 stencil the lattices constants are

$$\omega_i = \begin{cases} \frac{1}{3} & \text{for } i = 0 \\ \frac{1}{18} & \text{for } i = 1 \cdots 6 \\ \frac{1}{36} & \text{for } i = 7 \cdots 18 \end{cases} \tag{2.3}$$

where $i = 0$ is for the rest, $i = 1 \cdots 6$ are for non-diagonal and $i = 7 \cdots 18$ are for diagonal directions of the lattice. Figure 2.2 shows the D3Q19 stencil.

By definition the macroscopic fluid properties are found by the moments of $f_i^{eq}(\vec{x}, t)$.

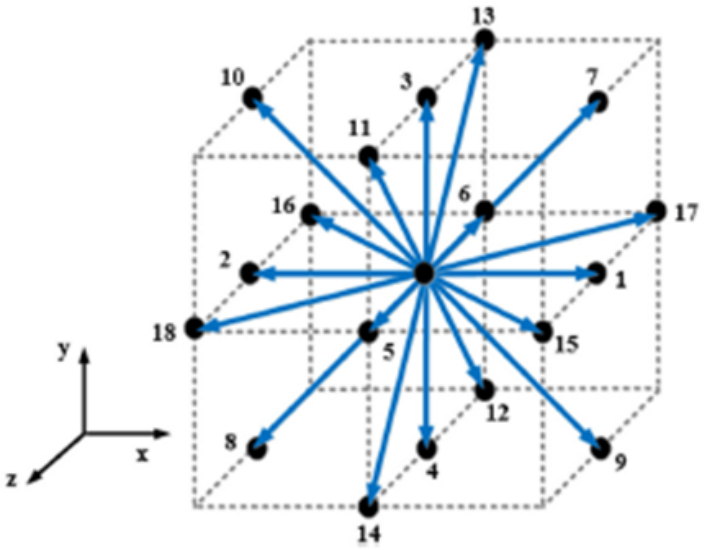

Figure 2.2: D3Q19 stencil (figure adapted from Hashemi *et al.*[85])

Density (ρ) is given by the first moment as

$$\rho(\vec{x},t) = \sum_{i}^{Q} f_i^{eq}(\vec{x},t) \tag{2.4}$$

and the solid phase density, $\rho_s(\vec{x},t)$ is to chosen to be same as $\rho(\vec{x},t)$. The velocity is given by the second moment of $f_i^{eq}(\vec{x},t)$ as

$$\rho(\vec{x},t)\vec{u}(\vec{x},t) = \sum_{i}^{Q} f_i^{eq}(\vec{x},t)\vec{e_i} \tag{2.5}$$

The third moment of $f_i^{eq}(\vec{x},t)$ gives the expression for pressure as following

$$c_s^2\rho(\vec{x},t)\mathbb{I} + \rho\vec{u}(\vec{x},t)\vec{u}(\vec{x},t) = \sum_{i}^{Q} f_i^{eq}(\vec{x},t)\vec{e_i}\vec{e_i} \tag{2.6}$$

where $\mathbb{I}$ is the identity matrix. In LBM formulation, pressure is proportional to the density, i.e. $P = c_s^2\rho = \frac{1}{3}\rho$, which is why LBM is pseudo-compressible and requires flows of analysis to be of low Mach number.

2.2.2 Spectrin-link Method

The SL model for deformable RBC membrane is based on the idea of mimicking the physiological construction of RBC membrane that is mainly formed by network of spectrin proteins attached to the RBC membrane lipid bi-layer. In this model RBC membrane is modeled as a 2D triangular network on the RBC surface. However, modeling RBC membrane using spectrin link lengths of $\mathcal{O}(100nm)$ will require > 25000 vertices per RBC triangulation [64, 65], which is quite an impractically high resolution for modeling flow with $\mathcal{O}(10^3)$ RBCs. The coarse-grained method, originally developed by Pivkin *et al.* [71] and improved by Fedosov *et al.* [72, 86, 87] can model RBC with a much smaller number of nodes (250-300) and can still capture the elastic response of the membrane [65].

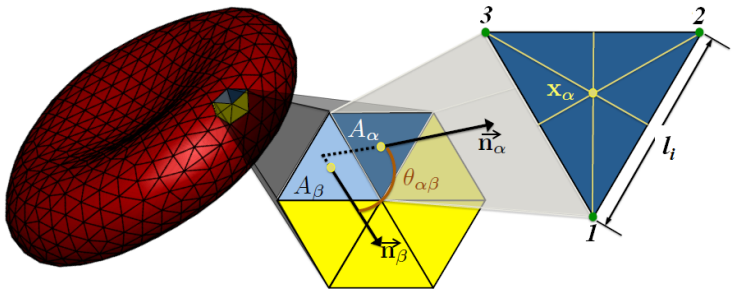

Figure 2.3: Triangulation of RBC in Spectrin-link method. α and β are two representative triangles. a, b and c are vertices and x_α is center of triangle α. A_α and A_β are the areas and, $\vec{n}_\alpha$ and $\vec{n}_\beta$ are the normal vectors of the triangles A_α and A_β with $\theta_{\alpha\beta}$ being the angle between them (figure adapted from Reasor [65])

.

In SL model each RBC membrane consists of a network of vertices $X_i, i \in 1 \cdots N_v$ connected through N_s springs of length $l_j, j \in 1 \cdots N_s$ forming Π surface triangles with areas of $A_\alpha, \alpha \in 1 \cdots \Pi$. Figure 2.3 shows the triangulation of and RBC in SL method. The area of triangle α is given by $A_\alpha = \frac{1}{2}|(X_2 - X_1) \times (X_3 - X_1)|$ and the total surface area is $A_{total} = \sum_{\alpha=1}^{\Pi} A_\alpha$. The total volume is given by $V_{total} = \sum_{\alpha=1}^{\Pi} \frac{1}{3}(X_\alpha \cdot \vec{n}_\alpha)$ where, $X_\alpha = \frac{1}{3}(X_1 + X_2 + X_3)$. The length of the link connecting vertices 1 and 2 is given by $l_i = |X_2 - X_1|$. The list of unique links and unique pairs of triangles sharing each link are stored in

a connectivity data file, which remains unchanged throughout the entire simulation as "no cell rupture" condition is assumed. RBC is triangulated using the hexagonal triangulation method as shown in 2.3.

The Helmholtz free energy $E(X_i)$ of membrane for SL method is given as the summation of contribution from in-plane $E_{in-plane}$, bending $E_{bending}$, area E_{area} and volume E_{volume} as following

$$E(X_i) = E_{in-plane} + E_{bending} + E_{area} + E_{volume} \tag{2.7}$$

$E_{in-plane}$ is given by the contribution of elastic energy stored in spectrin protein and hydrostatic energy stored in the membrane as given by

$$E_{in-plane} = \sum_{i \in N_s} U_{WLC}(l_i) + \sum_{\alpha \in \Pi} \frac{C}{A_\alpha} \tag{2.8}$$

The first sum in equation 2.8 represents the elastic energy stored in spectrin links described in terms of the wormlike chain (WLC) model [88, 89] as

$$U_{WLC}(l_i) = \frac{k_{in-plane} l_{max}}{4p} \frac{3x_i^2 - 2x_i^3}{1 - x_i} \tag{2.9}$$

where $x_i = \dfrac{l_i}{l_{max}} \in (0, 1)$, l_{max} is the maximum link length, $k_{in-plane}$ is in-plane SL model constant and p is the persistent length which is $\mathcal{O}(10nm)$. The attractive potential from WLC spring forces is balanced by a repulsive hydrostatic elastic in-plane energy described by

$$C = \frac{3\sqrt{3} k_{in-plane} l_{max}^3 x_0^4}{64p} \frac{4x_0^2 - 9x_0 + 6}{(1 - x_0^2)} \tag{2.10}$$

where $x_0 = \dfrac{l_0}{l_{max}}$, l_0 is the average link length $\dfrac{1}{N_s} \sum_{i \in N_s} l_i$.

The bending energy is defined as

$$E_{bending} = \sum_{adjacent\alpha,\beta\text{pair}} k_{bending}[1 - cos(\theta_{\alpha\beta} - \theta_0)] \tag{2.11}$$

where $k_{bending}$ is the discrete bending constant, $cos\theta_{\alpha\beta}$ is the instantaneous angle between adjacent triangles α and β (figure 2.3) and, θ_0 is the spontaneous (or initial) angle between the adjacent triangle pairs. $k_{bending}$ is related to average bending modulus k by $k_{bending} = \frac{2k}{\sqrt{3}}$ [87, 90].

The area constraint energy E_{area} is a non-physical energy imposed to ensure surface area conservation which is observed by the experimental study of Evans *et al.* [91]. Superiority of the SL model lies in the fact that it can capture this areas conservation phenomenon more accurately than the Hookean and neo-Hookean approach [65]. The area conservation energy is given by

$$E_{area} = \frac{k_{area}^{global}(A_{total} - A_{total}^0)^2}{2l_0^2 A_{total}^0} + \sum_{\alpha\in\Pi} \frac{k_{area}^{local}(A_\alpha - A_\alpha^0)^2}{2l_0^2 A_\alpha^0} \tag{2.12}$$

where A_{total} is the instantaneous surface area of RBC and A_{total}^0 is the initial surface area of RBC. A_α and A_α^0 are the instantaneous and initial surface area of triangle α. The first term in equation 2.12 represent global area conservation, whereas the second term represent local area conservation.

The volume conservation constraint is applied for similar reason as E_{area}, to ensure that the volume inside the triangulated RBC is constant. The fluid volume inside the RBC is enforced this way because of the incompressibility of the RBCs cytoplasm. The constraint due volume conservation is given by

$$E_{volume} = \frac{k_{volume}(V_{total} - V_{total}^0)^2}{2l_0^3 V_{total}^0} \tag{2.13}$$

where V_{total} is the instantaneous volume and V_{total}^0 is the total desired volume of RBC.

The values of constants $k_{in-plane}$, $k_{bending}$, k_{area} and k_{volume} are dependent on Boltzmann constant (k_B) and temperature (T) when using fluid domain methods such as dissipa-

tive particle dynamics (DPD) [92]. But, as the current LBM is independent of temperature and Brownian motions, the above mentioned constants arbitrarily chosen to match the non-dimensional parameters of interest. Constant $k_{in-plane}$ is chosen to match capillary number Ca_G and other constants are chosen to fulfill the condition $E_{volume} > E_{area} > E_{in-plane} > E_{bending}$ as proposed by Dupin *et al.* [58]. $k_{bending}$ can be chosen and modified to change the bending ratio χ independent of Ca_G. For RBC, the three important material properties are shear modulus (G), elastic area compression modulus (K) and Young's modulus (Y).

For SL model Pivkin *et al.* [71] expressed shear modulus of RBC membrane as

$$G = \frac{\sqrt{3}k_{in-plane}}{4pl_{max}x_0}\left(\frac{3}{4(1-x_0)^2} - \frac{3}{4} + 4x_0 + \frac{x_0}{2(1-x_0)^3}\right) \tag{2.14}$$

$G = 67 \times 10^{-7 J}/_{m^2}$ is used here, which is near the upper limit of the measured experimental value [93].

According to Fedosov *et al.*[87], the elastic area compression modulus is given as

$$K = \frac{\sqrt{3}k_{in-plane}}{4pl_{max}(1-x_0)^2}\left(\frac{3}{2}(6 - 9x_0 + 4x_0^2) + \frac{1 + 2(1-x_0)^3}{1-x_0}\right) + k_{area}^{local} + k_{area}^{global} \tag{2.15}$$

Based on the values of G and K, the Young's modulus is expressed as

$$E_y = \frac{4KG}{K+G} \tag{2.16}$$

and the Poisson ratio can be expressed as

$$\nu_p = \frac{K-G}{K+G} \tag{2.17}$$

For all simulations presented in this work, ν_p is chosen to be $\frac{1}{3}$.

2.2.3 Fluid-Solid Coupling

For an RBC triangulated with SL method, all the surface vertices move abiding by Newton's laws of motion

$$\frac{dX_i}{dt} = \vec{v}_i; \qquad\qquad M\frac{d\vec{v}_i}{dt} = F_i^m + F_i^{FS} + F_i^{PP} = F_i^{total} \tag{2.18}$$

where $\vec{v}_i$ is the velocity of vertex i and M is the fictitious mass at each vertex, F_i^{FS} is the force due to fluid solid interaction, F_i^{PP} are the forces due to particle-particle interactions which include lubrication, adhesion or contact. Details of the derivation of particle-particle interaction force components can be found in previous works [60, 65, 83]. The remaining term F_i^m represents forces due to the Helmholtz free energy contributions of the SL model (equation 2.7) and is expressed as

$$F_i^m = -\frac{\partial E(X_i)}{\partial X_i} \tag{2.19}$$

Detailed derivation for expression of F_i^m can be found in Appendix A of [94].

The fluid-solid coupling of LB-SL method is based on standard bounce back (SBB) implementation of the no-slip boundary condition that is quite common in LB methods [75, 76, 78, 80] and was implemented by MacMeccan *et al.* [60]. Traditional SBB methods are second order accurate, as exact location of fluid-solid boundary mid-point is known. But for the case of current work, as each of the RBCs can move through the cartesian LB grid, the boundary locations are not exactly at the mid-point between internal and external fluid nodes and hence the accuracy is reduced to first order in space [95, 96]. SBB procedure for SL RBC moving through fluid with a velocity $\vec{u}_b$ can be expressed as

$$f_i(\vec{X}, t+1) = f_{i'}(\vec{X}, t^+) + 6\rho\omega_i\vec{u}_b \cdot \vec{e}_i \tag{2.20}$$

where i' is the inward normal and i is the outward normal of SL membrane surface. In the same manner equal and opposite momentum transfers occur in the form of

$$\vec{F}^b = -2\vec{e}_i[f_{i'}(\vec{X}, t^+) + 3\rho\omega_i\vec{u}_b \cdot \vec{e}_i] \tag{2.21}$$

As SL RBCs are filled with fluid, the momentum transfer occurs twice for each link between interior and exterior fluid LB nodes. The force is interpolated to the nearest vertices as SL RBC is a triangulated approximation of the smooth RBC membrane. A linear interpolation is sufficient since the grid resolution of fluid is finer than that of the triangulated RBC membrane. The interpolated force is given by F_i^{FS} in equation 2.18. 12 lattice units are used to represent $4\mu m$ radius of the RBC and this resolution was previously tested by Macmeccan *et al.* [60]. The values of G and viscosity ratio (λ) lie within the experimentally measured values of RBC properties.

2.2.4 Equilibrium Red Blood Cell Shape

For obtaining baseline RBC mesh, a spherical capsule with 613 nodes is deflated to 59% of its original volume while keeping the surface area constant following the following same method as [69]. Schedule for deflation can be expressed as

$$V_{total}^0(t) = V_{total}^0(0) + \frac{t}{t_{final}}\left[V_{total}^0(t_{final}) - V_{total}^0(0)\right] \tag{2.22}$$

where $V_{total}^0(t_{final}) = 0.59V_{total}^{sphere}$. Here, $t = 0$ and $t = t_{final}$ are the initial and final time step and V_{total}^0 stands for total desired volume of RBC. Figure 2.4 shows the progressive deflation of a sphere to the equilibrium bi-concave shape of RBC. The bi-concave shape is an artifact of minimizing Helmholtz free energy, that also includes contribution due to bending. Value of bending modulus has very strong effect on the equilibrium shape of RBC. For $k_{bending} = 2.4 \times 10^{-19}J$ as suggested by Hwang *et al.*[97] the deflating sphere reaches to an equilibrium bi-concave shape of RBC. However, this shape is stable only at

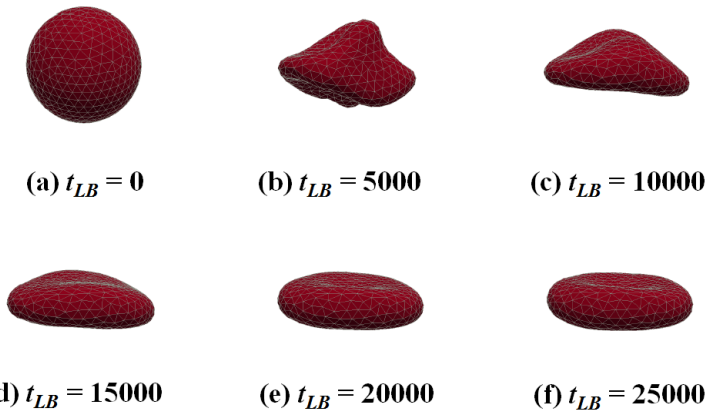

Figure 2.4: Deflation of sphere to equilibrium shape of RBC. Figure adapted from Reasor *et al.* [62].

stationary condition. Any small fluctuation or mesh irregularities will result in the RBC deform into a cup-like shape [65]. $k_{bending}$ value of $4.7 \times 10^{-18} J$, which is about an order of magnitude higher than the experimentally found value [97] produces a completely stable bi-concave RBC [69], and hence used for this work.

2.3 Simulation Setup

Flow of RBC suspensions between two parallel plates with spacing W has been simulated for multiple values of W, channel Reynolds number Re_c and volume fraction ϕ. Figure 2.5 shows geometrical configuration of the set up along with flow direction, axes directions and wall locations. For all the cases, the flow is driven by a constant body force in the axial direction X. Periodic boundary condition is applied in the flow (X-axis) and height-wise (Y-axis) direction and no-slip boundary condition in the span-wise (Z-axis) direction is applied through standard bounce back (SBB) condition of LBM, as shown in figure 2.5. So, the setup basically resembles with the case of flow between two parallel plates that are infinitely long and high and kept at distance W from each other, which is also known as Hele-Shaw flow. As there are walls (no-slip boundary condition) only in one axis orientation (Z), shear gradient and wall force will also be acting only along Z axis. So according to previous studies [46, 98] cell migration will be taking place only along

the width of the channel. Also experimentally it has been shown [46, 98] that when aspect ratio of channel greater than 2 $\left(\frac{H}{W} > 2\right)$, partile margination will be significant only in the direction of W. So the simulation setup used in this work is sufficient to mimic the flow inside a straight micro-channel with high aspect ratio. The spatial resolution for all the cases is $\frac{1}{3}\mu m$. A complete list of all the cases is given in table 2.1.

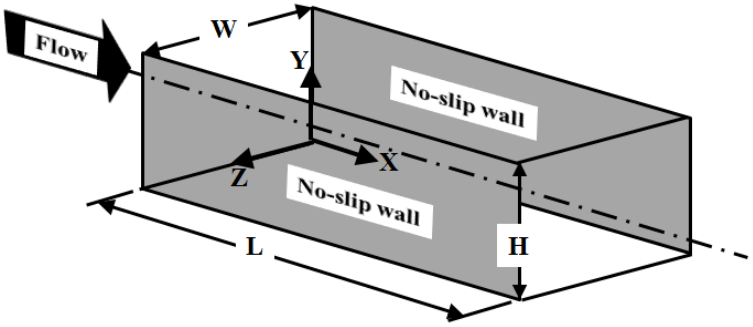

Figure 2.5: Microchannel configuration

As mentioned in section 2.2.4 triangular mesh with 613 nodes was used to resolve the RBC membrane. The inside viscosity of the RBC was five times higher than the surrounding liquid to mimic the RBC cytoplasm, i.e. $\lambda = \frac{\nu_{in}}{\nu_{out}} = 5$. RBC cytoplasm is set to $\rho = 1^{gm}/_{cm^3}$, equal to that of the plasma. For the purpose of this study, there will be two diffrent types of RBC, the ones with internal viscosity same as normal RBCs and the ones with cytoplasmic viscosity four times higher than the normal ones. As was mentioned in chapter 1, the main motivation for this research is sickle cell disease. Studies done by Byun *et al.* [99] found that, internal viscosity of RBC, which is one of the major determinant of RBC deformability, increases around four times when affected by SCD. For the rest of this chapter, the RBCs with normal internal viscosity will be referred to as *normal* RBC and the ones with higher internal viscosity will be referred to as *sickle* RBC. A list of all the RBC properties can be found in table 2.2. Values suggested for membrane shear modulus (G) and viscosity ratio (λ) are within the range of RBC properties measured experimentally by Byun *et al.* [99]. Area k_{area} and volume k_{volume} constraints are applied to ensure membrane inextensibility and cytoplasm incompressibility as mentioned in section 2.2.2

and their actual values are not important [62–64]. The prescribed value of $k_{bending}$ is about one order of magnitude higher than that found by experiments [97] and this is to ensure a stable bi-concave shape of RBCs [69].

To mimic dilute suspension cases where cell-cell interaction is not present, migration of single cell was studied in a channel with $W = 40\mu m$ to make sure there was no effect of intercellular interaction. In total eight simulations were run for the single cell case, four of them for $Re_c = 4$ and another four for $Re_c = 8$. For every Re_c category, there were two different types of cells, normal and sickle. For each of these cell types there were two cases, based on the initial location of the cells. Figure 4 shows the initial locations of all the cells. For the ease of visualization, snapshots of all the four cells were super imposed onto one and shown in a single channel. As can be seen from figure 2.6 (a), (b) and (c), there are two locations for normal cells - Normal 1 is seeded closer to the centerline of the channel and Normal 2 is seeded closer to the wall of the channel. Same is the case for the two sickle cells. This is done to observe, if initial location has any impact on the margination pattern of the cells in the absence of inter-cellular interaction.

For the semi-dense ($\phi = 10\%$) to dense suspension ($\phi = 30\%$) studies appropriate number of cells (based on value of ϕ) was seeded randomly in the whole domain at the beginning. Half of these seeded cells were chosen making sure that they were spread uniformly across the whole domain and their internal viscosity value was set to that of sickle RBCs as was done for dilute suspension cases. Figure 2.9 shows the initial simulation setup for the case of channel width $30\mu m$, $40\mu m$ and $60\mu m$.

Wall shear rate $\dot{\gamma}_w$ can be calculated from the equations

$$Re = \frac{u_{max} W}{\nu}; \qquad \dot{\gamma}_w = \frac{4}{W} u_{max} \tag{2.23}$$

Table 2.1: List of simulation cases

Domain size $(L \times W \times H)$ $(\mu m \times \mu m \times \mu m)$	Volume fraction $\phi(\%)$	Channel Reynolds number $Re_c = \frac{u_{max} W}{\nu}$	Shear rate $\dot{\gamma}_w = \frac{4}{W} u_{max}$ $(\times 10^3) sec^{-1}$	RBC Reynolds number $Re_{RBC} = \frac{\dot{\gamma}_w a_{RBC}^2}{\nu}$	Capillary number $Ca_G = \frac{a_{RBC} \dot{\gamma}_w \mu}{G}$
Dilute suspension					
$40 \times 40 \times 30$		4	10	0.042	4.328
		8	20	0.084	8.656
Dense suspension					
$30 \times 30 \times 30$	10	2	8.888	0.074	3.84
	20				
$40 \times 40 \times 30$	10	1	2.5	0.021	1.082
	10	2	5	0.042	2.164
	20				
	30				
	10	4	10	0.084	4.328
	20				
	30				
$60 \times 60 \times 30$	10	2	2.222	0.018	0.96
	20	10	11.111	0.093	4.80

Table 2.2: Red blood cell properties

Cell type	Bending modulus $k_{bending}(J)$	Shear modulus $G\left(\frac{J}{m^2}\right)$	Area constraint coefficient $k_{area}\left(\frac{J}{m^2}\right)$	Volume constraint coefficient $k_{volume}\left(\frac{J}{m^2}\right)$	Viscosity ratio $\lambda = \frac{\nu_{in}}{\nu_{out}}$
Normal	4.7×10^{-18}	67×10^{-7}	1.7×10^{-5}	50.9	5
Sickle					20

where W is the channel width, $\nu = 10^{-6} m^2/sec$ is the viscosity of the surrounding media of RBCs (here water). From the shear rate calculated in equation 2.23, particle / RBC Reynolds number Re_{RBC} can be calculated as

$$Re_{RBC} = \frac{\dot{\gamma}_w a_{RBC}^2}{\nu} \tag{2.24}$$

where $a_{RBC} = 2.85\mu m$ is the effective radius of RBC calculated based on RBC sphere volume given by

$$V_{RBC} = \frac{4}{3}\pi a_{RBC}^3 \tag{2.25}$$

Capillary number Ca_G, which is a measure of cell deformability, can be calculated as

$$Ca_G = \frac{a_{RBC}\dot{\gamma}_w \mu}{G} \tag{2.26}$$

where, $\mu = 1.2 \times 10^{-3} N.sec/m^2$ is the dynamic viscosity of the surrounding media and $G = 67 \times 10^{-7} J/m^2$ is the membrane shear modulus. Calculated values of $\dot{\gamma}_w$, Re_{RBC} and Ca_G for different flow conditions are summarized in table 2.1.

For dilute suspension cases, non-dimensional trajectories of individual cells were observed, which is basically the lateral displacement of cell from the center line of the channel normalized by half of the channel height. Lateral displacement is defined as

$$D(t) = z(t) - \frac{W}{2} \tag{2.27}$$

where, $z(t)$ is the individual cell location at time t. So non-dimensional quantity will be $\frac{D(t)}{W/2}$.

For dense suspension cases, the average of the lateral displacement of cells from centerline is used as the measure of margination. It is defined as

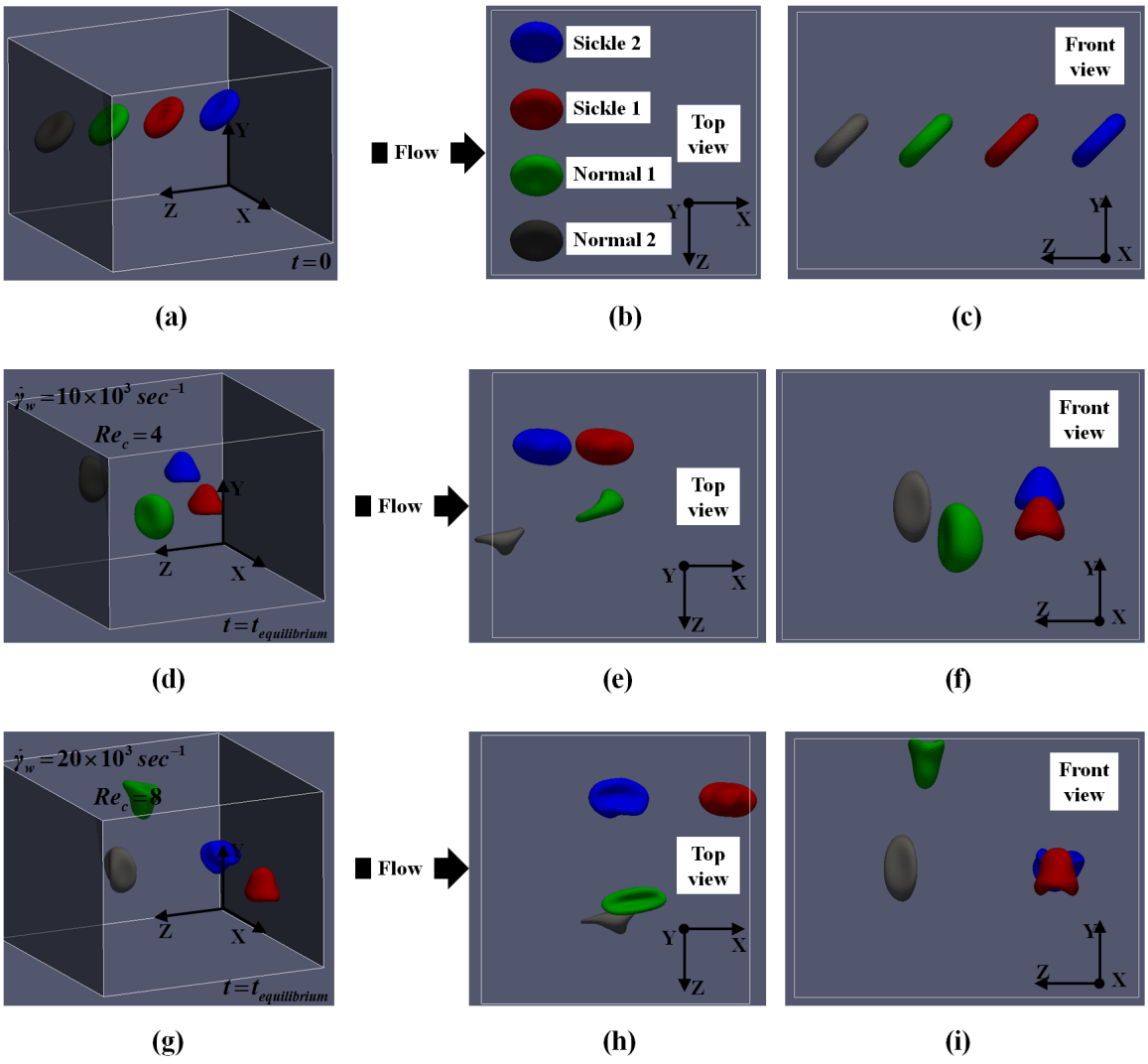

Figure 2.6: Single cell simulation cases. (a), (b) and (c) are snapshots at initial time step for both $Re_c = 4$ and $Re_c = 8$ cases. (d), (e) and (f) are snapshots at a time step after the cells have reached their equilibrium time step for the $Re_c = 4$ case. (g), (h) and (i) are snapshots at a time step after the cells have reached their equilibrium time step for the $Re_c = 8$ case. Transparent dark planes in the isometric views (a, d and g) represent no-slip walls.

$$\overline{D}(t) = \left|\overline{z(t) - \frac{W}{2}}\right| = \frac{1}{N}\sum_{i-1}^{N} D_i(t) \tag{2.28}$$

where $\overline{D}(t)$ is the average distance of the cells from centerline at time t. N is the total number of cells and $D_i(t)$ is the distance of cell i from the channel centerline.

For comparison of margination between different cases, normalized lateral displacement

$\frac{\overline{D}(t)}{W/2}$ is used. Also, the difference between the average trajectories of stiff and normal cells as given by $\frac{\overline{D}_{sickle}(t) - \overline{D}_{normal}(t)}{W/2}$ is used as a measure of strength of separation between stiff and normal cells.

2.4 Results

2.4.1 Effect of internal viscosity on RBC deformation

Earlier studies [32, 37–39] have shown that deformable vesicles with higher internal viscosity are less deformable compared to the ones having lower internal viscosity. Experimentally it was also shown that RBCs with higher internal viscosity have lower deformability [99]. To validate that the observation for vesicles also holds true for RBCs and to understand the deformation characteristics of RBC based on their internal viscosity, benchmark cases from previous works [62, 100] studying parachuting behavior of RBC in microcapillary were run. Figure 2.7(a) shows snapshots of parachuting for the two cell types at different time steps. As can be seen, the deformation of sickle RBC is smaller compared to the normal one. Also, the normal RBC moved further in the channel compared to the sickle one because of less resistance arising from smaller frontal area. Variation of deformation index $\left(\Gamma = \frac{L}{D}\right)$, a measure of deformability [62, 100] against flow velocity for the two cell types are plotted in figure 2.7(b) and it is observed that the higher internal viscosity RBC is less deformable compared to the RBC with normal internal viscosity.

2.4.2 Dilute Suspension

Dilute suspension simulations were run for two values of Re_c to study effect of shear rate on the margination of RBCs with different internal viscosity. A listing of all these cases can be found in table 2.1. Snapshots of the initial time step and at a time step after the cells have reached their equilibrium positions are shown in figure 2.6 (d - i) for different Re_c case. Figure 2.8 shows the non-dimensional trajectories of the individual cells.

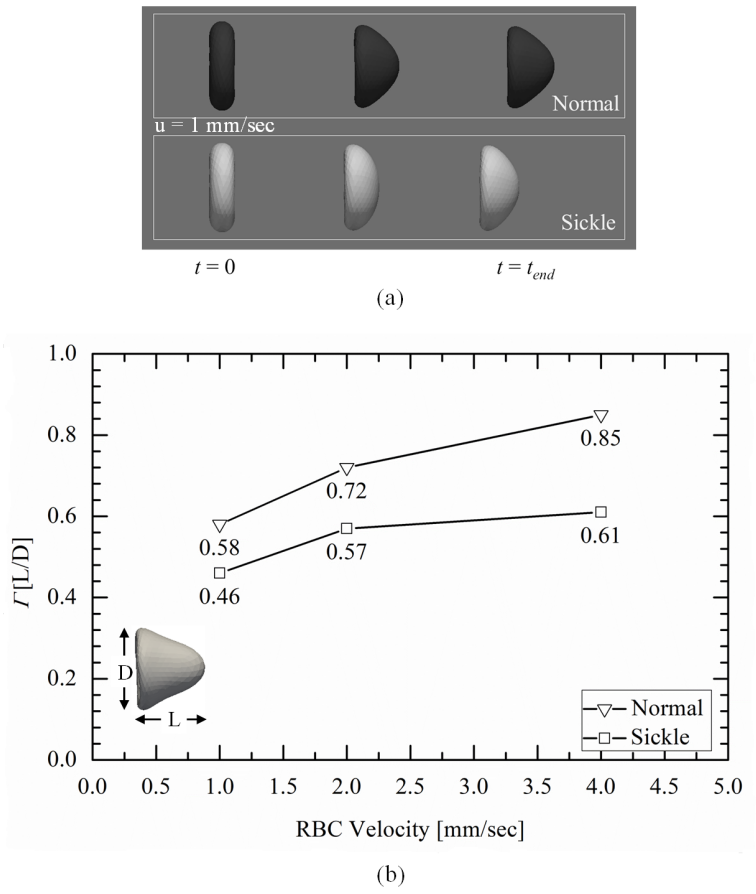

Figure 2.7: Parachuting of RBC in micro-capillary flow. (a) Snapshots of RBC shape at three time points. (b) Variation of RBC deformation with flow velocity

.

As can be observed for both the cell types, normal and sickle, cells are laterally migrating from their initial location to an equilibrium position somewhere between the central plane $\left(\frac{D}{W/2}\right) = 0$ and the wall $\left(\frac{D}{W/2}\right) = 1$, which is an expected behavior observed in earlier studies [34–38, 40, 51, 52]. Between cells that are of two different types (sickle and normal), but have the same initial transverse location (i.e. initial $\frac{D}{W/2}$ is same for both types), the one with higher internal viscosity stabilizes closer to the wall and the one with normal viscosity has equilibrium location closer to the center line of the channel. As can be seen from figure 2.6 (d - i), between the pair Normal 1 and Sickle 1, Normal 1 stabilizes near the center line whereas Sickle 1 stays closer to the wall when it reaches equilibrium. Same is true for the pair Normal 2 and Sickle 2.

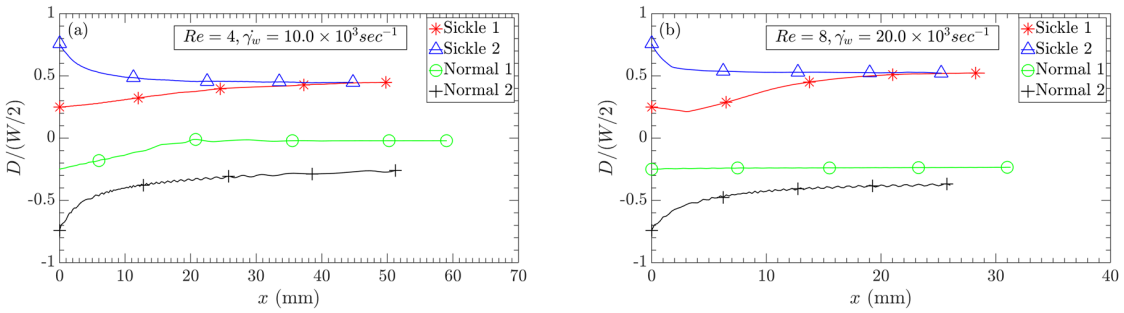

Figure 2.8: Non-dimensional lateral trajectories of individual cells. (a) for $Re_c = 4$, (b) for $Re_c = 8$

.

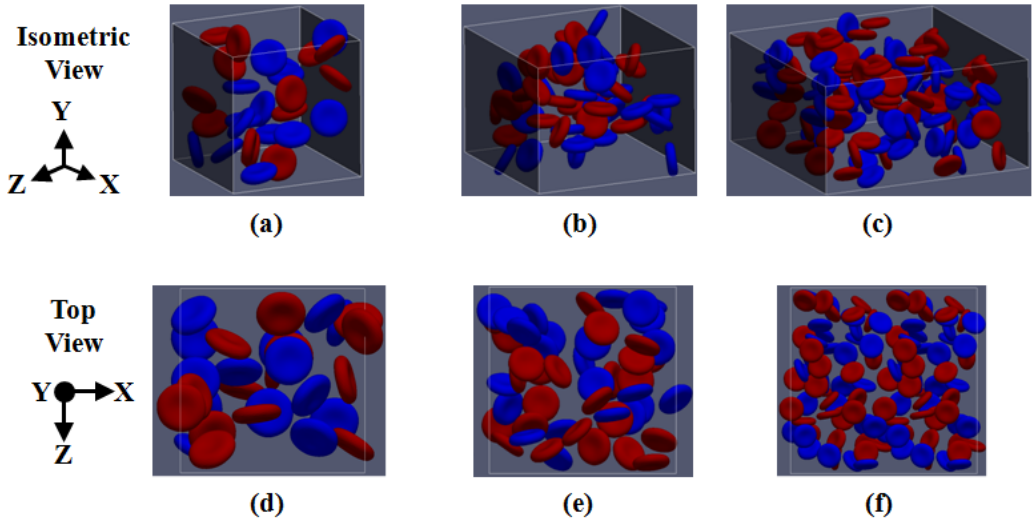

Figure 2.9: Snapshots right after cell seeding. (a), (b) and (c) are isometric views and, (d), (e) and (f) are top views of $30\mu m \times 30\mu m \times 30\mu m$, $40\mu m \times 40\mu m \times 30\mu m$ and $60\mu m \times 60\mu m \times 30\mu m$ cases respectively. Red cells represent normal RBCs, and blue cells represent sickle RBCs. Transparent dark planes in a, b and c represent no-slip walls.

Comparing figure 2.8 (a) and (b), the most prominent effect of increasing Re_c appears to be that the cells reach to their equilibrium locations much faster for higher Re_c cases, regardless of their type and initial locations. It also appears that for the range of Re_c considered for this work, the equilibrium positions for both the cell types move towards the wall as Re_c increases. As explained in section 2.1, in the absence of any cell-cell interaction, a deformable paticle migrates in transverse direction under the effect of two opposing forces, F_S and F_W (2.1) and eventually settles down to (or oscillates about) an

equilibrium location where F_S and F_W balances each other. Increasing Re_c results in increase of F_S, which pushes the cell further towards the wall and the inidividual cells ends up in an equilibrium location closer to the wall.

From the margination pattern observed in 2.8, it appears that for the Re_c range considered in this work and in the absence of any intercellular interaction, RBCs with higher internal viscosity have pretty much the same lateral equilibrium position regardless of their initial seeding location. The normal RBCs, however seem to have more like an *equilibrium zone* around the centerline rather than a particular location. This variation is because of difference in deformability between normal and sickle RBCs. In the absence of any cell-cell interaction, cell deformability is the only factor to influence equilibrium locations of RBCs for a particular Re_c. Cells with lower deformability will cause lower disturbance in the fluid around them and hence will migrate to the same or nearly same location at equilibrium regardless of where they were seeded initially. Normal RBCs can deform more, which causes higher disturbance in the fluid around the cells. Normal RBCs originally seeded at different locations will have different deformation pattern and hence will migrate to different equilibrium locations giving rise to the *equilibrium zone*. So it can be inferred that less deformable RBCs will have a narrower *equilibrium zone* compared to the more deformable ones.

2.4.3 Dense Suspension

The dense suspension cases are the ones, where cell-cell interactions are present and play a significant role in lateral cell margination. As can be seen from the list of all the cases provided in table 2.1, simulations with ϕ varying from 10% to 30% have been run for different Re_c and cross-sectional sizes of channels. In figure 2.10 non-dimensional average lateral displacement $\left(\frac{\overline{D}}{W/2}\right)$ and standard deviation of that quantity are plotted against time

for two cases. Standard deviation for the above stated quantity can be expressed as

$$\sigma = \sqrt{\frac{1}{N-1}\sum_{i=1}^{N} |D_{ND_i} - \overline{D}_{ND}|^2} \tag{2.29}$$

where, $D_{ND_i} = \dfrac{D(t)}{W/2}$ and $\overline{D}_{ND} = \dfrac{\overline{D}(t)}{W/2}$. Standard deviation σ represents cell fluctuation from the average trajectory. As expected, σ decreases with time as the cells progress to their equilibrium loications. This pattern of σ diminishing with time was observed for all the simulation cases run here and the two cases presented here are representative of all of them. The extent to which σ for each cell type decreases is dependent on how dispersed were the cells initially and the cell-cell interaction. Also because of the presence of cell-cell interaction cells of each type will keep moving within their *equilibrium zone* and hence σ will keep on oscillating even after all the cells have reahced their locations.

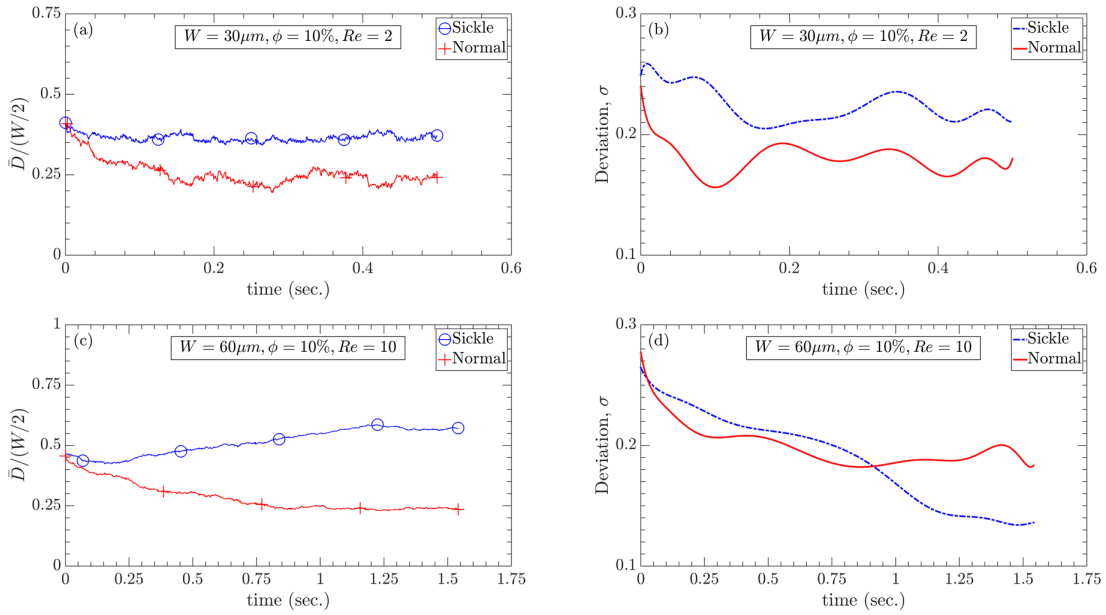

Figure 2.10: Variation of non-dimensional lateral displacement (a) and standard deviation of non-dimensional lateral displacement (b) with time

Effect of RBC Internal Viscosity

To study the effect of RBCs internal viscosity on margination of RBCs when intercellular collision is significant, the case of RBCs flowing through $60\mu m \times 60\mu m \times 30\mu m$ channel with $Re_c = 10$ at volume fraction $\phi = 10\%$ is considered. As shwon in table 2.1, the corresponding wall shear rate $\dot{\gamma_w} \approx 11000 sec^{-1}$ which is calculated based on matching channel Reynolds number Re_c and RBC shear capillary number Ca_G. Based on RBC effective diameter value of $a_{RBC} \approx 2.85\mu m$ [64, 65] a total of 112 RBCs make up 10% volume fraction.

Figure2.11 contains snapshots of the simulation taken from two different viewpoints, at initial time step (a and c) and, at a time step after both the cell types seem to have reached their transverse equilibrium position (b and d). As can be seen from figure 2.11 (b) and (d), most of the normal cells accumulated closer to the centerline while the sickle ones diffuse to outer region next to the walls following RESID mechanism as proposed by Mehrabadi *et al.* [64]. Figure 2.11 (e) shows the non-dimensional average lateral displacement of normal RBCs from their initial positions demonstrating that the average trajectory for the sickle RBCs is moving towards the wall whereas that for the normal RBCs reaching a somewhat steady state closer to the channel center. The observed margination pattern for dense cell suspension is very similar to that observed for dilute suspension in this work and earlier works [32, 35–38, 40, 51, 52]. Interestingly this λ dependent margination pattern of RBCs in dense suspension is also qualitatively similar to the stiffness/deformability dependent cell margination as observed in earlier studies [41, 46, 53, 54, 56, 64] for microchannel flows. This confirms cytoplasmic viscosity being one of the major factors for defining RBCs overall deformability. Similar λ dependent margination phenomenon has been observed for all the simulation cases considered for this work and the case described in this section is representative of all of them.

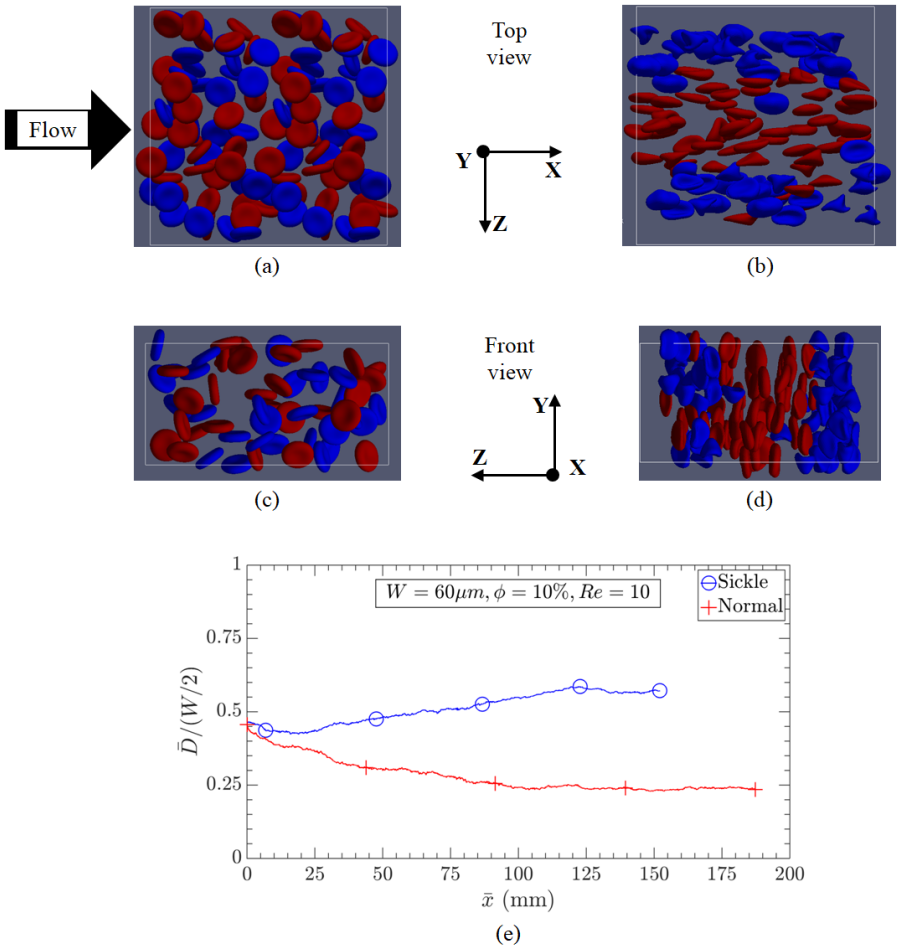

Figure 2.11: Internal viscosity dependent margination of RBCs for the case of $60\mu m \times 60\mu m \times 30\mu m$ and $Re_c = 10$. Figure (a - d) are snapshots of first (a and c) and last (b and d) time steps. Figure (e) shows the non-dimensional average lateral displacement of the two cell types. Red represents normal RBC, blue represents sickle RBCs.

Effect of Cell Mixture

Migration of RBCs under three different cell mixture conditions was studied to check, how RBCs migrate. The three cases were: (i) all normal, (ii) all sickle and (iii) half and half mixture of normal and sickle RBCs. Figure 2.4.3 (a), (b) and (c) are the snapshots of the initial time step (top row) and of time step where the cells reached their lateral equilibrium locations (bottom row) for the three above mentioned cases respectively. As can be observed from top row images of figure 2.4.3 (a), (b) and (c), initial locations of cells for the all three cases are exactly same. Equilibrium positions of cells depending on

their internal viscosity and type of cell mixture are different (bottom row of figure 2.4.3 (a), (b) and (c)).

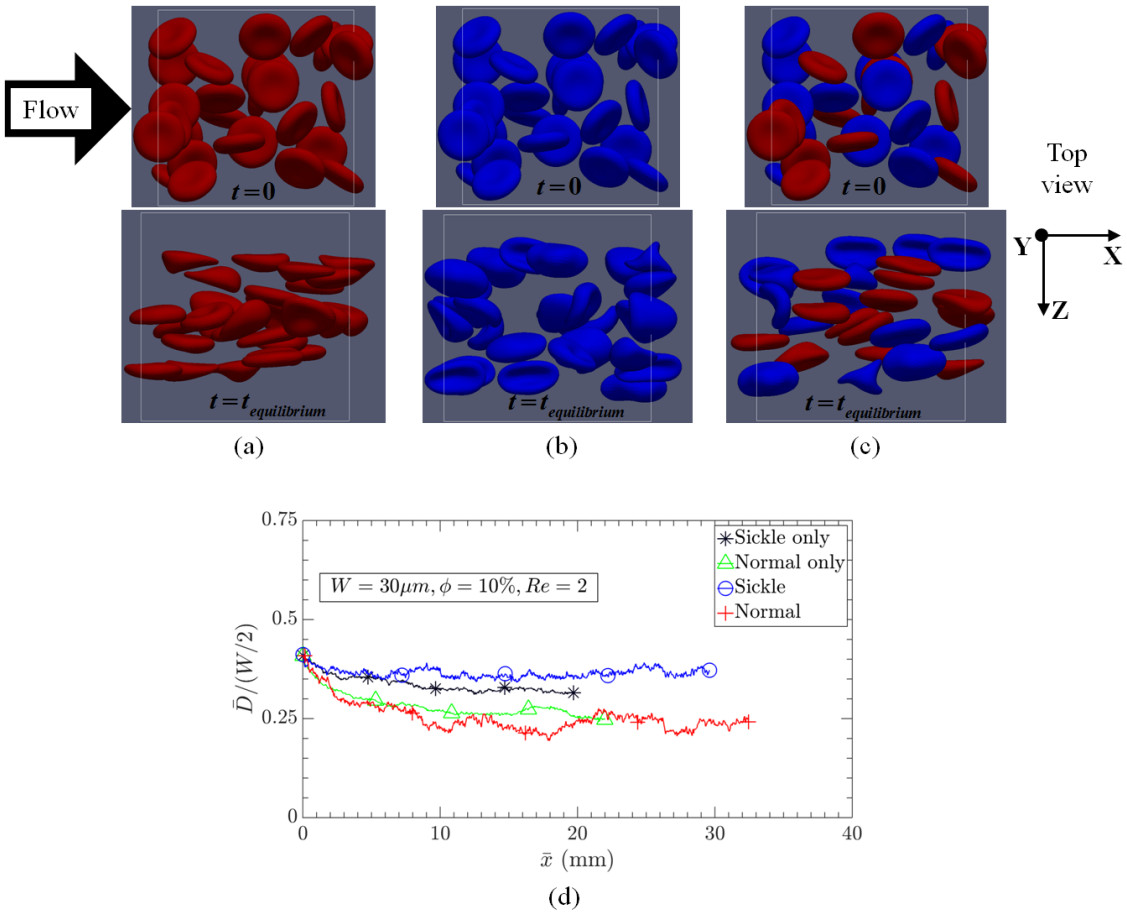

Figure 2.12: Effect of cell type mixture on the margination of cells for $30\mu m \times 30\mu m \times 30\mu m$, $Re_c = 2$ and $\phi = 10\%$ case. Top row of (a), (b) and (c) are snapshots at initial time step for normal-only, sickle-only and normal-sickle mixture cases respectively. Bottom row of (a), (b) and (c) are snapshots taken after the cells have reached their equilibrium position for normal-only, sickle-only and normal-sickle mixture cases respectively. Figure (d) shows non-dimensional average lateral displacement of cells under three different cell mixture conditions.

Figure 2.4.3 (d) shows the normalized average lateral migration of the cells from their initial locations with respect to the average distance covered in the flow direction. Snapshots of cell margination for normal-only and sickle-only cases at equilibrium time step (bottom row figures of figure 2.4.3 (a) and (b)) and the two different migration curves for normal-only and sickle-only cases (2.4.3 (d)) support the earlier observation that cells with

different internal viscosity migrate to different equilibrium locations. When the mixture of cell types come into play, a larger spacing between curves corresponding to sickle and normal RBCs compared to the spacing between sickle-only and normal-only cases is observed. In particular it is observed that, the average trajectories of the normal cells for the normal-only and normal in mixture case are almost overlapping, whereas for sickle-only and sickle in mixture cases, the trajectories are spaced apart, the latter being further from the center line. This indicates that for dense suspensions, inter-cellular collision is a significant factor in margination of cells with different cytoplasmic viscosity in addition to the balancing mechanism of forces F_S and F_W as described before. For the dense suspension, RBCs with normal cytoplasmic viscosity gather closer to the center and the ones with higher internal viscosity (higher λ) get out of the central core following the RESID mechanism explained by Mehrabadi *et al.* [64]. The margination pattern observed is very similar to that as explained by Munn *et al.* [101] for segregation of particles with different deformability in rectangular microchannel flow, which is an indication that cells with higher cytoplasmic viscosity behave like less deformable or stiffer cells.

Cell-free layer

As can be seen from snapshots presented in figure 2.11 and , cell-free layers are formed next to the channel walls resembling the observations from previous works [62–64]. Mehrabadi *et al.* [64] in their study of RBC and platelet mixture observed that platelets diffuses to the RBC-free layer and hence it is an important parameter for study of platelet margination. The current study focuses on margination of RBCs and as both of the RBC types are deformable, there was no migration of sickle or less deformable RBCs to the cell-free layer. From figure2.13 non-dimensional cell-free layer thickness $\left(\frac{\delta}{a_{RBC}}\right)$ is observed to follow a power-law relation with RBC capillary number Ca_G as was done in previous works [64, 102].

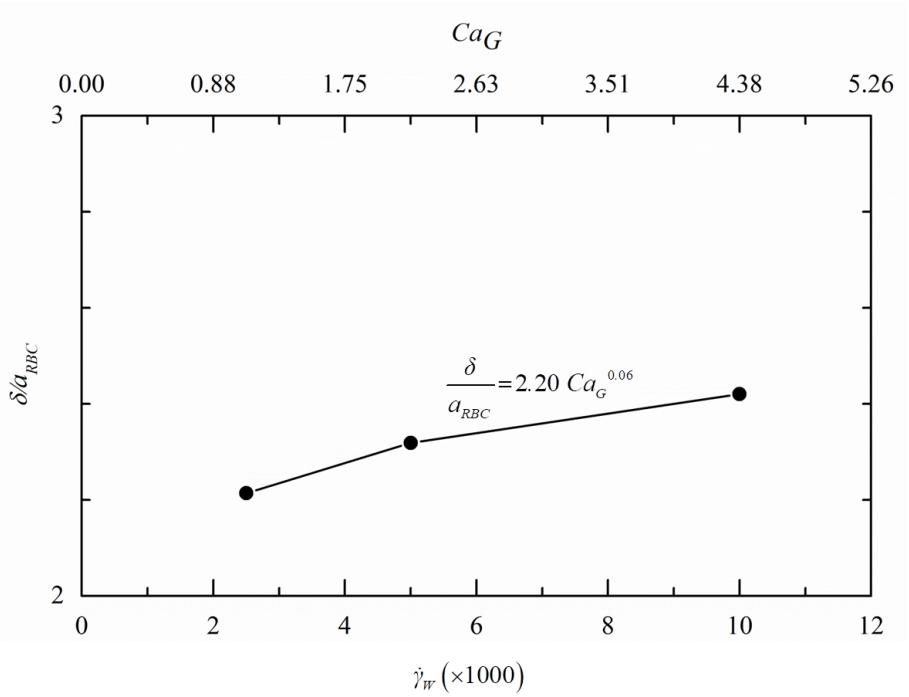

Figure 2.13: Effect of wall shear rate $(\dot{\gamma}_w)$ and RBC capillary number (Ca_G) on cell-free layer thickness

Effect of Confinement Ratio

Confinement ratio is a non-dimensional measure of channel size and is defined as $\frac{2a_{RBC}}{W}$. Higher value of it indicates channel with smaller width and vice versa given a particular value of particle/cell radius. Average non-dimensional lateral displacement as a function of average distance travelled along the flow direction comparing cases $W = 60\mu m$ and $W = 40\mu m$ for $\phi = 10\%$ (2.14 (a)) and cases $W = 40\mu m$ and $W = 30\mu m$ for $\phi = 20\%$ (2.14 (c)) is plotted. As can be observed from 2.14 (a) and (c), both cases of $\phi = 10\%$ and $\phi = 20\%$, margination is faster in channels with smaller cross-section compared to the ones with larger cross-section, which is in agreement with the observation of Mehrabadi *et al.* [64]. The parameter $\frac{\overline{D}_{sickle} - \overline{D}_{normal}}{W/2}$, defined previously as a measure of margination strength, is plotted in figure 2.14 (b) and (d). As can be seen from both these figures, for channel with stronger confinement ratio, the separation between average trajectories of normal and sickle RBCs is stronger. The fact that it is observed for both $\phi = 10\%$ and

$\phi = 20\%$ demonstrates that, this phenomenon is independent of cell volume fraction (ϕ) as long as it is high enough for cell-cell interaction to be significant. This is also an indication of wall force playing an important role on the margination. From design perspective of a microfluidic channels for RBC separation based on deformability, this observation indicates that a channel with smaller cross-section will provide a faster and stronger separation between the cell types. However because of practical factors like expected throughput, pressure withstanding capability of the device, maximum allowable shear rate and channel clogging there needs to be a compromise on how small of a cross-section is feasible.

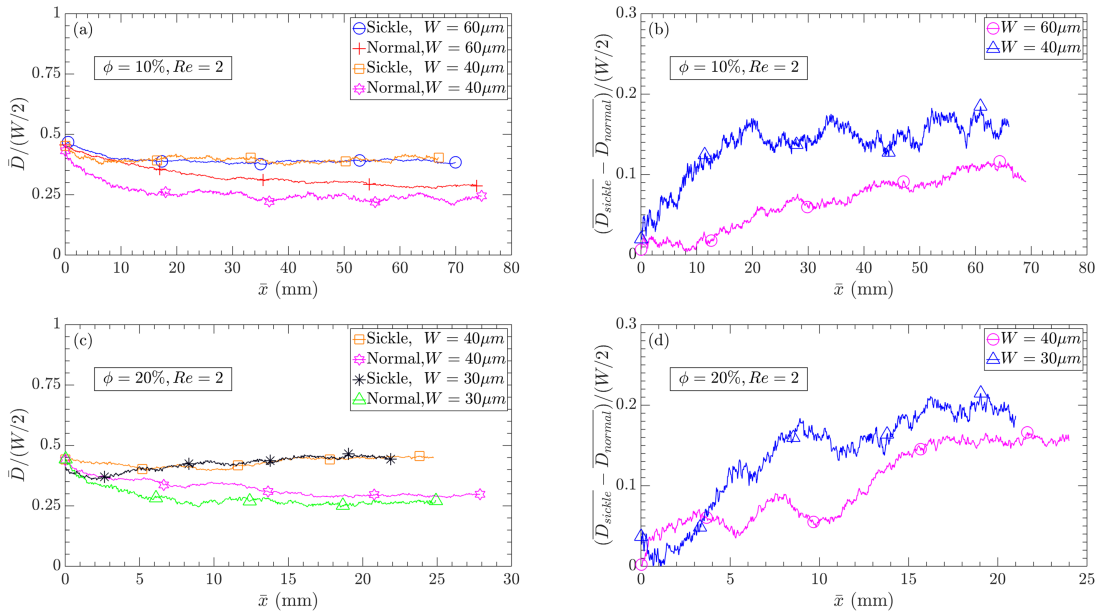

Figure 2.14: Effect of confinement ratio on margination. Figure (a) and (c) show average non-dimensional lateral displacement of cells. Figure (b) and (d) show distance between lateral displacement of sickle and normal cells.

Mehrabadi *et al.* [64] in their work, proposed a scaling law based on the quantity *average relative lateral displacement* of cells, which is defined as

$$\Delta\overline{D} = \overline{D}(t) - \overline{D}(0) \tag{2.30}$$

where, $\overline{D}(t)$ is the average distance of cells from centerline at time t and $\overline{D}(0)$ is that at the

beginning $(t = 0)$. They are calculated as,

$$\overline{D}(t) = \left|\overline{z(t) - \frac{W}{2}}\right| \text{ and,} \overline{D}(0) = \left|\overline{z(0) - \frac{W}{2}}\right| \tag{2.31}$$

where $z(t)$ is cell location at time t, and $z(0)$ is initial cell location.

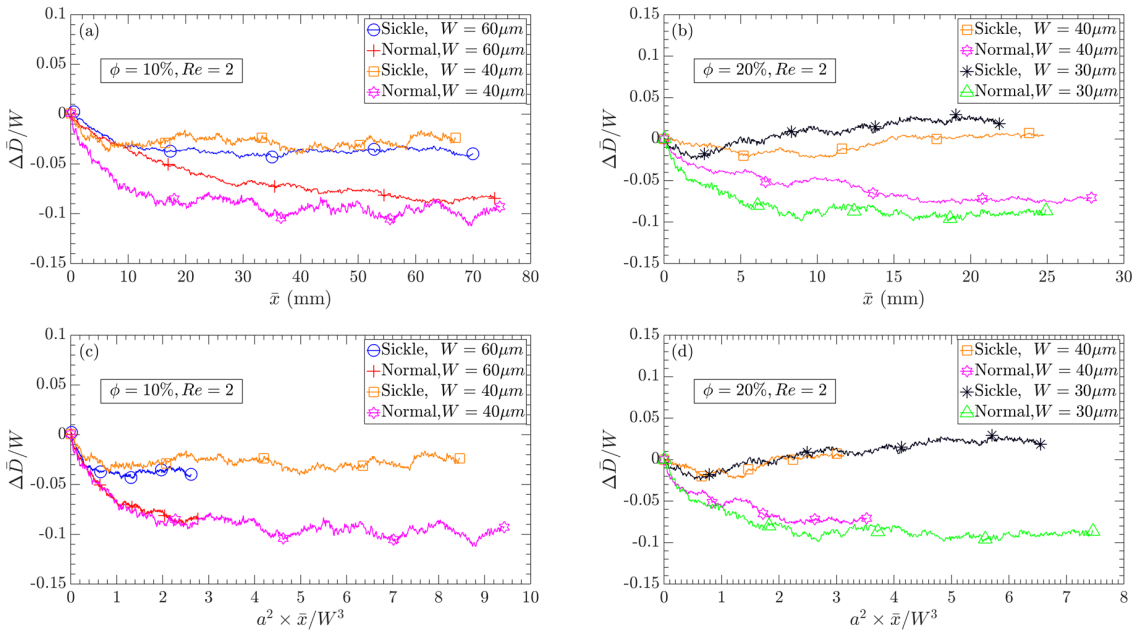

Figure 2.15: Scaling law validation for different cases. Figure (a) and (b) show average relative lateral displacement of cells. Figure (c) and (d) show the scaling law.

The proposed law states that, the lataeral displacement $\Delta\overline{D}$ of particles from their initial position scales as $\left(\frac{\Delta\overline{D}}{W}\right) \sim 12K\frac{a_{RBC}^2\overline{x}}{W^3}$, where $\overline{x}$ is the average distance traveled by particles in flow direction, and K is a non-dimensional constant accounting for dependence of shear-induced diffusion coefficient on particle volume fraction, particle deformability and other particle parameters as shape [103–105]. From the scaling law, the expression for the margination development length, L_D (the length over which the average relative distance of particles from wall is $\sim W$, i.e. $L_D = \overline{x}|_{\Delta\overline{D}\sim W}$ was derived as $L_D \sim \frac{W^3}{12Ka_{RBC}^2}$. However, Mehrabadi *et al.* [64] compared margination behavior between normal deformable RBCs and platelets modeled as rigid oblate spheroids. To investigate whether or not the scaling law still holds when comparing margination behavior of cells with same size and

shape but different internal viscosity, the parameter $\frac{\Delta\overline{D}}{W}$ is plotted against $\frac{a_{RBC}^2\overline{x}}{W^3}$ comparing $H = 60\mu m$ and $40\mu m$ cases for $\phi = 10\%$ (figure 2.15 (c)) and comparing $H = 40\mu m$ and $H = 30\mu m$ cases for $\phi = 10\%$ (figure 2.15 (d)). For all the cases, as can be seen from figure 2.15 (c) and (d) the average trajectories for both the normal and sickle RBCs collapse, thereby confirming that the scaling law proposed by Mehrabadi *et al.* [64] still holds for cells with same shape and size but different internal viscosity.

Effect of Shear Rate

Effect of shear rate $(\dot{\gamma}_w)$ on margination of RBCs has been studied where $(\dot{\gamma}_w)$ is calculated from channel Reynolds number (Re_c) using equation 2.23. Figure 2.16 shows the effect of shear rate on cellular margination for different channel widths (W) and volume fraction of cells (ϕ). Two types of plots are presented to explain the results. First type is, plots showing average nondimensional lateral cellular displacement between different cases $\frac{\overline{D}(t)}{W/2}$ (figure fig:shearrate (a), (c) and (e)). Second types of plots are the ones showing spacing between average trajectories of sickle and normal cells $\frac{\overline{D}_{sickle}(t) - \overline{D}_{normal}(t)}{W/2}$ (figure 2.16 (b), (d) and (f)) for each of the cases compared in figure 2.16 11 (a), (c) and (e). As can be observed from Figure 11 (a) and (b), for a particular channel size (here, $40\mu m \times 40\mu m \times 30\mu m$) with shear rates going higher, the segregation of cells of different internal viscosity gets stronger. Comparing figure 2.16 (a) and (b), which are plotted for $\phi = 10\%$ and 2.16 (e) and (f), which are plotted for $\phi = 20\%$, it can be concluded that the observed phenomenon of shear rate induced separation enhancement is independent of the volume fraction, provided that value of ϕ is high enough for inter-cellular interaction to be present. From figure 2.16 (a), (c), and (e) it can be seen that it is mainly the lateral displacement of RBCs with higher internal viscosity that gets influenced with shear rate, while the average lateral displacement of the normal RBCs is not strongly affected by the shear rate .

Snapshots of cells across the cross section of channels for the above mentioned cases at different time points can be seen from figure 2.17. In comparison to platelet (modeled

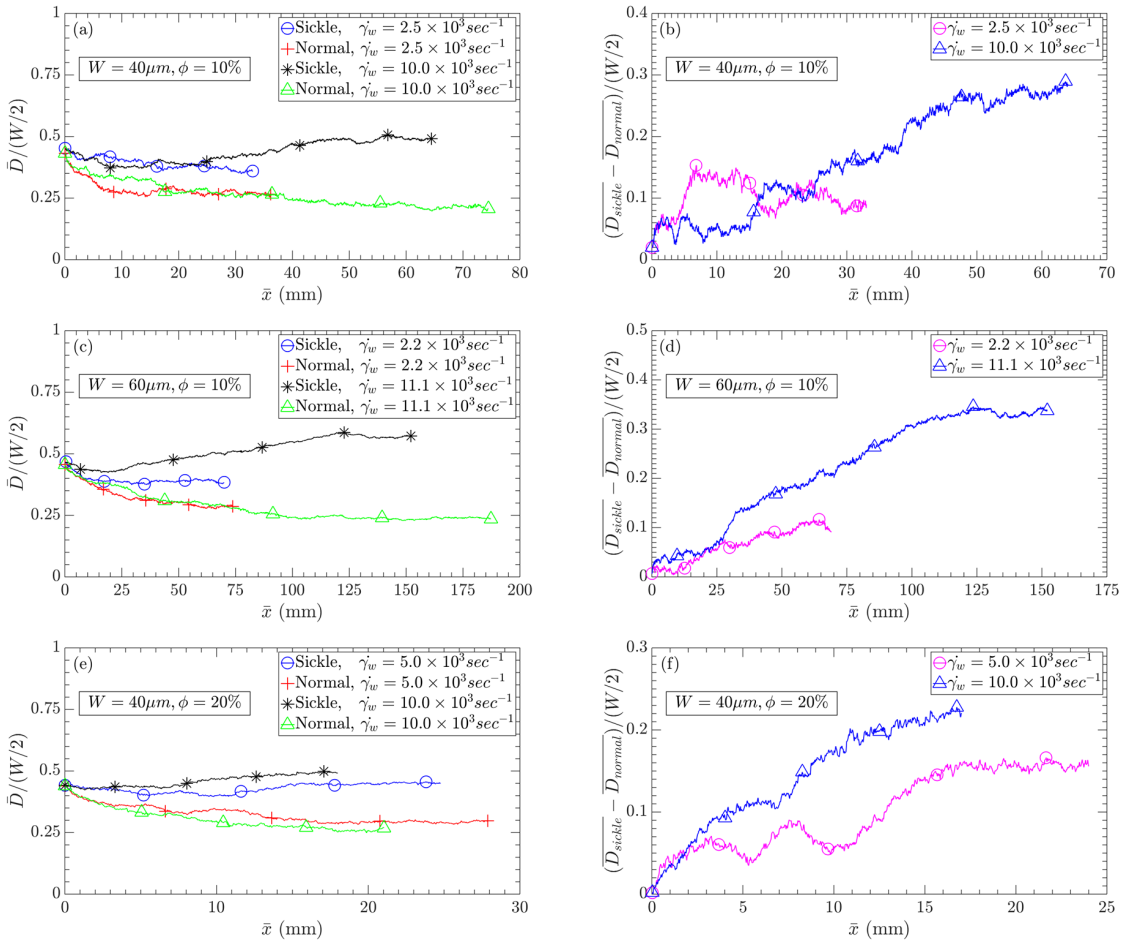

Figure 2.16: Effect of shear rate on cellular margination. Figure (a), (c) and (e) show average non-dimensional lateral displacement of RBCs. Figure (b), (d), and (f) show distance between average trajectories of sickle and normal RBCs.

as solid particle) margination [64], the effect of shear rate on margination of deformable particles with higher internal viscosity seems to be stronger. We believe deformation of the RBCs with higher internal viscosity is the primary reason behind the observed enhanced margination of these cells under higher shear rate. As stated previously, earlier studies [28, 31, 57] have shown that rigid particles do not experience lateral margination for stokes flow whereas studies [32, 35–38, 40, 51, 52] shown that liquid droplets always marginate laterally regardless of the Reynolds number regime. As can be seen from table 2.1, all of simulations reported in this paper are conducted at very small particle Reynolds number (Re_{RBC}).

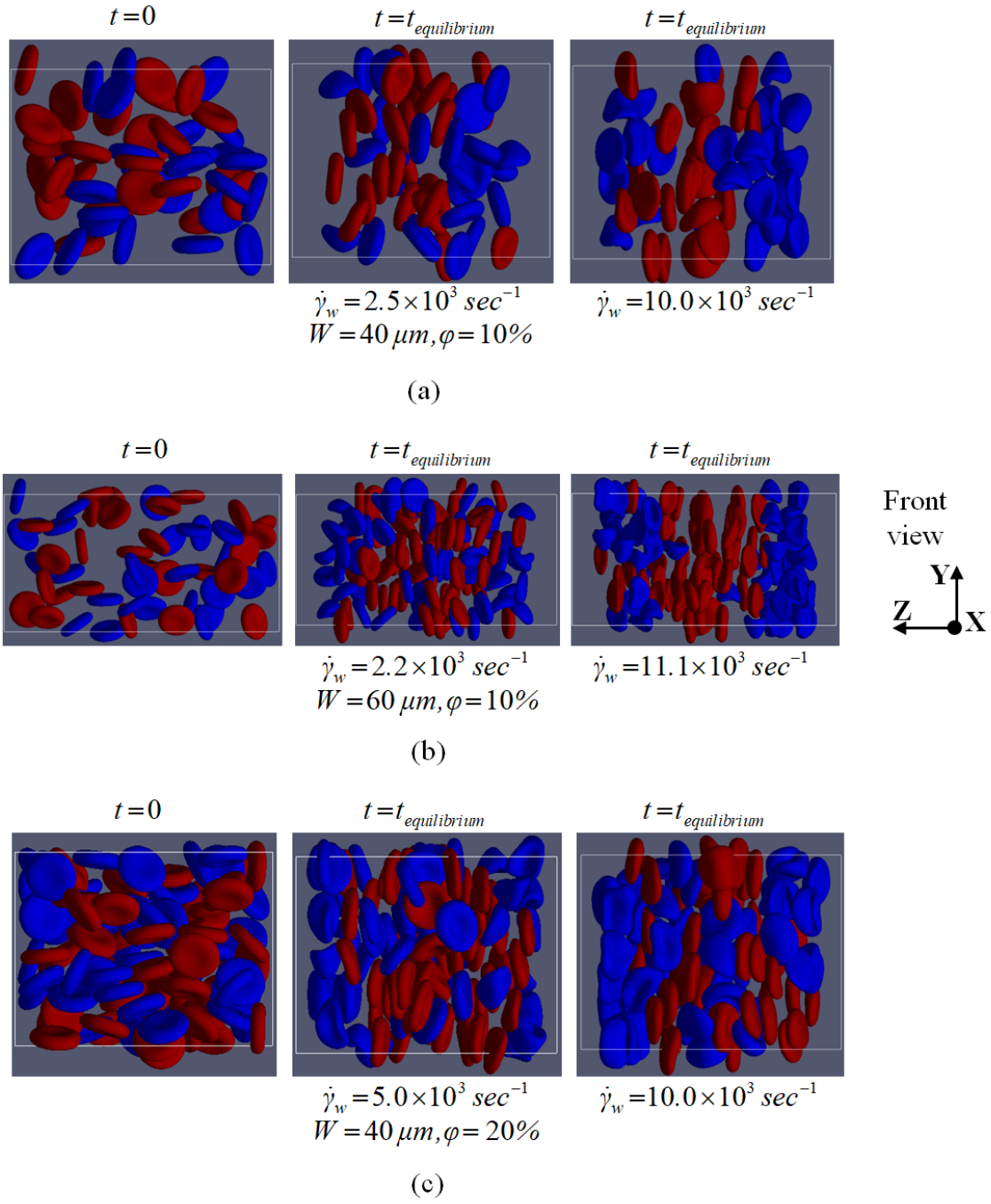

Figure 2.17: Snapshots of front view of flow comparing margination under different shear rate. Figure (a) for $W = 40\mu m, \phi = 10\%$, figure (b) for $W = 60\mu m, \phi = 10\%$ and, figure (c) for $W = 40\mu m, \phi = 20\%$. For all the three cases, left most images are for initial time step, and the rest are for at some time step after reaching equilibrium. Red cells are normal RBCs and the blue ones are sickle.

Effect of Volume Fraction

To study the effect of cell volume fraction (ϕ) on the margination, average nondimensional lateral cellular displacement, $\frac{\overline{D}(t)}{W/2}$, and spacing between average trajectories of sickle and normal cells, $\frac{\overline{D}_{sickle}(t) - \overline{D}_{normal}(t)}{W/2}$, are plotted against averaged distance crossed by cells in flow direction ($\overline{x}$) for different values of ϕ for a particular cross-sectional size and Re_c or $\dot{\gamma}_w$ in figure 2.18.

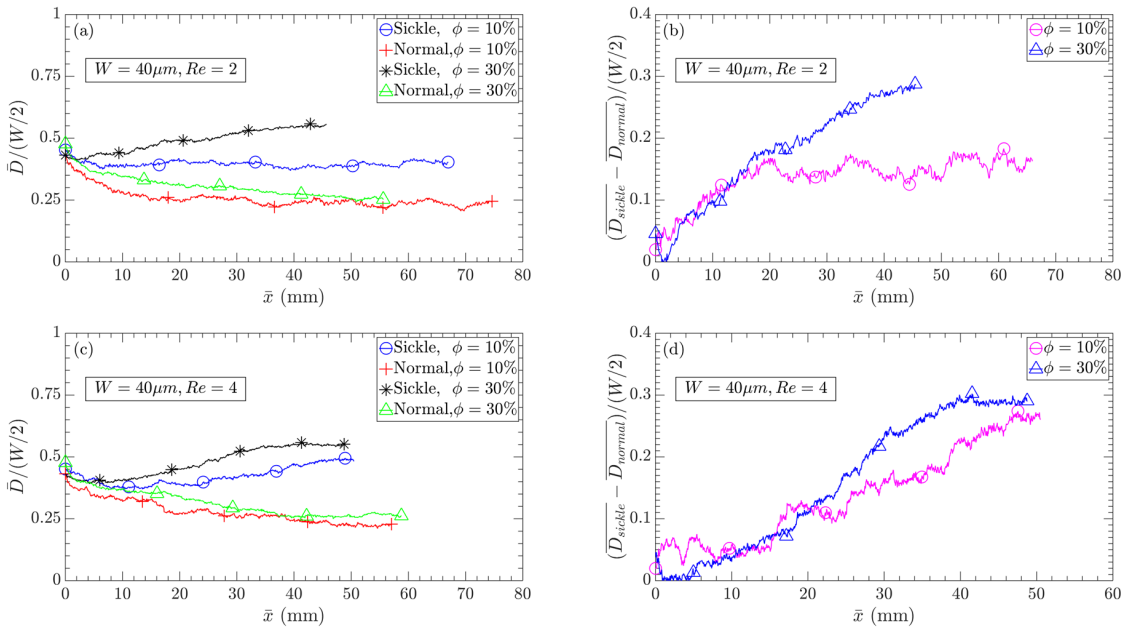

Figure 2.18: Effect of volume fraction on cell margination. Figure (a) and (c) show average normalized lateral displacement of RBCs. Figure (b) and (d) show distance between average trajectories of sickle and normal RBCs.

From figure 2.18 (a) and (b) which are for $Re_c = 2$, it can be observed that the separation of two cell types is enhanced with increasing ϕ and this effect of separation enhancement can also be observed from the snapshots of cell distribution shown in figure 2.19 (a) and (b). To investigate, whether or not, this phenomenon is independent Re_c and hence shear rate ($\dot{\gamma}_w$), the same quantities are plotted for the same channel size but for $Re_c = 4$ in figure 2.18 (c) and (d). ϕ induced enhancement of cell separation was still present for the higher Re_c which can also be observed from the snapshots of figure 2.19 (c) and (d). This

observation leads to the conclusion that, ϕ is an independent parameter that can influence the separation of cell types.

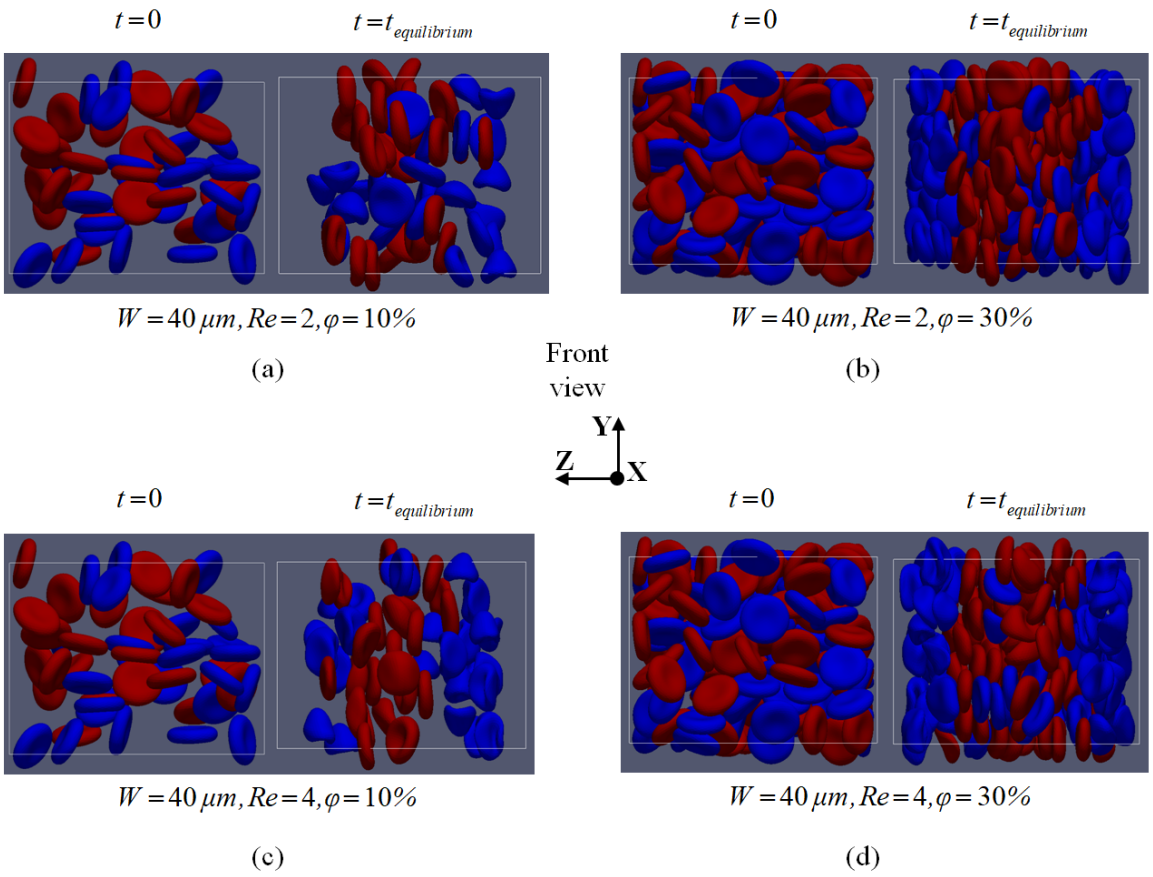

Figure 2.19: Snapshots of front view of flow comparing margination for different volume fraction cases. Figure (a) and (b) compare margination between $\phi = 10\%$ and $\phi = 30\%$ cases for $W = 40\mu m$, $Re_c = 2$. Figure (c) and (d) compare margination between $\phi = 10\%$ and $\phi = 30\%$ cases for $W = 40\mu m$, $Re_c = 4$. For all the four sub-figures, left image is for initial time step, and the right for at some time step after reaching equilibrium. Red cells are normal RBCs and the blue ones are sickle.

Combined Effect of Shear Rate and Volume Fraction

As mentioned earlier, one of the main objectives of this work is to find out flow conditions, that will optimize the separation of cells with different internal viscosity (and hence deformability) in a straight channel microfluidic device. To explore this, it is important to investigate the combined effect of flow parameters, such as shear rate ($\dot{\gamma}_w$) of flow and volume fraction (ϕ). Figure 2.20 shows the averaged cell trajectories (figure 2.20 a) and

the distance between the average cell trajectories of sickle and normal cells (figure 2.20 b). From both these plots, it is clear that an enhanced separation between the sickle and normal RBCs is obtained, when a straight channel microfluidic device is operated under an optimally high Re_c and ϕ.

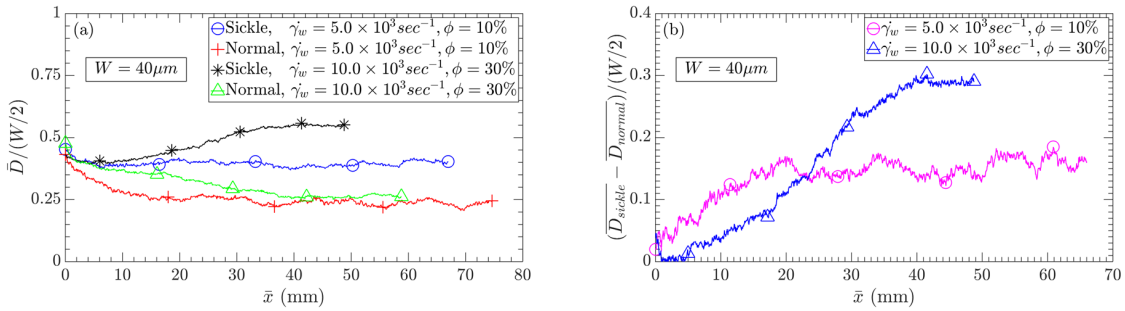

Figure 2.20: Combined effect of volume fraction and shear rate on cell margination. Figure (a) shows average normalized lateral displacement of RBCs. Figure (b) shows distance between average trajectories of sickle and normal RBCs.

2.5 Experimental Validation

A simple straight channel microfluidic device was designed and fabricated using insights obtained from the numerical simulations and some preliminary experiments were conducted to verify the margination phenomenon observed in the simulations. A schematic of the straight channel microfluidic device for cell sample enrichment is shown in figure 2.21. $10\%\,(^{V}/_{V})$ RBC suspension in PBS was flown through the device with a syringe pump, and samples were collected at the two outlets. Flowrate Q was set to $22.2135^{\mu L}/_{min}$ which corresponds to $Re_c = 5$. The inlet sample is a 1:1 mixture of normal RBC and artificially stiffened RBC with glutaraldehyde. Protocol mentioned in [106] was used to stiffen RBCs which made RBCs about two times stiffer than the normal ones[106]. A quantity called *Enrichment Ratio* ER is used as a measure of the enrichment efficiency which is defined as following

$$ER_{stiff} = \frac{\left(^{\%stiff}/_{\%normal}\right)_{outlet}}{\left(^{\%stiff}/_{\%normal}\right)_{inlet}} \tag{2.32}$$

It is basically the ratio of the amount of stiff to normal RBC at outlet normalized by that at the inlet. So, $ER_{stiff} > 1$ indicates presence of enrichment and stiff $ER_{stiff} < 1$ means there is no enrichment of stiff cells. Experimentally, the ratio of stiff to normal RBC amount for inlet and each of the outlets are measured using flow cytometer. For the device shown in figure 2.21, outlet2 is the port expected to have more of the stiffer RBC compared to port 1.

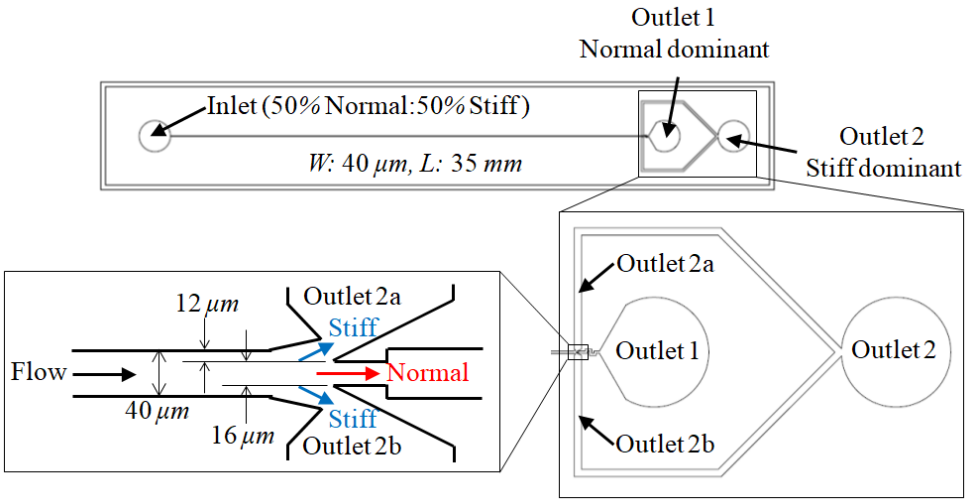

Figure 2.21: Enrichment device schematic

2.5.1 Experimental Validation Results

After conducting 12 runs of the experiment mentioned above, the average ER_{stiff} value obtained for outlet1 and outlet2 were $ER_{stiff_{outlet2}} = 1.569 \pm 0.054$ and $ER_{stiff_{outlet1}} = 0.621 \pm 0.026$ respectively. These values of ER_{stiff} indicate that, outlet2 is stiff RBC dominant and outlet1 is normal RBC dominant, thereby confirming the presence of enrichment of a particular cell type.

Next simulation was conducted for $40\mu m \times 40\mu m \times 30\mu m, \phi = 10\%, Re_c = 5$ case, where the internal viscosity of RBCs with lower deformability was set two times higher than that of the normal RBCs to match the experimental condition. For the sake of simplicity these lower deformability cells are called *stiff* cells here. Figure 2.22 shows snapshots

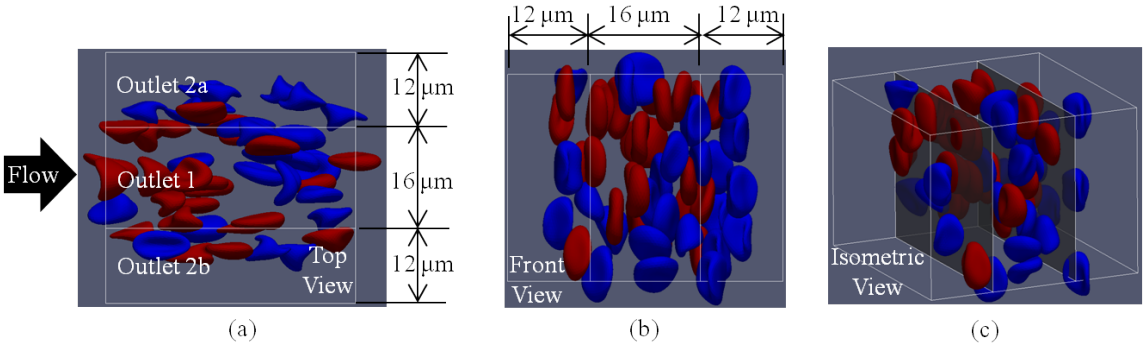

Figure 2.22: Snapshots of cell distribution after equilibrium has been reached

of the top (a), front (b) and isometric (c) view of the channel after equilibrium has been reached. The cross section of the channel is partitioned into three segments whose position matches exactly with the location of the outlet channels shown in 2.21.

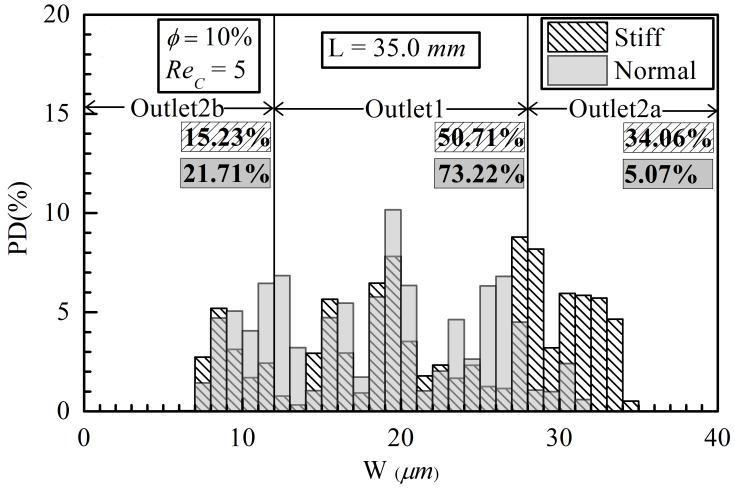

Figure 2.23: Cell population distribution, PD (%) across the width of channel at a particular lengthwise location. The width is divided into three segments (outlet 1, outlet 2a and outlet 2b) by two partitions, one located at $12\mu m$ and the other located at $28\mu m$. In each segment, the numbers represent the percentage of cell population of each cell type in that particular segment.

In figure 2.22 (a) the segments are marked with the same outlet channel names they correspond to of the channel shown in 2.21. Population distribution (PD) of both normal and stiff RBCs as a percentage of the total population of each type across the width of the channel is calculated and plotted in figure 2.23. From this $ER_{stiff_{outlet2}}$ is calculated to

be 1.84. So, the margination effect and hence the enrichment observed in simulation was also observed in the experiment. Average value of $ER_{stiff_{outlet2}}$ obtained from experiments was very close to that obtained from simulation. Simulation overpredicted $ER_{stiff_{outlet2}}$ slightly. This is mainly occurring due to the variation of stiffness property in real RBCs, minor variation in channel dimension due to fabricaiton error and error due to disturbance from surroundings during the flow experiment.

2.6 Conclusion

In this study, transverse margination behavior of deformable RBCs based on their internal viscosity has been studied for wide range of cell volume fraction. It is observed that both in the absence and presence of inter cellular interaction, RBCs with higher internal viscosity behave like stiffer cells compared to the normal RBCs. For single cell cases, RBCs of different cytoplasmic viscosity migrate transversely to their equilibrium position, the normal ones staying closer to the center of the channel while the ones with higher internal viscosity staying closer to the wall. Also the rate of margination is enhanced and the cells reach to their equilibrium locations faster with the increase in flow Reynolds number. For the dense suspension cases, collision between cells plays a significant role in margination in addition to the internal viscosity of the cells. The normal RBCs gather in a region close to the channel center within a very short time scale and through interaction with the normal cells, the cells with higher internal viscosity diffuse to outer region closer to the wall following the RESID mechanism [64]. Segregation between the two cell types is observed to get stronger with higher flow Reynolds number and higher cell volume fraction. Deformable RBCs with different internal viscosities also seem to follow the margination scaling law proposed by Mehrabadi *et al.* [64]. Preliminary experiments were conducted and margination pattern observed in simulations was experimentally verified. Results from this study will aid in designing of microfluidic devices for blood cell sample enrichment for different diseases.

CHAPTER 3
STRAIGHT CHANNEL MICROFLUIDIC DEVICE FOR STIFFNESS DEPENDENT CELL ENRICHMENT: CHARACTERIZATION OF PERFORMANCE AND ITS IMPROVEMENT

3.1 Introduction

Separation and enrichment of disease affected cellular components of blood have already been established as the first step of disease diagnostic. Analyses on these enriched samples are very likely to lead to an accurate assessment of disease progression for individual patients and newer treatment or enhanced treatment strategies. Currently cellular expression of bio-molecules and morphogy of cells are most widely used as bio-markers for cell separation and identification of critical diseases like cancer, spherocytosis, malaria, sickle cell disease, etc. Based on these biomarkers, the three most widely used diseased cell enrichment tools currently used in health care industry are density gradient methods / centrifuge, magnetically actuated cell sorter (MACS) and flow cytometer. Each of these tools requires trained professionals to operate, is expensive and time consuming. In research community microfluidics based cell sorting has caught a lot of attention in last couple of years. Researchers have explored use of magnetic fields [107–109], electric fields [110–113], optical forces [114–116] and acoustic fields [117–119] on microfluidic chips quite extensively. These methods are also known as *active* separation methods, where an external force field is employed to achieve separation. As can be guessed, these active methods add to the complexity of device fabrication and operation and are also expensive. To complement these active methods, researchers have sought for different biophysical properties based on which label free and *passive* separation methods (requiring no external forces) of cell separation can be developed. Size [120–123], shape [124, 125], mass [126] and adhesiveness

[127] have been used as biophysical markers for separating cells by numerous researchers, and the ones cited here are just few significant ones. However, overlap in values of these properties between diseased and normal blood cells, especially size and morphology, poses a significant challenge for them to be used as the basis for separation. Morphology in particular though useful for separating blood cells of different kinds, but is quite ineffective when it comes to the task of separating diseased cells from the normal ones having same shape. Cell stiffness/deformability is a property that gets affected by a lot of the diseases quite strongly and the band of overlap of values between diseased and normal cells is quite narrow. That is why stiffness has proven to be quite a suitable biophysical marker, based on which efficient separation between diseased and normal blood cells can be achieved, especially when the cell type is same [46, 128–130]. Significant previous works on stiffness dependent separation of cells using straight channel microfluidic devices can be classified into three broad categories : (i) inertial microfluidics based [46, 55, 128], (ii) viscoelastic medium based [35, 129, 131] and (iii) special channel feature (e.g. ridged channel) based [130, 132, 133].

As mentioned in chapter 2, particle migration through inertial flow in circular pipe was first reported by Segré and Silberberg [43] and since then it has been numerically predicted and experimentally observed by many other researchers. The mechanism of inertial lift can be summarized according to a recent explanation provided by Matas *et al.* [45] and Zhou *et al.* [98] as follows: neutrally buoyant particles in a microchannel with no other external force present, experience two forces, wall-repulsion force F_W (figure 2.1 (c)) that pushes the particles away from the wall and the shear gradient force F_S (figure 2.1 (b)) that pushes the particles from low shear to higher shear region, i.e. in the direction towards the wall. The magnitude of F_W decreases further away from the wall. The inertial lift force (F_L) is a combination of F_S and F_W and the equilibrium position of particles are determined by the balancing of these two forces. Although it was previously thought that inertial lift force is only important for inertial flows and can be neglected for low Reynolds

number flows occurring in microfluidic channels, experimental studies done by Di Carlo *et al.* [55, 134] showed that for confined flows as in microchannels, inertial lift force is still of importance and play a crucial role in particle margination. They showed that for flows in rectangular channel with height H, inertial lift on a solid particle with diameter d will scale as $F_L \propto \frac{\rho U^2 d^3}{H}$ near channel center-line and $F_L \propto \frac{\rho U^2 d^6}{H^4}$ near the channel wall, where ρ is density of suspending media and U is aveage particle velocity. As explained in chapter 2, particle deformability induces an additional lift force F_D near the channel wall [135–137] originating from flow disturbance by a deformed object [32, 136]. Abkarian *et al.* [42, 138] have expressed this force as

$$F_D = \left(\frac{\mu R^3 \dot{\gamma}_w}{\delta}\right) \vec{n} f(V_R) \tag{3.1}$$

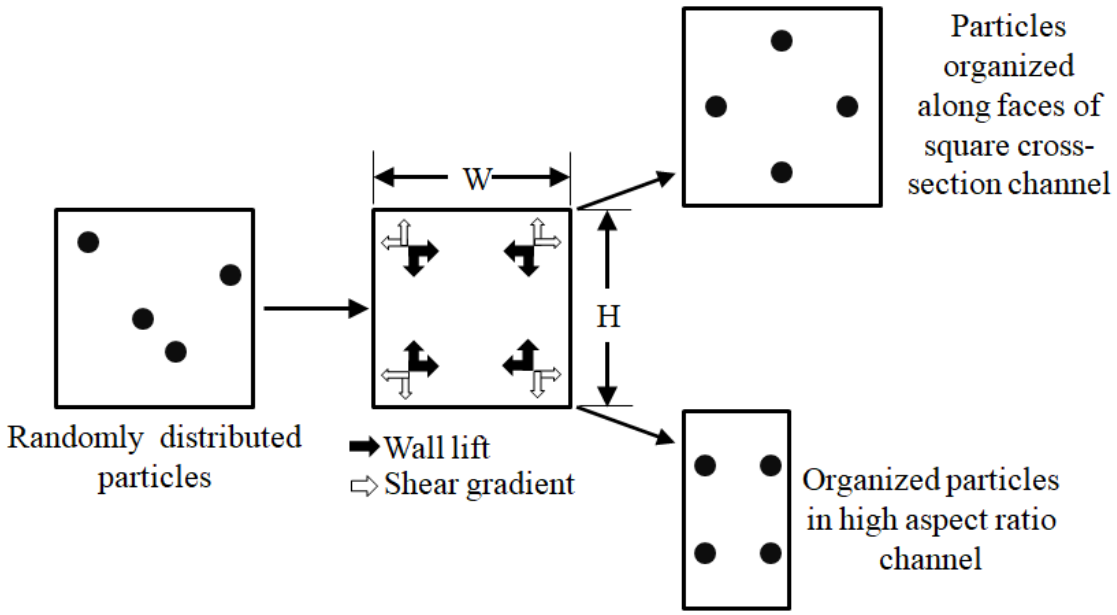

Figure 3.1: Inertial migration of particles in rectangular channel

Here V_R is the reduced volume defined as $V_R = \frac{V_C}{{}^4/_{3\pi}\left(\sqrt{{}^S/_{4\pi}}\right)^3}$, V_C is particle volume, S is particle surface area, R is the effective particle radius defined as $\left(\frac{3V_C}{4\pi}\right)^{1/3}$ for non-spherical deformable particle such as RBCs, δ is the distance between particle and channel

wall, μ is medium dynamic viscosity, $\dot{\gamma}_w$ is wall/characteristics shear rate and $\vec{n}$ is the normal wall vector. $f(V_R)$ needs to determined experimentally. For deformable particle that is quite far away from the wall ($\delta \gg R$), wall lift force scales as $F_D \approx \frac{R^4}{\delta^2}$ [139–141] instead of $F_D \approx \frac{R^3}{\delta}$.

Figure 3.1 shows margination of randomly distributed deformable particles in a microchannel having rectangular cross section under inertial lift. As can be seen, for channels having a square cross secsion (height (H) and width(W) same) the particles marginate along the middle of the faces, whereas for non-unity aspect ratio channels $\left(\frac{H}{W} \neq 1\right)$ the particles marginate along the two opposing faces that create the largest shear gradient. Using the above explained mechanism, Hou *et al.* did deformability based enrichment of malaria infected RBCs from a mixture of normal and malaria infected RBCs with the help of a low aspect ratio straight channel microfluidic device. They found out that, for the cases they ran, enrichment efficiency improved remarkably with increasing volume fraction of cells in the cell solution and flow rate had no remarkable impact on the enrichment efficiency. Using the same principle of inertial focusing, Hur *et al.* [46] did enrichment of different types of cancer cells from a very dilute blood sample spiked with cancer cells. They used very dilute cell solution to make sure no cell-cell interaction was present. This is to avoid cell defocusing and mixing due to cell-cell interaction in the straight portion and diverging section of outlet of their device. They also studied the effect of flow Reynolds number (Re_C) on enrichment efficiency, and found out that for the experiments they ran, there is an optimum RE_C for which the efficiency is maximum, and running the device below or above this Re_C will yield a lower efficiency. They defined the measure of cell enrichment efficiency as *Enrichment Ratio*(ER). For enriching stiff cell out of a mixture of normal and stiff cells, it can be defined as

$$ER_{stiff} = \frac{\left(\%stiff/\%normal\right)_{outlet}}{\left(\%stiff/\%normal\right)_{inlet}} \tag{3.2}$$

The experimental use of viscoelastic medium in solid particle focusing was first re-

ported by Yang *et al.* [142], which was mainly based on the theoretical work of Ho *et al.* [131]. For particle focusing in viscoelastic media the parameter *Elasticity* (El) is important, which determines the relative importance of medium elasticity to flow inertia, and is defined as

$$El = \frac{Wi}{Re_C} = \frac{\lambda\mu(W+H)}{\rho W^2 H} \tag{3.3}$$

Here Wi is Weissenberg number which is defined as $Wi = \lambda\dot{\gamma}_w$, where λ is medium relaxation time. For rectangular channel Wi is defined as $Wi = \dfrac{2\lambda Q}{HW^2}$ and channel Reynolds number Re_C is defined as $Re_C = \dfrac{\rho U h}{\mu}$, where h is characteristics length defined as $h = \dfrac{2HW}{H+W}$ and Q is the flow rate in the channel. The limiting case of $El \sim 0$ represents flow with only inertial effect and $El \gg 1$ represents flow cases with only elasticity effect. In their work, Yang *et al.* surmised that particle focusing can only be obtained for moderate values of El, i.e. when the flows are influenced both by inertia and elasticity ($El \sim \mathcal{O}(1)$). They observed that particles eventually marginated to five equilibrium locations, four at four corners of the channel, and one around the central core of the channel as shown in figure 3.2.

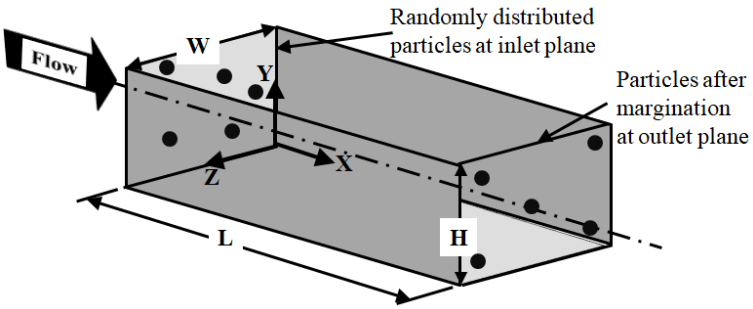

Figure 3.2: Particle migration in viscoelastic medium

Ho *et al.* [131], in their theoretical work showed that particle migration in viscoelastic medium occurs due to mainly first normal stress difference defined as $N_1 = \sigma_{xx} - \sigma_{yy}$. The second normal stress difference $N_2 = \sigma_{yy} - \sigma_{yy}$ is neglected here, as $N_1 \gg N_2$ for

viscoelastic medium with constant shear viscosity [142, 143]. Here, σ_{xx}, σ_{yy} and σzz are normal stresses exerted in the direction of flow, velocity gradient and vorticity directions. The force exerted due to medium elasticity on the particles can be expressed as follows (from [129, 144, 145]):

$$F_e = AR^3 \nabla N_1 \tag{3.4}$$

where, A is an empirical constant and R is the particle effective radius. Balancing F_e with the drag force on particle, the non-dimensional form of particle lateral migration velocity has been derived as [129]:

$$\frac{\overrightarrow{V}/U_{avg}}{\left(R/H\right)^2 \left(4A/6\pi\right)} = \hat{\nabla}\hat{N}_1 = 2Wi\hat{\nabla}\hat{\dot{\gamma}}_w^2 \tag{3.5}$$

where $\overrightarrow{V}$ is particle lateral migration velocity, U_{avg} is average streamwise velocity, $\hat{N}_1$ is first normal stress difference non-dimensionalized with $\frac{2\mu U_{avg}}{H}$ and $\hat{\dot{\gamma}}_w$ is non-dimensionalized wall shear rate.

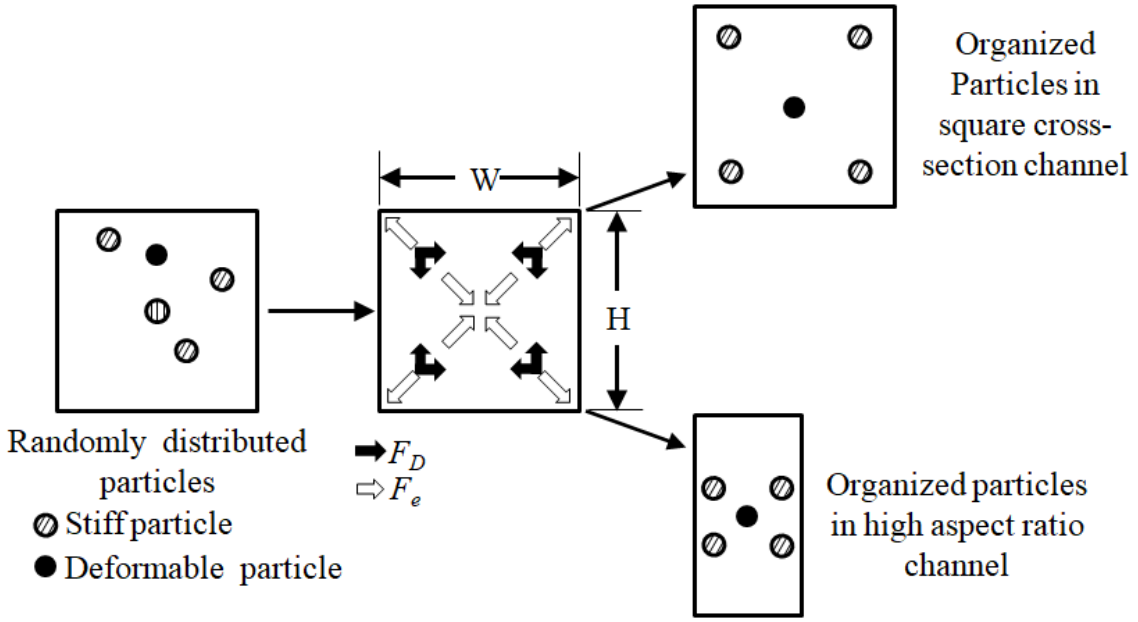

Figure 3.3: Migration of deformable and stiff particles in viscoelastic medium

For a rectangular channel, there are five locations of minimum of the quantity $\frac{\vec{V}/U_{avg}}{\left(R/H\right)^2\left(4A/6\pi\right)}$ on the channel cross-section (as shown in figure 3.2) where solid particles will migrate to in a purely viscoelastic flow condition [142]. Based on these principles, Yang *et al.* [129] conducted experimental study to enrich stiffer particles and cells from a mixture of cells and particles of varying deformability. Deformable particles will experience two forces, the wall lift force due to deformability (F_D) and the elastic force (F_e) as shown in figure 3.3. Randomly distributed deformable particles will settle down in cross-sectional locations where F_D and F_e balances each other out. Out of the five cross-sectional location, the ones near corner will be rich in stiff/less deformable particles and the one around the central core will contain more deformable cells. Yang *et al.* [129] in their work showed significant enrichment of stiff polystyrene (PS) particles from mixture of PS particles and normal RBCs and, artificially stiffened RBCs from mixture of artificially stiffened RBCs and normal RBCs. For each of the cases they ran, they found out that there is an optimum flow rate which will yield the maximum ER and above and below this value of flow rate, ER will be lower.

Use of special geometrical features, such as diagonal ridges [130, 133] in channels, has brought noticeable success in efforts to separate cells of similar size and shape, but different deformability. Wang *et al.* [130, 133] separated certain types of cancer cells from mixtures of white blood cells (WBC) and cancer cells with enrichment ratio as high as 6.3 fold. Their work is based on a previous theoretical study of Mao *et al.* [132] on deformable particle margination in microfluidic channels with top wall decorated with ridges spanning in diagonal direction. Study of Mao *et al.* [132] showed that when a deformable particle tries to squeeze itself through the spacing between diagonally placed ridges and channel bottom wall, it experiences an elastic force acting perpendicular to the diagonal ridges. This force has a component that displaces cell in a direction normal to the flow direction. The stiffer cells get displaced more by that component compared to the more deformable ones, and hence stiff and normal cells will have two different trajectories as they move

along the channel and can eventually by collected by two different outlets.

The methods mentioned so far have multiple issues low throughput because of the necessity to use very dilute sample [46, 129, 130, 133], low ER because of mixing at the expanded section near the outlet [46, 128], issues with channel clogging [130, 133], inability to be applied to non-spherical cells like RBCs [130, 133] and special treatment / washing after the cells have gone through the separation process [129]. The current work focuses on using inertial migration and cell volume fraction to separate RBCs based on their stiffness from a mixture of normal and artificially stiffened RBCs with a straight channel microfluidic device. There are mainly two major portions of this work. In the first portion, a simple straight channel is designed and fabricated based on the results obtained from simulations (chapter 2), experiments were run to achieve cell enrichment and the straight channel device performance was characterized for varying flow rate and cell volume fraction. In the second portion of the work, an improved version of the straight channel device was designed and fabricated and experiments were run study performance improvement.

3.2 Methods

The whole experimental process can be divided in four major steps : (i) preparing the separation device, (ii) cell sample preparation, (iii) flow conducting flow experiment and (iv) analyze separated samples. A flow chart of the process can be seen in figure 3.4.

3.2.1 Microchannel Design and Fabrication

As mentioned in section 3.1, there were two versions of straight channel devices that were tested experimentally for their performance to enrich RBCs based on stiffness. The first one is a simple straight channel device and and its schematic can be seen in figure 3.5. The straight channel portion, which is also the portion where the cell margination takes place, has a length, $L = 35mm$, width $W = 40\mu m$ and height $H \approx 100\mu m$. So the channel aspect ratio is $\frac{H}{W} \approx 2.5$. These parameters were chosen baesd on the results from

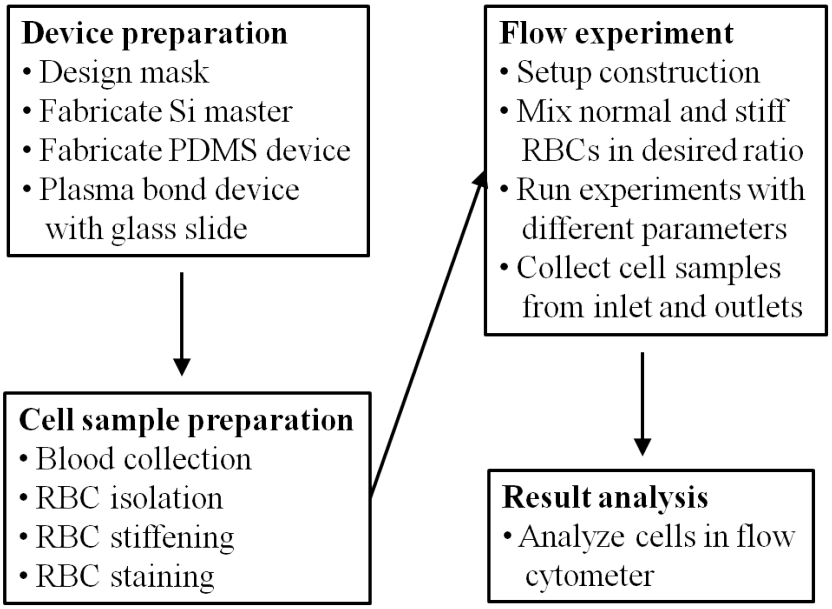

Figure 3.4: Flow chart of experiment

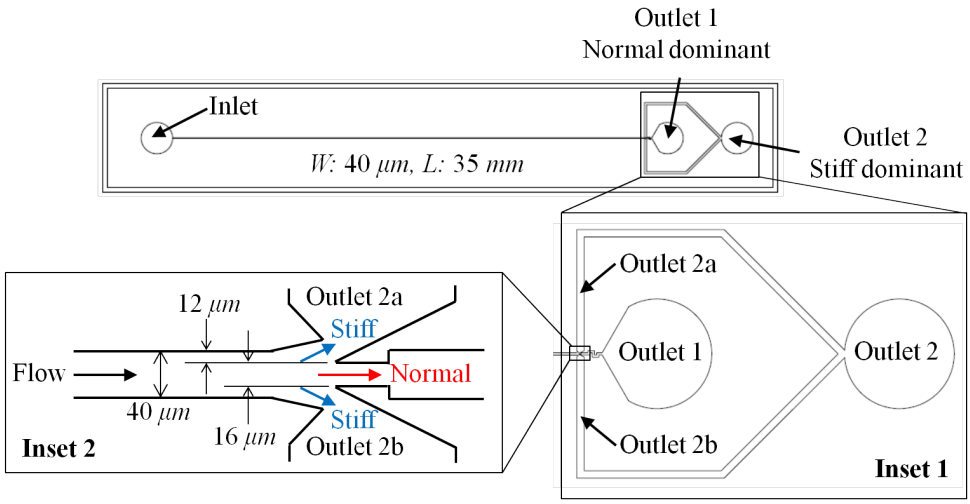

Figure 3.5: Schematic of simple straight channel device

numerical simulations as reported in chapter 2. At the end of the channel, there are three branches as can be seen from inset 1 and inset 2 of figure 3.5, where branches 2a and 2b will eventually merge to form a common outlet 2. As the cell mixture travel from inlet to the branching, the stiffer cells will marginate towards to wall, and the normal ones gather in the central core, as was observed in chapter 2. Outlet 2 is expected to be stiff enriched and outlet 1 to be normal enriched. The widths of these outlets were designed to optimize

the collection of samples enriched with the desired cell type (stiff or normal) based on the cell distribution pattern obtained from simulations as shown in figure 2.22.

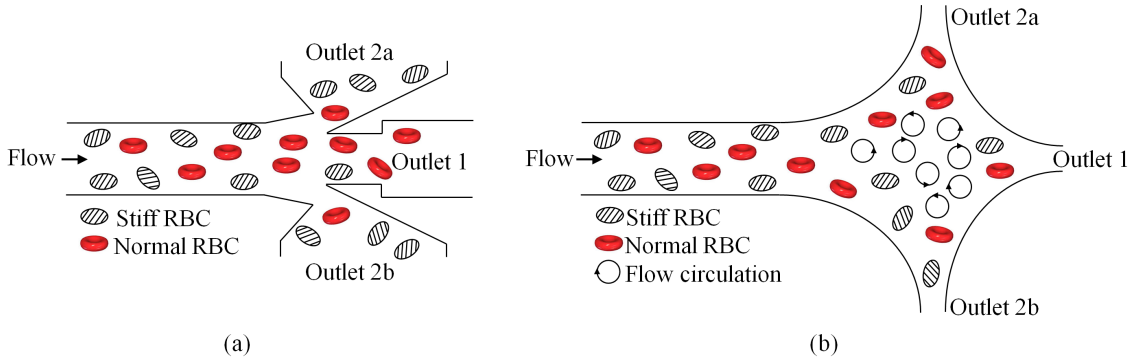

Figure 3.6: Comparison of cell streaming near outlet between devices with and without a diverging section. (a) Channel without diverging section, (b) Channel with diverging section.

As can be seen from inset 2 of figure 3.5, this design got rid of the expanded / diverging section at the end of the straight channel, as was done in earlier works [46, 128]. This is to avoid re-mixing of normal and stiff cells. As all the experiments were run in the laminar flow region, in the straight portion of the device the cells will follow the streamlines after reaching equilibrium. However, when they reach such a diverging section as done in [46, 128], there will be a sudden and big drop of flow velocity and flow circulation will be created, which will cause the cells to stagnate. Eventually the whole pattern of cell type segregation (stiff cells near the wall, normal ones around the channel center) will be destroyed because of remixing of the cells due to flow stagnation and circulation at the diverging section and the samples collected at outlets are more likely to have undesired cell composition. Also, channels without a diverging section, are shorter in size. Getting rid of the divergent section, also made it possible to design an improved multistep version of the channel, which will be described shortly. Merging of branching 2a and 2b reduced the total number of outlets from three to two. This led to reduction of the likelihood of having backflow problem due to uneven pressure drop at outlets and thereby reducing the undesired bias in cell type composition at the outlets.

Schematic of the second device, which is an improved version of the first one can be seen in figure 3.7. This can be viewed as a multistep version of the simple straight channel device. A mixture of stiff and normal RBCs coming from the inlet (region b of figure 3.7(a) and figure 3.7(b)) gets divided into three branches (region c of figure 3.7(a) and figure 3.7(c)). The two side branches are expected to be stiff RBC dominant and the middle one is expected to be normal RBC dominant. Cell mixtures in all these branches will again flow through straight channel portions and another level of enrichment will take place when they further get separated into stiff and normal dominant outlets. Here, outlet 1 is expected to be normal RBC dominant and outlet 4 and 6 are expected to be stiff RBC dominant. As this is a multistep enrichment process, the expectation is outlet 1 of multistep device will have higher ER_{normal} than outlet 1 of the first device and, outlet 4 and 6 of multistep device will have higher ER_{stiff} compared to outlet 2 of the first device.

For fabricating the device, soft lithography technique introduced by Qin *et al.*[146] was used. First a mask containing the device schematics of figure 3.5 and 3.5 was designed using AutoCAD and was printed on chrome glass. For fabricating the master on 4-inch silocon wafer, first the wafer was spin-coated with a negative photoresist (SU8-2100, Microchem). After following the proper baking steps, the spin-coated wafer was exposed to light in a mask aligner (TSA-MA6) with light passing through the designed mask. The exposed wafer was then baked and washed with developer to have the photoresist master. PDMS prepolymer mixed at a $10:1$ $(^{W}/_{W})$ ratio with curing agent was poured onto the silicon master and cured at 60°C for 6 hours. The cured PDMS device was then cut carefully off the silicon master. Holes were punched using 1.5 mm hole puncher. This device was then plasma bonded with glass slide to have a sealed device ready for running flow experiment.

3.2.2 Cell Sample Preparation

Fresh human blood was collected from healthy consenting donors in 3 mL BD Vacutainer

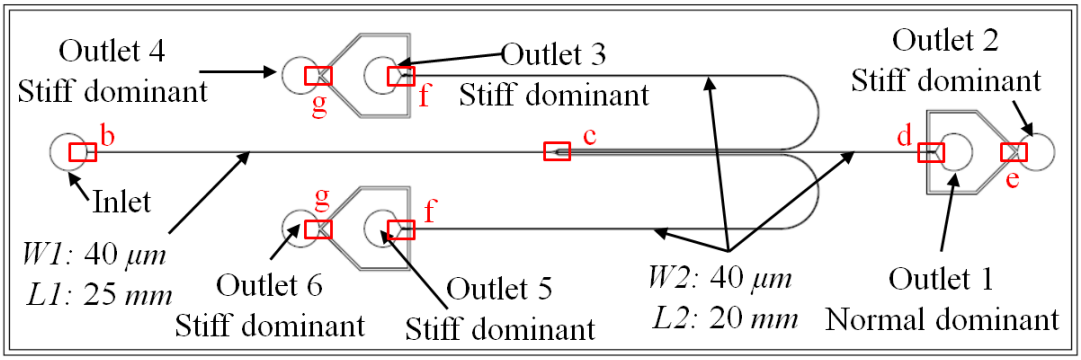

(a)

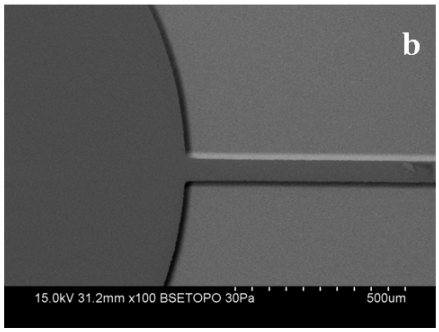

(b)

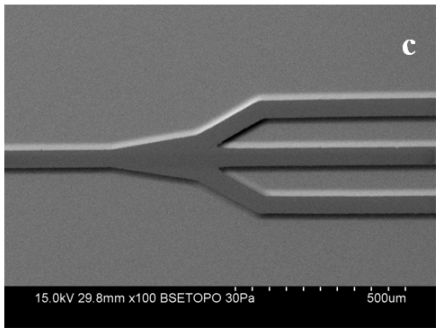

(c)

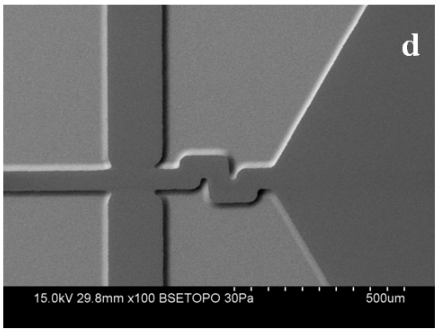

(d)

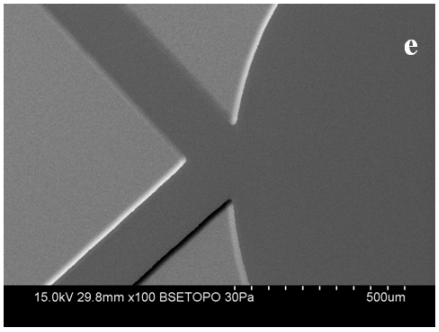

(e)

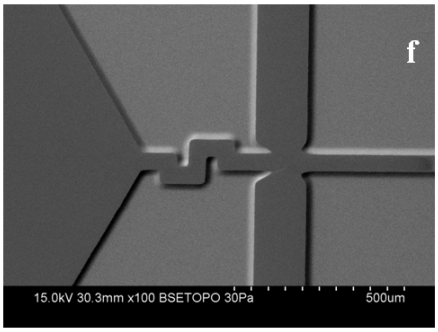

(f)

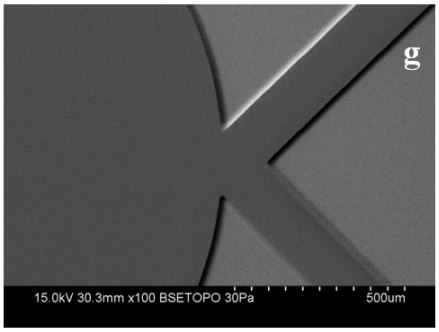

(g)

Figure 3.7: Multistep straight channel separation device. (a) Whole channel schematic. (b)-(d) SEM images of locations marked b to g in schematic of the whole channel.

tube with Sodium Citrate as anti-coagulant. This whole blood sample was first spun at 150 G for 15 minutes. Plasma and buffy coat was aspirated out from the top of the tube to make sure all that are left in the tube bottom were RBCs. These RBCs were washed with 1X PBS (pH 7.4, ThermoFischer Scientific) two times by centrifuging at 300 G for 7 minutes each time.

An appropriate portion of the washed RBC was separated for stiffening process with glutaraldehyde. The source solution of glutaraldehyde (3% in Aqueous, Poly Scientific R&D Corp.) was diluted with PBS to form stock solutions of 0.10%. RBC samples were combined with the stock solution of glutaraldehyde in 1:1 $(^{V}/_{V})$ ratio to expose the cells to glutaraldehyde concentrations of 0.05%. The cells were incubated in glutaraldehyde for 10 minutes at room temperature. For quenching the cross-linking reaction, 50 mL of PBS was added and the solution was immediately washed by centrifuging at 150G for 10 minutes. After aspirating out the supenatant from the tube, the stiffened RBCs were washed with 10 mL of PBS by centrifugation two more times to make sure no glutaraldehyde was left and the cross-linking reaction was quenched completely. The protocol followed here is very similar to what was done by Sosa *et al.* [106], who reported the deformability of stiffened RBCs to be about 50% of that of normal ones when 0.05% glutaraldehyde is used. So, for all the experiments performed in this work, the glutaraldehyde stiffened RBCs are approximately twice as stiffer as the normal ones.

The stiffened RBCs were then aliquoted in portions of 25 μL to be stained with antibody conjugated with fluorophore. The staining buffer was made by mixing FBS with PBS in 1:10 $(^{V}/_{V})$ ratio. Aliquoted RBCs were first incubated at room temperature for 1 hour with the 500 μL staining buffer for the unspecific binding sites. The RBCs were then spun down at 300 G for 7 minutes and the supernatants were removed. Packed RBCs were re-suspended in 500 μL staining buffer and 10 μL of Ab91163, a CD235a binding antibody conjugated with Allphycocyanin (APC) from Abcam, was added as suggested by sample protocols provided by Abcam. The solution was then mixed in hula mixer for 2 hours at

room temperature. This well mixed solution was then centrifuged at 300G for 7 minutes and the supernatant was aspirated out. The packed RBCs were then re-suspended in 1 mL of PBS and stored at $4°C$ for use in flow experiment.

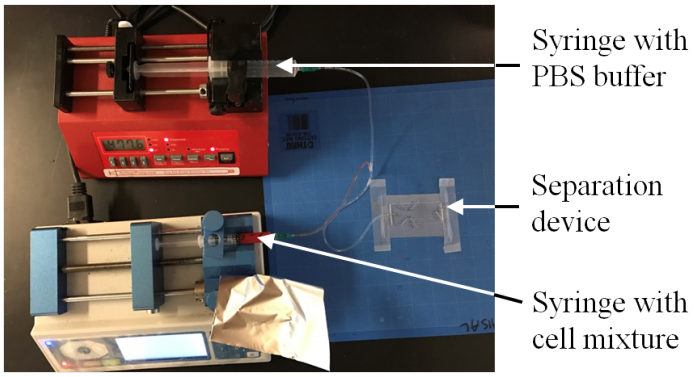

Figure 3.8: Experimental setup

3.2.3 Flow Experiment

For running the flow experiments to enrich stiff RBCs from a mixture of normal and stiff RBCs, normal and stiff RBCs were mixed in $1:1\,(^{V}/_{V})$ ratio and suspended in PBS in desired volume fraction. The devices were coated with 1% BSA (Sigma-Aldrich) in PBS for about 1 hour to reduce the possibility of any non-specific binding of RBCs in the channel that could lead to channel clogging and/or biased cell composition at the outlets. A series of experiments were run to study the effect of flow rate or Re_C and volume fraction ϕ on the efficiency of enrichment. A complete list of all the cases run for single straight channel and the multistep device can be found in table 3.1 and table 3.2 respectively.

Table 3.1: Experimental parameters for simple straight device

$\phi(\%)$ \ Re_C	5	10	20	40
5%	X	X	X	X
10%	X	X	X	X
20%	X	X	X	X

Table 3.2: Experimental parameters for multistep device

$\phi(\%)$ \ Re_C	**10**	**20**
10%	X	X
20%	X	X

An additional syringe containing PBS (figure 3.8) was used in the experimental setup. This was done to remove bubbles and debris from the channel, and wash the devices before and after running separation experiments with a combination of parameters (table 3.1 and 3.2), thereby giving the opportunity to re-use a device. Cell smaples collected from inlet and each of the outlets are analyzed in flow cytometer (BD Acuri C6) to find out the ratio between stiff (stained with Ab 91163) and normal RBCs. Efficacy of a particular cell type enrichment is described by a parameter called *Enrichment Ratio (ER)*, which is defined as

$$ER_{desired} = \frac{\left(\%desired/\%other\right)_{outlet}}{\left(\%desired/\%other\right)_{inlet}} \tag{3.6}$$

where the subscript *desired* stands for the the target cell type for enrichment, and subscript *other* stands for the other cell type in the cell mixture.

3.3 Results and Analysis

There are two major phases of the experimental work. In the first phase, enrichment experiments were conducted with simple straight channel device and the device performance was characterized against variation of flow and cell mixture parameters. In the second phase, experiments were run with multistep device to validate its better performance and study effect of flow and cell mixture parameters on enrichment efficiency.

3.3.1 Simple Straight Channel Device

Validation of Cell Type Margination

For initial experimental validation that most of the stiffer RBCs stay closer to the channel walls and the normal ones stay around the central core, solutions of glutaraldehyde stiffened RBCs and normal RBCs were flown through the simple straight channel microfluidic devices and the margination patterns near the outlet branching were recorded with a high speed camera (Vision research). Snapshots of cell margination pattern for the both the normal and stiff RBCs can be seen in figure 3.9. As can be observed, most of the normal cells coming from the straight portion of the device stay near the central core and hence at the branching of outlets they mostly follow the middle outlet, whereas the stiff cells are more spread throughout the whole channel width and hence they divert to the two side outlets at the branching.

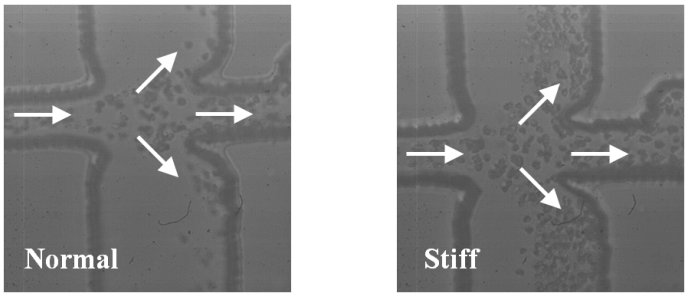

Figure 3.9: Margination pattern of cells near the outlet branching. (a) Normal RBCs, (b) Stiff RBCs. Arrows indicate flow direction.

Validation of Cell Enrichment

As can be seen from table 3.1 a series of experiments were run with different combination of Re_C and ϕ values. Samples collected from inlet and outlets were analyzed in flow cytometer. Figure 3.10 shows results of flow cytometry analyses performed on samples collected from one of the experiments for parameter combination of $\phi = 20\%$ and $Re_C = 40$.

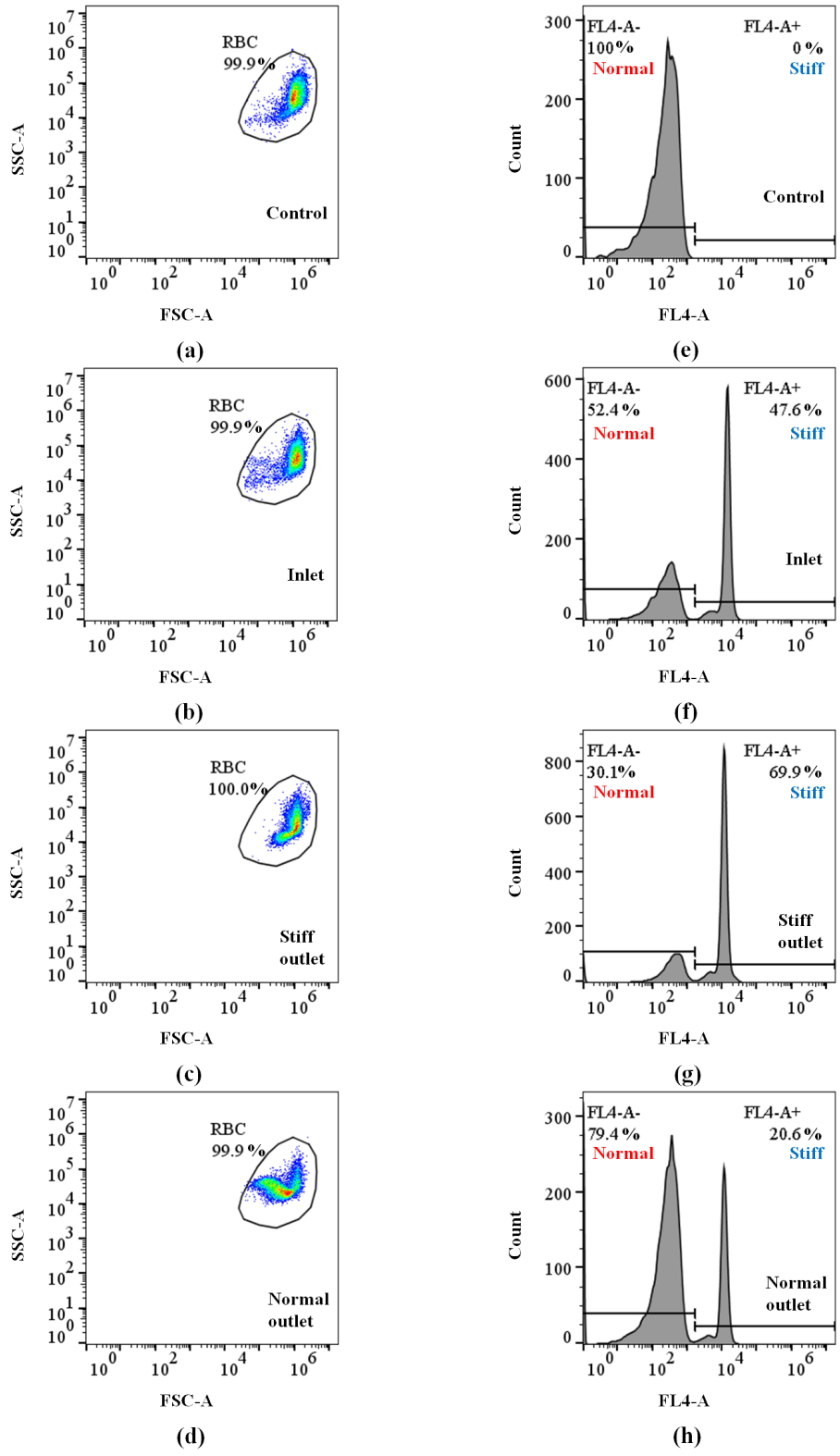

Figure 3.10: Flow cytometry analyses of cell samples collected after experiment.(a)-(d) Scatter plots. (e)-(h) Histograms for allophycocyanin (APC) signal collected at channel FL4-A. Sample identifications are provided at the bottom right corner of each plot.

As mentioned in section 3.2.2, in the RBC mixture only the stiff cells were stained with Ab 91163, which is a CD235a binding antibody conjugated with APC. So, the stiff RBCs are detected in channel FL4-A of the flow cytometer used for analysis. Figure 3.10 (f), (g) and (h) are providing the ratio of normal to stiff RBC amount in inlet, stiff cell dominant outlet and normal cell dominant outlet respectively. Using these numbers in equation 3.6, the enrichment ratio for stiff cell was calculated to be $ER_{stiff} = 2.55$ and that for normal cells was calculated to be $ER_{normal} = 3.50$. Multiple experiments were conducted with a particular combination of ϕ and Re_C to obtain average values of ER and further statistical analysis. The results presented in figure 3.10 are representative for all the experimental runs.

Stain Swap Test

To make certain that the cell margination and hence the enrichment was purely because of difference in stiffness and was independent of the antibody staining, RBC cell samples were prepared by swapping the stain, i.e. instead of glutaraldehyde stiffened RBCs, normal RBCs were stained with Ab 91163. Flow experiments were run for $\phi = 20\%$ and $Re_C = 20$ case with these cell samples. The enrichment ratios calculated for stiff and normal RBCs were $ER_{stiff} = 2.65 \pm 0.05$ and $ER_{normal} = 2.44 \pm 0.05$. These values are in the same range as those obtained when stiff RBCs are stained instead of the normal ones. This indicates that RBC margination in the microfluidics device was independent of antibody staining and purely dependent on cell stiffness. Flow cytometry anlyses results from one of the experiment runs for these cases are presented in figure 3.11.

Effect of Flow Reynolds Number

To characterize the performance of simple straight channel device enrichment for Re_c variation, experiments were run varying the flow rate (and hence Re_C) for a particular value of the cell solution volume fraction (ϕ). Multiple experiments were conducted for a particular

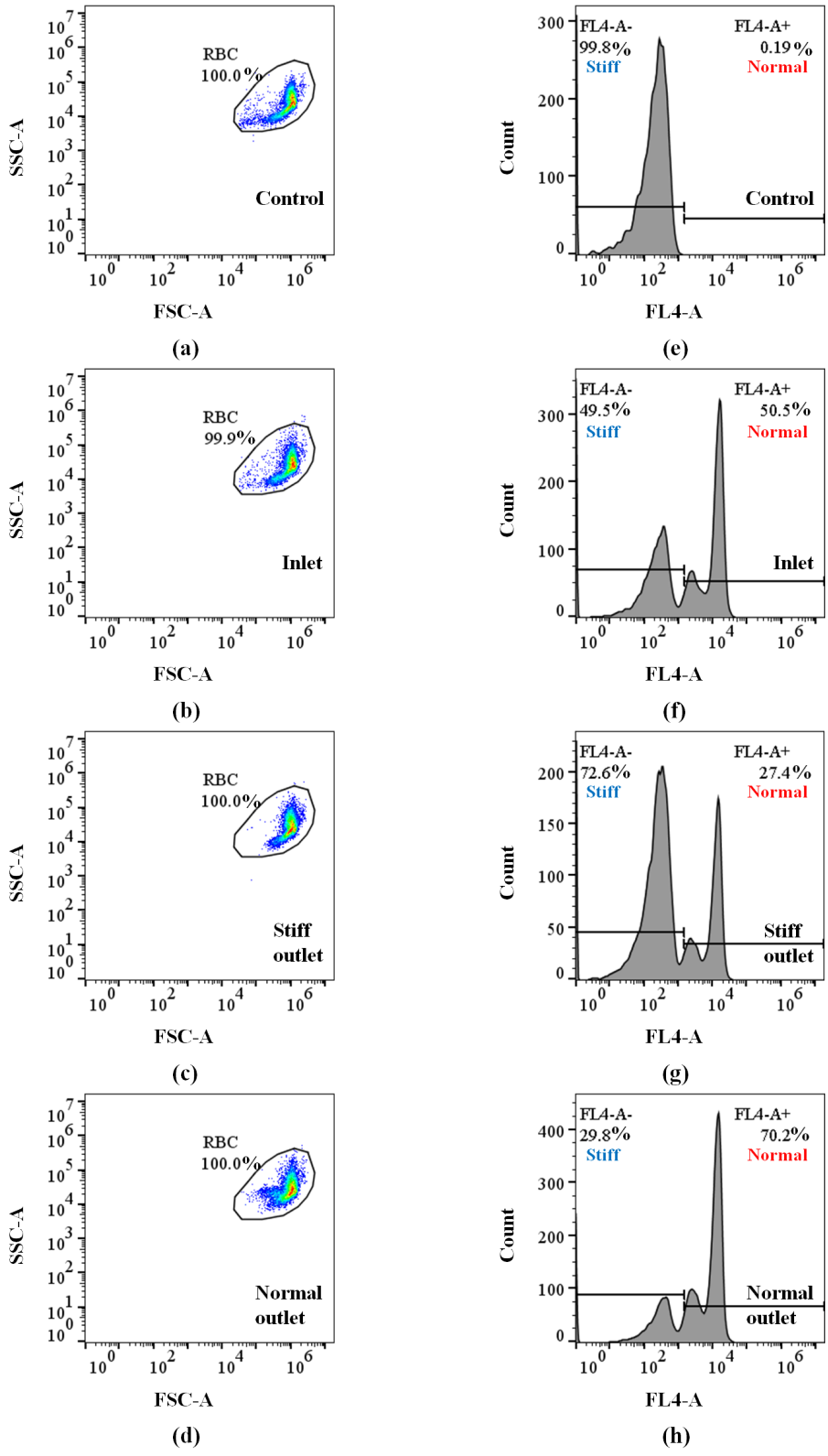

Figure 3.11: Flow cytometry analyses for stain swap test. Normal RBCs are stained with allophycocyanin (APC) and stiff RBCs are unstained. (a)-(d) Scatter plots. (e)-(h) Histograms for APC signal collected at channel FL4-A. Sample identifications are provided at the bottom right corner of each plot.

Table 3.3: ER_{stiff} values corresponding to each Re_C and ϕ value combination

$\phi(\%)$ \ Re_C	**5**	**10**	**20**	**40**
5%	1.199 ± 0.046 $n = 10$	1.70529 ± 0.084 $n = 10$	2.404 ± 0.060 $n = 12$	2.396 ± 0.151 $n = 10$
10%	1.569 ± 0.054 $n = 12$	2.058 ± 0.028 $n = 7$	2.491 ± 0.118 $n = 12$	2.571 ± 0.120 $n = 6$
20%	1.643 ± 0.183 $n = 10$	2.479 ± 0.078 $n = 8$	2.570 ± 0.029 $n = 6$	2.609 ± 0.205 $n = 12$

value of flow rate and an average value of of ER_{stiff} for each of the Re_C was calculated. Average values of ER_{stiff} for each of the Re_C cases are reported in table 3.3 and variation of ER_{stiff} with Re_C is also plotted in figure 3.12. For each of the volume fraction cases, enrichment performance of the simple straight channel improves quite drastically upto certain value of Re_C and beyond that the improvement in ER_{stiff} reaches an asymptote. This observation is consistent with the results presented in section 2.4.3 and is useful for deciding on an optimum flow rate for obtaining the maximum enrichment performance. Increasing flow rate beyond this optimum value will not improve ER_{stiff} and may damage the microfluidic set up because of too high a fluid pressure.

Effect of Volume Fraction

Device performance was also characterized against variation of volume fraction (ϕ). The range of ϕ values for which experiments were run, better enrichment performance was obtained as the ϕ was increased as can be seen from table 3.3 and figure 3.12. In solutions with higher cell volume fraction, cell-cell interaction will be higher. This will in turn enhance the RBC-enhanced shear-induced diffusion (RESID) [64] of stiff RBCs towards the channel walls leading to better enrichment of cell types. This pattern of enhancement of ER with increasing ϕ is consistent with the simulation results presented in section 2.4.3. The maximum value of ϕ with which experiments were run was 20%. Experiments beyond

$\phi = 20\%$ resulted in frequent clogs in the outlet branching of the straight channel device.

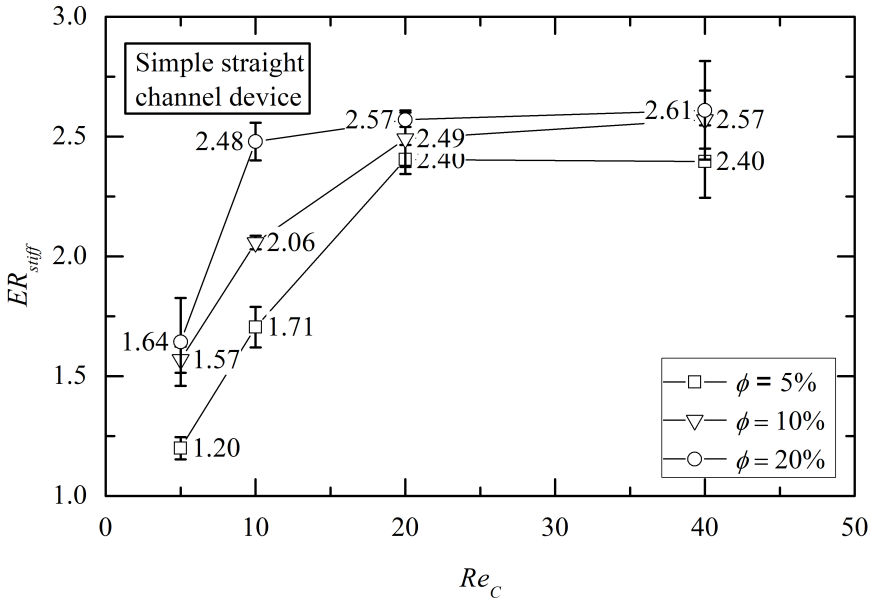

Figure 3.12: Variation of ER_{stiff} with Re_C for different volume fraction (ϕ) cases for simple straight channel device

Statistical Analysis

Statistical analysis was conducted on the data obtained from the experiments to determine the significance of variation of the parameters Re_C and ϕ on ER_{stiff}. As the intention was to conduct an ANOVA analysis, first the distribution of the ER_{stiff} was tested against standard normal distribution, as ANOVA analysis requires the data to be normally distributed. Figure 3.13 shows the quantile-quantile plot, also known as qq-plot used for determining whether or not a data distribution matches the normal distribution. From the distribution plotted on the qq-plot, it can be concluded that the ER_{stiff} values follow a normal distribution as the data points nearly follow the straight line that represents standard normal distribution. The aberration from straight line at the two end of the data points, indicates that distribution of ER_{stiff} is a normal distribution with fat tail at the two extremities.

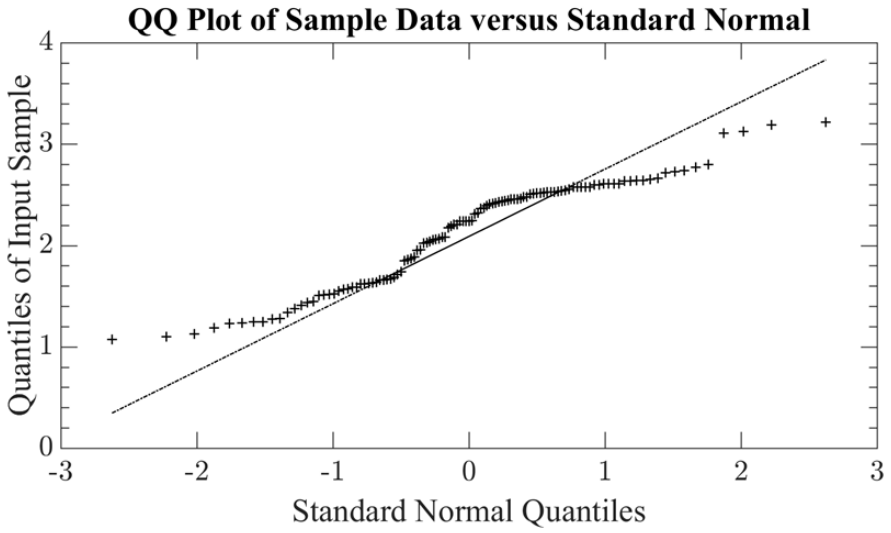

Figure 3.13: QQ plot for ER_{stiff} distribution. The straight line stands for standard normal distribution. ER_{stiff} data distribution is represented by '+' markers.

Table 3.4: Two-way ANOVA analysis for simple straight channel

Source	DoF	F	p
$\boldsymbol{\phi}$	2	35.41	$1.97e-12$
$\boldsymbol{Re_C}$	3	165.38	$3.09e-39$
$\boldsymbol{\phi \times Re_C}$	6	4.68	0.0003
Error	103		
Total	114		

For statistical analysis a Two Way ANOVA analysis was conducted, as there were two factors (Re_C and ϕ) for which ER_{stiff} was recorded. As can be observed from table 3.4, $p < 0.05$ for both the individual factors ϕ and Re_C. This indicates that both channel Reynolds number and volume fraction individually influences ER_{stiff} and hence the performance of the separation device. However, the most interesting observation is the fact that $p < 0.05$ for the interaction term ($\phi \times Re_C$) as well. This indicates that the parameters volume fraction and channel Reynolds number are not independent, and they jointly influences the performance of the enrichment device. This means, the extent to which varying Re_C influences the ER_{stiff} at a particular value of ϕ is different from when ϕ is set to a

different value and depending on the value of ϕ, ER_{stiff} may be affected negatively or positively with increasing or decreasing Re_C. Varying ϕ while keeping Re_C constant at a particular value will also show the same trend.

Presence of a significant interaction affects the tests for main effects. To study the independent effect of main parameters (ϕ and Re) conditional one-way ANOVA tests need to be conducted for ER_{stiff} for two situations: (i) test the effect of Re_C for a particular value of ϕ for all values of ϕ for which experiments were conducted and, (ii) test the effect of ϕ for a particular value of Re_C for all values of Re_C for which experiments were conducted.

Table 3.5: One-way ANOVA table for constant volume fraction(ϕ)

ϕ	Source	DoF	F	p
5	**Groups**	3	158.69	$1.55e-21$
	Error	38		
	Total	41		
10	**Groups**	3	93.45	$2.56e-15$
	Error	30		
	Total	33		
20	**Groups**	3	25.61	$5.99e-09$
	Error	35		
	Total	38		

Table 3.5 shows a part of the one-way ANOVA table generated by MATLAB for each of the ϕ values for which experiments were conducted. From the p-values given in the table for all the ϕ, it can be concluded that the enrichment efficiency of the simple straight channel is strongly influenced by Re_C at all values of volume fraction. The total DoF values in table 3.5 stand for the total number of experiments run for a particular value of the volume fraction.

Table 3.6 shows a part of the one-way ANOVA table generated by MATLAB for each of the Re_C values for which experiments were conducted. From the p-values given in the table, it appears for $Re_C = 5$ and $Re_C = 10$, enrichment efficiency is strongly influence by the

volume fraction of the cell solution. However, as the Re_C increases, effect of volume fraction on ER_{stiff} seems to be diminishing. For the two upper most values of Re_C at which experiments were conducted, volume fraction seems to have no effect on the enrichment efficiency.

Table 3.6: One-way ANOVA table for constant Reynolds number (Re_C)

Re_C	Source	DoF	F	p
5	**Groups**	2	25.13	$4.66e-07$
	Error	29		
	Total	31		
10	**Groups**	2	97.67	$1.00e-10$
	Error	19		
	Total	21		
20	**Groups**	2	2.36	0.1134
	Error	27		
	Total	29		
40	**Groups**	2	1.34	0.2774
	Error	28		
	Total	30		

3.3.2 Multistep Device

After validation of enrichment and characterization of performance for the simple straight channel, experiments were conducted to study and characterize the performance of newly designed multistep enrichment device. Enrichment experiments were conducted for Re_C and ϕ combinations presented in table 3.2. The single step device performance seemed to have improved the most for $\phi = 10\% - 20\%$ and $Re_C = 10 - 20$ range (refer to figure 3.12) and beyond these ranges in either direction, the enrichment performance and its improvement had been shown to be insignificant. So rather than trying a wide range of ϕ and Re_C for multistep enrichment device, it is more logical to run experiments for parameter ranges for which the single step device had been shown to perform best. As

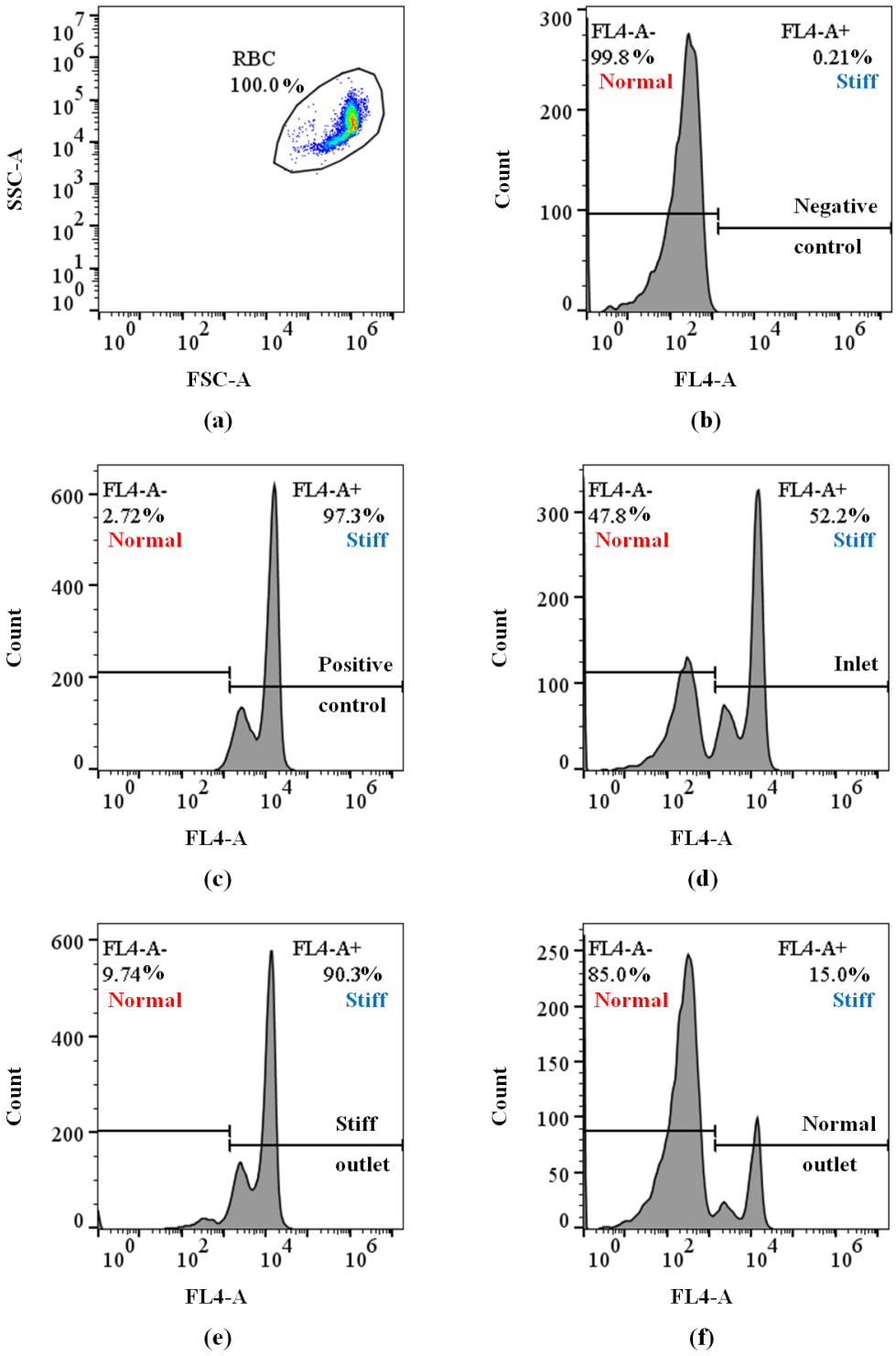

Figure 3.14: Flow cytometry analyses of cell samples collected after experiment with multi step enrichment device. (a) Scatter plot with the gate showing RBCs. (b)-(f) Histograms for allophycocyanin (APC) signal collected at channel FL4-A. Sample identifications are provided at the bottom right corner of each plot.

can be seen from figure 3.7 there are six outlets in the multi step device. According to the explanation provided in section 3.2.1, outlet 1 is expected to have the highest percentage of normal RBCs (and hence highest ER_{normal}) and outlet 4 and outlet 6 are expected to have the highest percentage of stiff RBCs (and hence highest ER_{stiff}). Although theoretically there is not supposed to be a difference in the ER_{stiff} obtained from outlet 4 and outlet 6, experimentally some difference was observed. Small variations in dimensions of different parts of channels stemming from micro-fabrication process, natural variance cell stiffness and other external fluctuations caused during experiments are some of the most likely reasons for the observed difference in ER_{stiff} values between outlet 4 and outlet 6. As the objective of the work is to show the multi step device's capability to get better enrichment compared to the simple straight channel, the higher of the two ER_{stiff} obtained from outlet 4 and 6 will be presented here.

Validation of Cell Enrichment

For each of the Re_C and ϕ combinations in table 3.2, six experiments were conducted to enrich stiff RBCs from a mixture of stiff and normal RBC. Results from flow cytometry analyses for one of the experiment run at $\phi = 20\%$ and $Re_C = 20$ are presented in figure 3.14. The enrichment ratios for stiff and normal RBCs calculated from the flow cytometry are $ER_{stiff} = 8.48$ and $ER_{normal} = 6.18$ respectively.

Table 3.7: ER_{stiff} for multistep device

$\phi(\%)$ \ Re_C	**10**	**20**
10%	3.388 ± 0.217 $n = 6$	4.616 ± 0.348 $n = 6$
20%	6.269 ± 0.460 $n = 6$	8.127 ± 0.828 $n = 6$

Table 3.7 shows the average ER_{stiff} values obtained for all the ϕ and Re_C combina-

tions for which experiments were conducted. Comparing the ER_{stiff} values of single step (3.3) and multi step device (3.7) for corresponding combinations of ϕ and Re_C, it appears that the newly designed multi step enrichment device boosts enrichment from ~ 1.6 to ~ 3.15 times, which is a remarkable improvement of performance.

Effect of ϕ and Re_C

Variation of ER_{stiff} with Re_C has been plotted for multiple ϕ cases in figure 3.15. As can be seen from figure 3.15, enrichment efficiency of multistep device improves as the flow rate (indicated by Re_C) and cell volume fraction are increased.

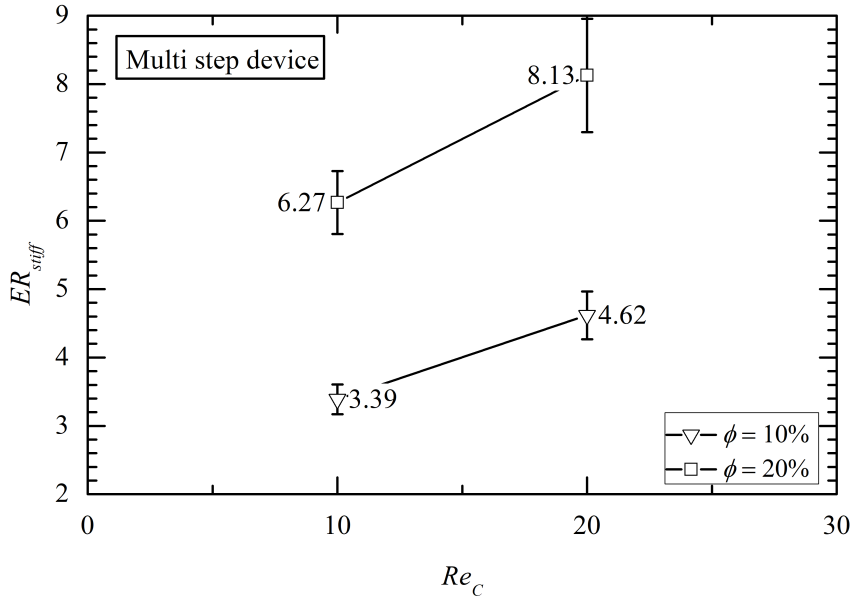

Figure 3.15: Variation of ER_{stiff} with Re_C for different volume fraction (ϕ) cases for multi step device

Statistical Analysis

As done for simple straight channel, ANOVA analysis was conducted on the enrichment ratio data for multi step device to study the significance of varying channel Reynolds number and hence flow rate and, volume fraction of cell solution. To check the distribution of

ER_{stiff} data qq-plot was generated for ER_{stiff} data against standard normal distribution (figure 3.16 (a)). From figure 3.16 (a) the distribution of ER_{stiff} looks like a normal distribution with a left fat tail. However when qq-plot was generated with natural logarithmic ratio of ER_{stiff} , i.e. $\log_e(ER_{stiff})$ as suggested in [147], the distribution looks like a normal distribution with fat tails on both ends as can be seen from figure 3.16 (b).

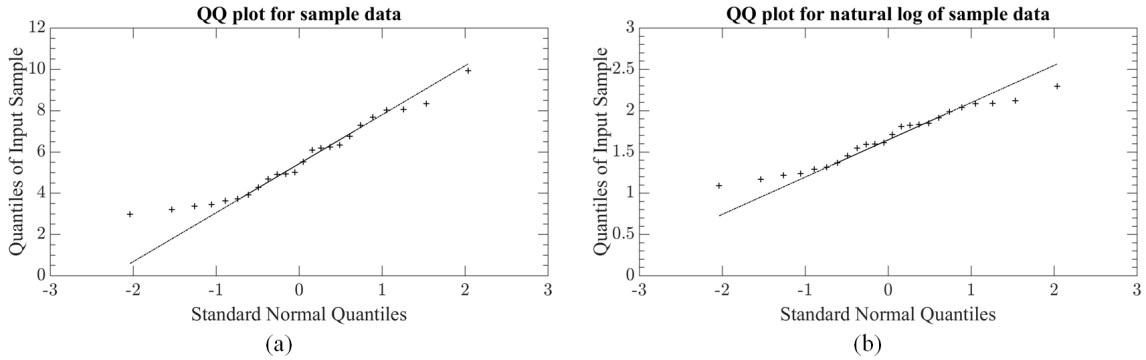

Figure 3.16: QQ plot for (a) ER_{stiff} and (b) $\log_e(ER_{stiff})$ distribution. The straight line stands for standard normal distribution. Input sample data distribution is represented by '+' markers.

Table 3.8: Two-way ANOVA analysis for multistep device

Source	DoF	F	p
$\boldsymbol{\phi}$	1	146.94	$1.13e-10$
$\boldsymbol{Re_C}$	1	34.24	$1.00e-05$
$\boldsymbol{\phi \times Re_C}$	1	1.43	0.2465
Error	20		
Total	23		

A portion of the two-way ANOVA statistics generated by MATLAB is presented in table 3.8. As can be observed from the table $p < 0.05$ for both the individual factors ϕ and Re_C. This indicates that both channel Reynolds number and volume fraction individually influences ER_{stiff} and hence the performance of the separation device.

3.4 Numerical Validation

To relate experimental results with results obtained from numerical simulations, multiple simulation cases were run with parameters matching the experiments for simple straight channel. The stiff RBC internal viscosity was set to double that of normal RBCs so that they match to the stiffness of glutaraldehyde stiffened RBCs. All the simulations were run for the channel size of $40\mu m \times 40\mu m \times 30\mu m$ with same boundary conditions stated in section 2.3 and shown in figure 2.5. As explained in section 2.3 this simulation configuration is sufficient to mimic the flow of cells in a straight micro-channel with high aspect ratio $\left(\frac{H}{W} > 2\right)$. The list of RBC properties used for these validation simulation cases can be found in table 3.9.

Table 3.9: Red blood cell properties

Cell type	Bending modulus $k_{bending}(J)$	Shear modulus $G\left(\frac{J}{m^2}\right)$	Area constraint coefficient $k_{area}\left(\frac{J}{m^2}\right)$	Volume constraint coefficient $k_{volume}\left(\frac{J}{m^2}\right)$	Viscosity ratio $\lambda = \frac{\nu_{in}}{\nu_{out}}$
Normal	4.7×10^{-18}	67×10^{-7}	1.7×10^{-5}	50.9	5
Stiff					10

For all the cases, simulations were run well beyond the length $L = 35mm$ point and then the cross sectional slice at $L = 35mm$ was extracted, as that was the length of the channels that were fabricated. From this slice, population distribution of cells were calculated by binning algorithom applied across the width of the channel. Subfigures of figure 3.17 show the steps mentioned above for a representative case of $\phi = 10\%$ and $Re_c = 10$. Figure 3.17(a) shows the close up view of the channel schematic near the $L = 35mm$. As can be seen from figure 3.17 (b), the simulation was run longer than $L = 35mm$ mark and a slice was cut at the same location corresponding to the length of channels in experiments. Figure 3.17 (c) shows snapshopts from simulations and figure 3.17 (d) shows the population

distribution (PD) across the channel width as a percentage of total population for each cell type. ER_{stiff} was calculated from figure 3.17 using equation 3.2.

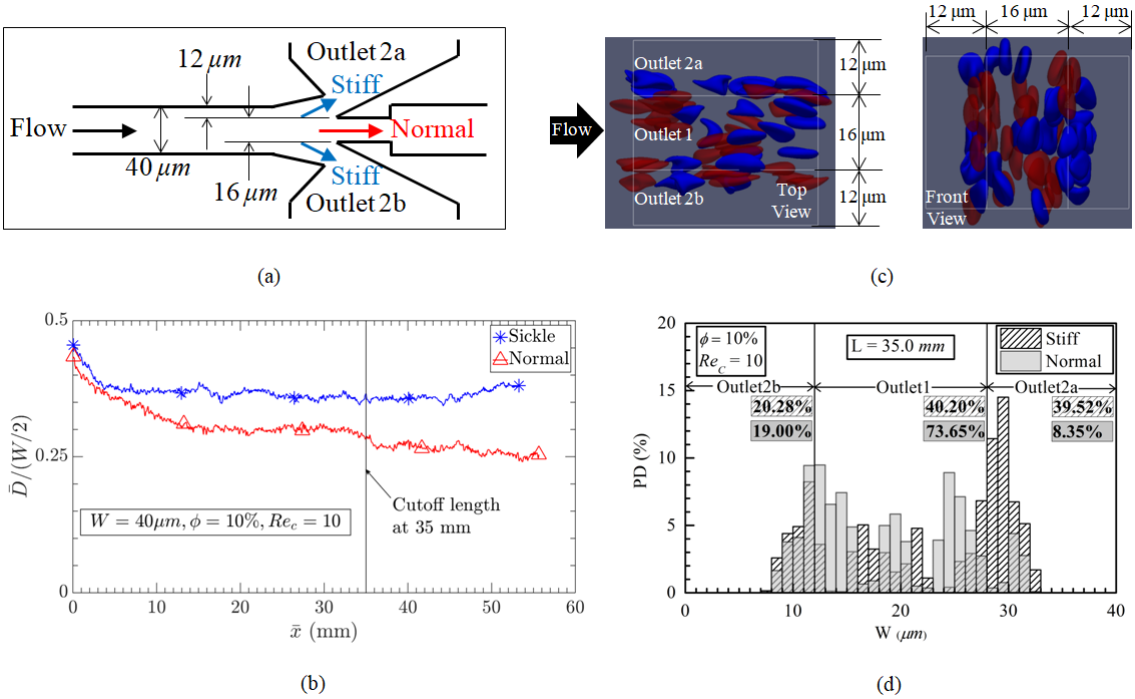

Figure 3.17: Cell population distribution, PD (%) across the width of channel at a particular lengthwise location for $\phi = 10\%$ and $Re_c = 10$ case. (a) Zoomed view of channel schematic near $L = 35mm$ location. (b) Non-dimensional cell margination plot showing the cutoff length location at $\overline{x} = 35mm$. (c) Snapshots of cell distribution around (top view) and at (front view) $L = 35mm$. (d) Cell PD calculated by binning the cells across the width of the channel.

Table 3.10 lists the ER_{stiff} values obtained from experiments and simulations for all the parameter (ϕ and Re_c) combinations that were compared. As observed from the table, the values of ER_{stiff} obtained from numerical simulations are quite close to the ones obtained through experiments. The slight difference can be attributed to the variation in stiffness property of real RBCs that occurs naturally, minor variation in channel dimension due to fabrication error and error due to disturbance from surroundings during flow experiments. Validation simulations were not run for all the combinations of ϕ and Re_c for which experiments were conducted, as the main objective of these simulations was to demonstrate the capability of numerical simulations to support the experimental results. It is expected that

results from simulations run for other combination of ϕ and Re_c will closely match with the results from experiments.

Table 3.10: List of validation cases

Domain size ($\mu m \times \mu m \times \mu m$)	ϕ (%)	Re_c	ER_{stiff} Experiment	ER_{stiff} Simulation
$40 \times 40 \times 30$	5	5	1.19 ± 0.04	1.25
	10	5	1.57 ± 0.05	1.84
	10	10	2.05 ± 0.02	2.18
	20	5	1.64 ± 0.18	1.96

A plot comparing the ER_{stiff} values obtained from simulations and experiments for $\phi = 10\%$ is provided in figure 3.18.

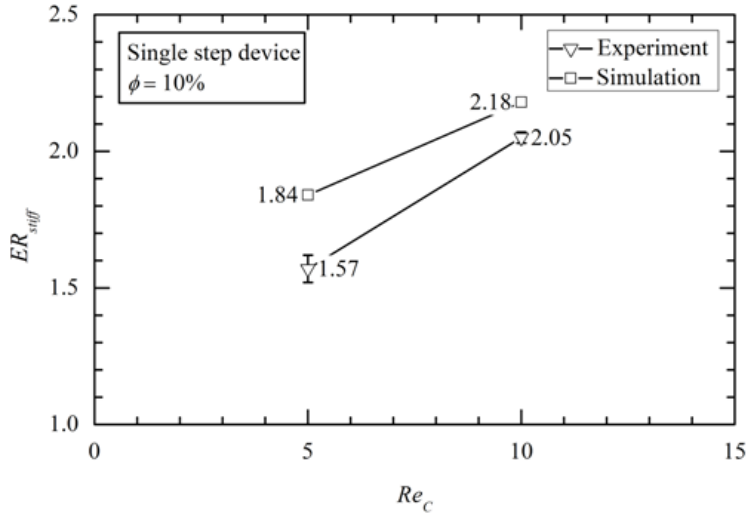

Figure 3.18: Variation of ER_{stiff} with Re_c compared between simulations and experiments for volume fraction of 10%

3.5 Conclusion

There were two major parts of this experimental work. In the first part a simple straight channel, similar to some previous works [46, 128, 129], was designed with improved design features. Cell enrichment experiments were conducted to enrich artificially stiffened RBC samples from a mixture of normal and stiff RBCs. Experiments were conducted for

a wide range of channel Reynolds number (and hence flow rate) and volume fraction of cells to characterize the enrichment performance of the straight channel device. Enrichment performance was found to be a strong function of both channel Reynolds number (and hence flow rate) and sample volume fraction. For a particular value of sample volume fraction the enrichment performance improved drastically up to a certain value of channel Reynolds number and beyond that value, the improvement of enrichment ratio plateaued. Similarly, for one particular value of channel Reynolds number, enrichment ratio improved as the cell volume fraction increased. The most interesting finding was the significant interaction between volume fraction and channel Reynolds number. The presence of interaction means that the extent to which varying flow rate influences the enrichment ratio at a particular value of volume fraction is different from when the volume fraction is set to a different value. The same pattern will be observed when cell volume fraction is varied keeping the flow rate constant. For obtaining best enrichment performance from the device both the channel Reynolds number and the volume fraction need to be optimized together. Increasing one of them while keeping the other constant will not provide the best enrichment performance. Numerical simulations were conducted with parameters matching with some of the experimental conditions and the results obtained from numerical simulations were very close the ones obtained from the experiments. This demonstrates the usefulness of numerical simulations as a supporting tool for experiments and provides a theoretical support for the observations from the experiments. In the second portion of the work, a new enrichment device was designed and fabricated. Enrichment experiments were conducted at different flow rates and volume fractions. For all the combinations of flow rate and cell volume fraction, enrichment ratio of the new device was found to be around 3 to 8 which was about 1.6 to 3.15 times higher compared to the simple straight channel devices. This is a very significant improvement of enrichment efficiency. The devices fabricated and tested here were not specific to any disease model and hence can be used for enrichment of disease affected cell sample for any disease that alters the cell deformability.

CHAPTER 4
CONCLUSION

4.1 Current Work

The main objective of this PhD research was to design and fabricate microfluidic devices that will separate stiff red blood cell sub-population from a mixture of normal and stiff red blood cells. Motivation of this work comes from the hematologic diseases like sickle cell disease, malaria spherocytosis and some cancers. Stiffness property of red blood cells change for the affected cells in these diseases. Isolating these affected red blood cells is essential for studying these diseases and has potential to lead to enhanced strategy of disease assessment and treatment. For diseases like Sickle Cell Disease, amount of stiffer RBCs in a patients' blood sample has been hypothesized to be correlated with the disease progression and therefore could potentially be used as a predictor for an oncoming bone pain episode.

The work was divided majorly in two parts. In the first portion of the work, stiffness dependent margination of red blood cells in microchannels with rectangular cross-section was studied with the help of direct numerical simulation. The numerical simulations were performed using a multiphase code that uses lattice Boltzmann method as fluid solver and spectrin link method for capturing the dynamics of red blood cells. Stiff RBCs were modeled by setting the internal viscosity couple of times higher than the normal ones. Multiple simulations were conducted to study different aspect of stiffness dependent cell margination. The findings from the simulations can be listed as following:

- Both for dilute (no cell-cell interaction) and dense (cell-cell interaction is significant) cell suspension, the stiffer cells marginate towards the channel walls whereas the normal ones stay closer around the channel centerline.

- Cells of different stiffness migrate to their average equilibrium locations faster for channels with smaller cross-section compared to that with larger cross-section.
- Increasing flow Reynolds number and hence shear rate up to certain limit boosts stiffness dependent cell margination.
- Increasing cell volume fraction boosts stiffness dependent cell margination as the cell-cell interaction is higher for higher volume fraction.

Results from the simulations provided useful guidance for designing microfluidic channels. The second part of the research was based on conducting experiments with the devices that were designed and fabricated with the insights obtained from the simulations. Experiments were run with two types of devices. The first type is a simple straight channel device, quite similar to the ones used in some previous studies [46, 128, 129], but with improved design features. Experiments conducted for a wide range of flow rate and volume fraction with simple straight channel revealed that the enrichment efficiency was a strong function of flow Reynolds number (and hence flow rate) and cell volume fraction up to a certain value of these parameters, and increasing them beyond those limits will not result in significant improvement of enrichment efficiency. However, the most interesting finding was that, flow Reynolds number and volume fraction are not two independent factors but actually jointly influence the enrichment performance of simple straight channel device. This means that the extent to which varying flow rate influences the enrichment ratio at a particular value of volume fraction is different from when the volume fraction is set to a different value. Best enrichment performance will depend on the optimal combination of channel Reynolds number (and hence flow rate) and cell volume fraction or hematocrit. Numerical simulations conducted with parameters matching with the experimental conditions revealed a remarkably close match between enrichment ratios calculated from experiments and those from the simulations. The second design can be considered as a multistep straight channel device. Experiments were conducted with different combinations of flow Reynolds number

and cell volume fraction and enrichment performance was observed to be 1.6 to 3.15 times better than simple straight channel device, which is a significant improvement from the previous works done in this field. To our knowledge, this is also the first time where such a rigorous experimental study of stiffness dependent cell margination and enrichment have been conducted with the support of an extensive simulation work.

4.2 Future Directions

Some of the suggested future work based on this research is listed below:

- Develop a better model for stiff red blood cells incorporating realistic values of membrane stiffness and bending stiffness corresponding to particular hematologic disorders. Run simulations to study and characterize stiffness dependent RBC margination in straight micro-channels.

- The devices designed for this work have experimentally shown the proof of concept of stiff dependent cell separation and are not specific to any particular hematologic disease. The next step would be to tailor the design of the devices for specific disease applications.

- The ultimate goal is to have a device that can directly take in patient blood sample and separate red blood cells subpopulations based on stiffness. One significant recent work in separating red blood cells from rest of the blood cell types was done by Zeming *et al.* [148]. Exploratory experiments should be conducted connecting a device similar to the one presented in [148] and the multistep device from this work in series and running whole blood samples through the setup with the final objective to enrich red blood cell sub-populations based on stiffness.

REFERENCES

[1] H.W. Hou et al. “Microfluidic devices for blood fractionation”. In: *Micromachines* 2 (2011), pp. 319–343.

[2] G. A. Barabino, M. O. Platt, and D. K. Kaul. “Sickle cell biomechanics”. In: *Annu. Rev. Biomed. Eng.* 12 (2010), pp. 345–367.

[3] URL: `http://www.redcrossblood.org/learn-about-blood/blood-facts-and-statistics`.

[4] S. Chakravorty and T. N. Williams. “Sickle cell disease: a neglected chronic disease of increasing global health importance”. In: *Archives of Disease in Childhood* 0 (2014), pp. 1–6.

[5] O. S. Platt et al. “Mortality in sickle cell disease – life expectancy and risk factors for early death”. In: *The New Englang Journal of Medicine* 330 (1994), pp. 1639–1644.

[6] L. A. Verduzco and G. Nathan. “Sickle cell disease and stroke”. In: *Blood* 114 (2009), pp. 5117–5125.

[7] T. L. Kauf et al. “The cost of health care for children and adults with sickle cell disease”. In: *American Journal of Hematology* 84 (2009), pp. 323–327.

[8] M.J. Stuart and R. L. Nagel. “Sickle-cell disease”. In: *The Lancet* 364.9442 (2004), pp. 1343–1360.

[9] M. H. Steinberg et al. In: *Disorders of Hemoglobin: Genetics, Pathophysiology and Clinical Management.* First. New York, NY, Chap. 6: Cambridge University Press, 2001. Chap. 26, pp. 711–755. ISBN: 0-521-63266-8.

[10] S. Chien. “Red cell deformability and its relevance to blood flow”. In: *Anu. Rev. Physiol.* 49 (1987), pp. 177–192.

[11] E. Evans, N. Mohandas, and A. Leung. “Static and dynamic rigidities of normal and sickle erythrocytes. Major influence of cell hemoglobin concentration”. In: *J. Clin. Invest.* 73 (1984), pp. 477–488.

[12] S. K. Ballas and N. Mohandas. “Sickle red cell microrheology and sickle blood rheology”. In: *Microcirculation* 11 (2004), pp. 209–225.

[13] D. C. Rees, T. N. Williams, and M. T. Gladwin. “Sickle-cell disease”. In: *The Lancet* 376.9757 (2010), pp. 2018–2031.

[14] N. Mohandas, J. A. Chasis, and S. B. Shohet. “The influence of membrane skeleton on red cell deformability, membrane material properties and shape”. In: *Seminars in Hematology* 20.3 (1983), pp. 225–242.

[15] M.R. Clark et al. “Influence of red cell water content on the morphology of sickling”. In: *Blood* 55.3 (1980), pp. 823–830.

[16] E. Evans and N. Mohandas. “Membrane associated sickle hemoglobin: a major determinant of sickle erythrocyte rigidity”. In: *Blood* 70.5 (1987), pp. 1443–1449.

[17] G.B. Nash, C.S. Johonson, and H.J. Meiselman. “Influence of oxygen tension on the viscoelastic behavior of red blood cells in sickle cell disease”. In: *Blood* 67.1 (1986), pp. 110–118.

[18] G.B. Nash, C.S. Johonson, and H.J Meiselman. “Rheologic impairment of sickle RBCs induced by repetitive cycles of deoxygenation-reoxygenation”. In: *Blood* 72.2 (1988), pp. 539–545.

[19] T. Itoh, S. Chien, and S. Usami. “Effects of hemoglobin concentration on deformability of individual sickle cells after deoxygenation”. In: *Blood* 85.8 (1995), pp. 2245–2253.

[20] C. Brugnara, H.F. Bunn, and D.C. Tosteson. “Regulation of erythrocyte cation and water content in sickle cell anemia”. In: *Science* 232.4748 (1986), pp. 388–390.

[21] C. Brugnara. URL: `http://sickle.bwh.harvard.edu/clt.html`.

[22] N. Mohandas, M.E. Rossi, and M.R. Clark. “Association between morphologic distortion of sickle cells and deoxygenation-induced cation permeability increase”. In: *Blood* 68.2 (1986), pp. 450–454.

[23] G.B. Nash, C.S. Johonson, and H.J Meiselman. “Mechanical properties of oxygenated red blood cells in sickle cell (HbSS) disease”. In: *Blood* 63.1 (1984), pp. 73–82.

[24] D. K. Kaul et al. “Erythrocytes in sickle cell anemia are heterogenous in their rheological and hemodynamic characteristics”. In: *J. Clin. Invest.* 72 (1983), pp. 22–31.

[25] R. P. Hebbel. “Adhesive interactions of sickle erythrocytes with endothelium”. In: *J. Clin. Invest.* 99.11 (1997), pp. 2561–2564.

[26] S. I Rubinow and J. B. Keller. “The transverse force on a spinning sphere moving in a viscous fluid”. In: *J. Fluid Mech.* 11.3 (1961), pp. 447–459.

[27] P. G. Saffman. “The lift on a small sphere in a slow shear flow”. In: *J. Fluid Mech.* 22.2 (1965), pp. 385–400.

[28] J.A. Schonberg and E. J. Hinch. “Intertial migration of a sphere in Poiseuille flow”. In: *J. Fluid Mech.* 203 (1989), pp. 517–524.

[29] H.L. Goldsmith and S. G. Mason. “The flow of suspensions through tubes. I. Single spheres, rods and discs”. In: *J. Colloid Sc.* 17.5 (1962), pp. 448–476.

[30] R. G. Cox and H. Brenner. “The lateral migration of solid particles in Poiseuille flow-I theory”. In: *Chemical Engineering Science* 23.2 (1968), pp. 147–173.

[31] E. S. Asmolov. “The inertial lift on a spherical particle in a plane Poiseuille flow at large channel Reynolds number”. In: *J. Fluid Mech.* 381 (1999), pp. 63 –87.

[32] S. Mortazavi and G. A. Tryggvason. “A numerical study of the motion of drops in Poiseuille flow. Part 1. Lateral migration of one drop”. In: *J. Fluid Mech.* 411 (2000), pp. 325 –350.

[33] J. Magnaudet, S. Takagi, and D. Legendre. “Drag, deformation and lateral migration of a buoyant drop moving near a wall”. In: *J. Fluid Mech.* 476 (2003), pp. 115 –157.

[34] H. Lan and D. B Khismatullin. “A numerical study of the lateral migration and deformation of drops and leukocytes in a rectangular microchannel”. In: *Int. J. Multiphase Flow.* 47 (2012), pp. 73 –84.

[35] P. C.-H. Chan and L. G Leal. “The motion of a deformable drop in a second-order fluid”. In: *J. Fluid Mech.* 92.1 (1979), pp. 131–170.

[36] A. Karnis and S. G. Mason. “Particle motions in sheared suspension. Part 23. Wall migration of fluid drops.” In: *J. Colloid and Interface Sci.* 24.2 (1967), pp. 164–169.

[37] W. Hiller and T. A. Kowaleski. “An experimental study of the lateral migration of a droplet in a creeping flow”. In: *Experiments in fluids* 5.1 (1986), pp. 43–48.

[38] H. Zhou and C. Pozrikidis. “Pressure-driven flow of suspensions of liquid drops”. In: *Microfluidics and Nanofluidics* 6.1 (1994), pp. 80–94.

[39] C. K. W. Tam and W. A Hyman. “Transverse motion of an elastic sphere in a shear field”. In: *J. Fluid Mech.* 59.1 (1973), pp. 177 –185.

[40] S. K. Doddi and P Bagchi. “Lateral migration of capsule in plane Poiseuille flow in a channel”. In: *Int. J. Multiphase Flow.* 34.10 (2008), pp. 966 –986.

[41] T. Krüger, B. Kaoui, and J. Harting. “Interplay of inertia and deformability on rheological properties of a suspension of capsules”. In: *J. Fluid Mech.* 751 (2014), pp. 725–745.

[42] M. Abkarian and A. Viallat. “Dynamics of vesciles in a wall-bounded shear flow”. In: *Biophysical Journal* 89.2 (2005), pp. 1055–1066.

[43] G. Segré and A. Silberberg. “Radial particle displacements in poiseuille flow of suspensions”. In: *Nature* 189 (1961), pp. 209–210.

[44] G. Segré and A. Silberberg. “Behavior of macroscopic rigid spheres in Poiseuille flow. Part 2. Experimental results and interpretation”. In: *J. Fluid Mech.* 14.1 (1962), pp. 136–157.

[45] J. P. Matas, J. F. Morris, and E. Guazzelli. “Lateral forces on a sphere”. In: *Oil & Gas Sci. Tech.* 59.1 (2004), pp. 59 –70.

[46] S.C. Hur et al. “Deformability-based cell classification and enrichment using inertial microfluidics”. In: *Lab on a Chip* 11.5 (2011), pp. 912–920.

[47] J. Feng, H. H. Hu, and D. D. Joseph. “Direct simulation of initial value problems for the motion of solid bodies in a Newtonian fluid. Part 2. Couette and Poiseuille flows”. In: *J. Fluid Mech.* 277 (1994), pp. 271 –301.

[48] J. B. McLaughlin. “The lift on a small sphere in wall-bounded linear shear flows.” In: *J. Fluid Mech.* 246 (1993), pp. 249 –165.

[49] A. J. Hogg. “The inertial migration of non-neutrally buoyant spherical particles in two-dimensional shear flows”. In: *J. Fluid Mech.* 272 (1994), pp. 285 –318.

[50] L. Y. Zeng, S. Balachandar, and P. Fischer. “Wall-induced forces on a rigid sphere at finite Reynolds number”. In: *J. Fluid Mech.* 536 (2005), pp. 1–25.

[51] G. Coupier et al. “Noninertial lateral migration of vesicles in bounded Poiseuille flow”. In: *Physics of Fluids* 20.11 (2008), p. 111702.

[52] G. Danker, P. M. Vlahovska, and C. Misbah. “Vesicles in Poiseuille flow”. In: *Phys. Rev. Lett.* 102.14 (2009), p. 148102.

[53] A. Kilimnik, W. Mao, and A. Alexeev. “Inertial migration of deformable capsules in channel flow”. In: *Physics of Fluids* 23.12 (2011), p. 123302.

[54] A. Nourbakhsh, S. Mortazavi, and Y. Afshar. “Three-dimensional numerical simulation of drops suspended in Poiseuille flow at non-zero Reynolds numbers”. In: *Physics of Fluids* 23.12 (2011), p. 123303.

[55] D. Di Carlo. “Inertial microfluidics”. In: *Lab on a Chip* 9.21 (2009), pp. 3038–3046.

[56] H.L. Goldsmith and J. Marlow. “Flow behavior of erythrocytes. I. Rotation and deformation in dilute suspensions”. In: *Proc. Royal. Soc. Lond. B* 182.1068 (1972), pp. 351–384.

[57] H.L. Goldsmith and J. Marlow. “Flow behavior of erythrocytes. II. Particle motions in concentrated suspensions of ghost cells.” In: *J. Colloid and Interface Sc.* 71.2 (1979), p. 383 407.

[58] M. M. Dupin et al. “Modeling the flow of dense suspensions of deformable particles in three dimensions”. In: *Physical Review E* 75.6 (2007), p. 066707.

[59] J. L. McWhirter, i H. Noguch, and G. Gompper. “Flow-induced clustering and alignment of vesicles and red blood cells in microcapillaries”. In: *PNAS* 106.15 (2009), pp. 6039 –6043.

[60] R. M. MacMeccan et al. “Simulating deformable particle suspensions using a coupled lattice-Boltzmann and finite-element method”. In: *J. Fluid Mech.* 618 (2009), pp. 13 –39.

[61] J. Wu and C. K. Aidun. “Simulating 3D deformable particle suspensions using lattice Boltzmann method with discrete external boundary force”. In: *Int. J. Numer. Meth. Fluids* 62.7 (2010), pp. 765 –783.

[62] D. A. Reasor Jr., Clausen J. R., and C. K. Aidun. “Coupling the lattice-Boltzmann and spectrin-link methods for the direct numerical simulation of cellular blood flow”. In: *Int. J. Numer. Meth. Fluids* 68.6 (2012), pp. 767 –781.

[63] D. A. Reasor Jr., J. R. Clausen, and C. K. Aidun. “Rheological characterization of cellular blood in shear”. In: *J. Fluid Mech.* 726 (2013), pp. 497–516.

[64] M. Mehrabadi, D. N. Ku, and C. K. Aidun. “Effects of shear rate, confinement, and particle parameters on margination in blood flow”. In: *Physical Review E* 93.2 (2016), p. 023109.

[65] D. A. Reasor Jr. “Numerical simulation of cellular blood flow”. PhD thesis. Georgia Institute of Technology, 2011.

[66] S. Chen and G. D. Doolen. “Lattice Boltzmann method for fluid flows.” In: *Annual Review of Fluid Mechanics* 30 (1998), pp. 329–64.

[67] C. K. Aidun and J. R. Clausen. “Lattice-Boltzmann method for complex flows”. In: *Annu. Rev. Fluid Mech.* 42 (2009), pp. 439–472.

[68] S. Succi. *The lattice-Boltzmann equation for fluid dynamics and beyond*. Oxford: Oxford University Press, 2001.

[69] J. Li et al. “Spectrin-level modeling of cytoskeleton and optical tweezers stretching of erythrocyte”. In: *Biophysical Journal* 88.5 (2005), pp. 3707–19.

[70] M. Dao, J. Li, and S. Suresh. “Molecularly based analysis of deformation of spectrin network and human erythrocyte”. In: *Materials Science and Engineering C* 26.8 (2006), pp. 1232–1244.

[71] I. V. Pivkin and G. E. Karniadakis. “Accurate coarse-grained modeling of red blood cellls”. In: *Phys. Rev. Lett.* 101.11 (2008), p. 118105.

[72] D. A. Fedosov, B. Caswell, and G. E. Karniadakis. “Coarse-grained red cell model with accurate mechanical properties, rheology and dynamics.” In: *31st Inter. Conf. IEEE EMBS* (2009), pp. 4266–4269.

[73] I. V. Karlin, A. Ferrante, and H. C. Ottinger. “Perfect entropy functions of the lattie Boltzmann method”. In: *European Physical Letters* 47 (1999), pp. 182–188.

[74] D. d’Humiéres. “Generalized lattice-Botzmann equations”. In: *Progress in Astronautics and Aeronautics* 159 (1994), pp. 450–458.

[75] A. J. C. Ladd. “Numerical simulations of particulate suspensions via a discretized Boltzmann equation. Part 1. Theoretical foundation”. In: *J. Fluid Mech.* 271 (1994), pp. 285–309.

[76] A. J. C. Ladd. “Numerical simulations of particulate suspensions via a discretized Boltzmann equation. Part 2. Numerical results”. In: *J. Fluid Mech.* 271 (1994), pp. 311–339.

[77] J. R. Clausen, D. A. Reasor Jr., and C. K. Aidun. “Parallel performance of a lattice-Boltzmann/ finite element cellular blood flow solver on IBM blue gene/p architecture”. In: *Computer Physics Communications* 181.6 (2010), pp. 1013–1020.

[78] E. Ding and C. K. Aidun. “The dynamics and scaling law for particles suspended in shear flow with inertia”. In: *J. Fluid Mech.* 423 (2000), pp. 317–344.

[79] A. J. C. Ladd and R. Verberg. “Lattice-Boltzmann simulations of particle-fluid suspensions”. In: *J. Stat. Phys.* 104.5-6 (2001), pp. 1191–1256.

[80] C.K. Aidun and Y Lu. “Lattice Boltzmann simulation of solid particles suspended in fluid”. In: *J. Stat. Phys* 81.1 (1995), pp. 49–61.

[81] C.K. Aidun, Y. Lu, and E.J. Ding. “Direct analysis of particulate suspensions with inertia using the discrete boltzmann equation”. In: *J. Fluid Mech.* 373 (1998), pp. 287–311.

[82] E. Ding and C. K. Aidun. “Extension of the lattice-Boltzmann method for direct simulation of suspended particles near contact”. In: *J. Stat. Phys.* 112.3-4 (2003), pp. 685–708.

[83] J. R. Clausen, D. A. Reasor Jr., and C. K. Aidun. “The rheology and microstructure of concentrated non-colloidal suspensions of deformable capsules”. In: *J. Fluid Mech.* 685 (2011), pp. 202–234.

[84] P. Bhatnagar, E. Gross, and M. Krook. “A model for collision processes in gases. I. Small amplitude processes in charged and neutral one-component systems”. In: *Physical Review* 94.3 (1954), pp. 511–525.

[85] Z. Hashemi and M. Rahnama. “Numerical simulation of tarnsient dynamic behavior of healthy and hardened red blood cells in microcapillary flow”. In: *Int. J. Numer. Meth. Biomed. Engng* 32.11 (2016), pp. 1 –12.

[86] D. A. Fedosov, B. Caswell, and G. E. Karniadakis. “A multiscale red blood cell model with accurate mechanics, rheology, and dynamics”. In: *Biophysical Journal* 98.10 (2010), pp. 2215–2225.

[87] D. A. Fedosov, B. Caswell, and G. E. Karniadakis. “Systematic coarse-graining of spectrin-level red blood cell models”. In: *Computer Methods in Applied Mechanics and Engineering* 199.29 (2010), pp. 1937–1948.

[88] J.F. Marko and E. D. Siggia. “Stretching DNA”. In: *Macromolecules* 28.26 (1995), pp. 8759–8770.

[89] C. Bustamante, Z. Bryant, and S. B. Smith. “Ten years of tension: single-molecule DNA mechanics”. In: *Nature* 421.6921 (2003), pp. 423–427.

[90] J. Lidmar, L. Mirny, and D. Nelson. “Virus shapes and buckling transitions in spherical shells”. In: *Physical Review E* 68.5 (2003), p. 051910.

[91] E. A. Evans, R. Waugh, and L. Melnik. “Elastic area compressibility modulus of red cell membrane”. In: *Biophysical Journal* 16 (1976), pp. 585–595.

[92] P. Hoogerbrugge and J. M. V. A. Koelman. “Simulating microscopic hydrodynamic phenomena with dissipative particle dynamics”. In: *Europhysics Letters* 19.3 (1992), pp. 155–166.

[93] R. M. Hochmuth and R. E. Waugh. “Erythrocyte membrane elasticity and viscosity”. In: *Annual Review of Physiology* 49.1 (1987), pp. 209–219.

[94] D. A. Fedosov. “Multiscale modeling of blood flow and soft matter”. PhD thesis. Brown University, 2010.

[95] I. Ginzburg and P. Adler. “Boundary flow condition analysis for the 3-dimensional lattice Boltzmann model”. In: *Journal de Physique II* 4.2 (1994), pp. 191–214.

[96] D. R. Noble et al. “A consistent hydrodynamic boundary condition for the lattice Boltzmann method”. In: *Phys. of Fluids* ().

[97] W. C. Hwang and R. E. Waugh. “Energy of dissociation of lipid bilayer from the membrane skeleton of red blood cells”. In: *Biophysical Journal* 72.6 (1997), pp. 2669–2678.

[98] Papautsky I. Zhou J. “Fundamentals of inertial focusing in microchannels”. In: *Lab on a Chip* 13.6 (2013), pp. 1121–1132.

[99] H. Byun et al. “Optical measurement of biomechanical properties of individual erythrocytes from a sickle cell patient”. In: *Acta Biomaterialia* 8.11 (2012), pp. 4130–4138.

[100] K. Tsukada et al. “Direct measurement of erythrocyte deformability in diabetes mellitus with a transparent microchannel capillary model and high-speed video camera system.” In: *Microvascular Res.* 61 (2001), pp. 231–239.

[101] L.L. Munn and M.M. Dupin. “Blood cell interactions and segregation in flow”. In: *Annals of Biomedical Engineering* 36.4 (2008), pp. 534–544.

[102] K. Marina et al. “Blood soluble drag-reducing polymers prevent lethality from hemorrhagic shock in acute animal experiments”. In: *Biorheology* 41.1 (2004), pp. 53–64.

[103] E. C. Eckstein, D. G. Bailey, and A. H. Shapiro. “Self-diffusion of particles in shear flow of a suspension”. In: *J. Fluid Mech.* 79.1 (1977), pp. 191–208.

[104] D. Leighton and A. Acrivos. “Viscous resuspension”. In: *Chemical Engineering Science* 41.6 (1986), pp. 1377–1384.

[105] D. Leighton and A. Acrivos. “The shear-induced migration of particles in concentrated suspensions”. In: *J. Fluid Mech.* 181 (1987), pp. 415–439.

[106] J. M. Sosa et al. “The relationship between red blood cell deformability metrics and perfusion of an artificial microvascular network”. In: *Clinical Hemorheology and Microcirculation* 57.3 (2014), pp. 275–289.

[107] N. Pamme and C. Wilhelm. “Continuous sorting of magnetic cells via on-chip free-flow magnetophoresis”. In: *Lab on a Chip* 6.8 (2006), pp. 974–980.

[108] N. Xia et al. “Combined microfluidic-micromagnetic separation of living cells in continuous flow”. In: *Biomedical Microdevices* 8.4 (2006), pp. 299–308.

[109] K. H. Han and A. B. Frazier. “Paramagnetic capture mode magnetophoretic microseparator for high efficiency blood cell separations”. In: *Lab on a Chip* 6.2 (2006), pp. 265–273.

[110] U. Kim et al. “Multitarget dielectrophoresis activated cell sorter”. In: *Analytical Chemistry* 80.22 (2008), pp. 8656–8661.

[111] M. S. Pommer et al. “Dielectrophoretic separation of platelets from diluted whole blood in microfluidic channels”. In: *Electrophoresis* 29.6 (2008), pp. 1213–1218.

[112] M. D. Vahey and J. Voldman. “An equilibrium method for continuous-flow cell sorting using dielectrophoresis”. In: *Analytical Chemistry* 80.9 (2008), pp. 3135–3143.

[113] I. Doh and Y. H. Cho. “A continuous cell separation chip using hydrodynamic dielectrophoresis (DEP) process”. In: *Sensors and Actuators A: Physical* 121.1 (2005), pp. 59–65.

[114] M. M. Wang et al. “Microfluidic sorting of mammalian cells by optical force switching”. In: *Nature Biotechnology* 23.1 (2005), pp. 83–87.

[115] T. D. Perroud et al. “Microfluidic-based cell sorting of Francisella tularensis infected macrophages using optical forces”. In: *Analytical Chemistry* 80.16 (2008), pp. 6365–6372.

[116] A. E. Ekpenyong et al. “Viscoelastic properties of differentiating blood cells are fate-and function-dependent”. In: *PLoS One* 7.9 (2012), e45237.

[117] A. Lenshof et al. “Acoustic whole blood plasmapheresis chip for prostate specific antigen microarray diagnostics”. In: *Analytical Chemistry* 81.15 (2009), pp. 6030–6037.

[118] F. Petersson et al. “Free flow acoustophoresis: microfluidic-based mode of particle and cell separation”. In: *Analytical Chemistry* 79.14 (2007), pp. 5117–5123.

[119] J. Shi et al. “Continuous particle separation in a microfluidic channel via standing surface acoustic waves (SSAW)”. In: *Lab on a Chip* 9.23 (2009), pp. 3354–3359.

[120] S. Choi et al. “Continuous blood cell separation by hydrophoretic filtration”. In: *Lab on a Chip* 7.11 (2007), pp. 1532–1538.

[121] D. Di Carlo et al. “Continuous inertial focusing, ordering, and separation of particles in microchannels”. In: *PNAS* 104.48 (2007), pp. 18892–18897.

[122] S.C. Hur, A.J. Mach, and D. Di Carlo. “High-throughput size-based rare cell enrichment using microscale vortices”. In: *Biomicrofluidics* 5.2 (2011), p. 022206.

[123] E. Sollier et al. “Size-selective collection of circulating tumor cells using vortex technology”. In: *Lab on a Chip* 14.61 (2014), pp. 63–77.

[124] A. Jain and L.L. Munn. “Biomimetic postcapillary expansions for enhancing rare blood cell separation on a microfluidic chip”. In: *Lab on a Chip* 11.17 (2011), pp. 2941–2947.

[125] M. Masaeli et al. “Continuous inertial focusing and separation of particles by shape”. In: *Physical Review X* 2.3 (2012), p. 031017.

[126] M. Godin et al. “Using buoyant mass to measure the growth of single cells”. In: *Nature Methods* 7.5 (2010), pp. 387–390.

[127] T.F. Didar and M. Tabrizian. “Adhesion based detection, sorting and enrichment of cells in microfluidic Lab-on-Chip devices”. In: *Lab on a Chipn* 10.22 (2010), pp. 3043–3053.

[128] H. W. Hou et al. “Deformability based cell margination - A simple microfluidic design for malaria-infected erythrocyte separation”. In: *Lab on a Chip* 10.19 (2010), pp. 2605–2613.

[129] S. Yang et al. “Deformability-selective particle entrainment and separation in a rectangular microchannel using medium viscoelasticityl”. In: *Soft Matter* 8.18 (2012), pp. 5011–5019.

[130] G. Wang et al. “Stiffness dependent separation of cells in a microfluidic device”. In: *PLoS ONE* 8.10 (2013), e75901.

[131] B. P. Ho and L. G Leal. “Migration of rigid spheres in a two-dimensional unidirectional shear flow of a second-order fluid”. In: *J. Fluid Mech.* 76.4 (1976), pp. 783–799.

[132] W. Mao and A. Alexeev. “Hydrodynamic sorting of microparticles by size in ridged microchannels”. In: *Physics of Fluids* 23.5 (2011), p. 051704.

[133] G. Wang et al. “Microfluidic cellular enrichment and separation through differences in viscoelastic deformation”. In: *Lab on a Chip* 15.2 (2014), pp. 532–540.

[134] D. Di Carlo et al. “Particle segregation and dynamics in confined flows”. In: *Physical Review Letters* 102.9 (2009), p. 094503.

[135] A. Karnis, S. G. Mason, and H. L. Goldsmith. “Axial migration of particles in Poiseuille flow”. In: *Nature* 200 (1963), pp. 159–160.

[136] L.G. Leal. “Particle motions in a viscous fluid”. In: *Annual Review of Fluid Mechanics* 12.1 (1980), pp. 435–476.

[137] R. Fåhræus and T. Lindqvist. “The viscosity of the blood in narrow capillary tubes”. In: *American Journal of Physiology–Legacy Content* 96.3 (1931), pp. 562–568.

[138] M. Abkarian and A. Viallat. “Vesicles and red blood cells in shear flow”. In: *Soft Matter* 4.4 (2008), pp. 653–657.

[139] P.M. Vlahovska, T. Podgorski, and C. Misbah. “Vesicles and red blood cells in flow: From individual dynamics to rheology”. In: *Comptes Rendus Physique* 10.8 (2009), pp. 775–789.

[140] P. Olla. “The lift on a tank-treading ellipsoidal cell in a shear flow”. In: *Journal de Physique II* 7.10 (1997), pp. 1533–1540.

[141] N. Callens et al. “Hydrodynamic lift of vesicles under shear flow in microgravity”. In: *EPL(Europhysics Letters)* 83.2 (2008), p. 24002.

[142] S. Yang et al. “Sheathless elasto-inertial particle focusing and continuous separation in a straight rectangular microchannel”. In: *Lab on a Chip* 11.2 (2011), pp. 266–273.

[143] J.A. Pathak, D. Ross, and K.B. Migler. “Elastic flow instability, curved streamlines, and mixing in microfluidic flows”. In: *Physics of Fluids* 16.11 (2004), pp. 4028–4034.

[144] M. A. Tehrani. “An experimental study of particle migration in pipe flow of viscoelastic fluids”. In: *Journal of Rheology* 40.6 (1996), pp. 1057–1077.

[145] A.M. Leshansky et al. “Tunable nonlinear viscoelastic ”focusing” in a microfluidic device”. In: *Physical Review Letters* 98.23 (2007), p. 234501.

[146] D. Qin, Y. Xia, and G.M. Whitesides. “Soft lithography for micro-and nanoscale patterning”. In: *Nature protocols* 5.3 (2010), pp. 491–502.

[147] V. Vidakovic. In: *Engineering biostatistics: An introduction to using MATLAB and WinBUGS*. San Francisco, CA, USA: John Wiley & Sons Inc., 2017. Chap. 11, pp. 503–582. ISBN: 978-1-119-16896-6.

[148] K. K. Zeming, S. Ranjan, and Y. Zhang. “Rotational separation of non-spherical bioparticles using I-shaped pillar arrays in a microfluidic device”. In: *Nature Communications* 4.1625 (2013), pp. 1 –8.